Multijet Production in Charged Current Deep Inelastic Scattering with ZEUS at HERA

by

Homer Frederick Wolfe

A dissertation submitted in partial fulfillment of the

requirements for the degree of

Doctor of Philosophy

(Physics)

at the

University of Wisconsin – Madison

2008

Draft Version September 11, 2008

Multijet Production in Charged Current Deep Inelastic Scattering with ZEUS at HERA

Differential jet cross sections have been measured in charged current deep inelastic $e^{\pm}p$ scattering at high boson virtualities Q^2 with the ZEUS detector at HERA using an integrated luminosity of 0.36 fb^{-1}. Jets were identified using the k_T cluster algorithm in the longitudinally invariant inclusive mode. Polarised and unpolarised-corrected cross sections are presented for inclusive-jet production as functions of Q^2, x_{Bj} and the jet transverse energy and pseudorapidity. The dijet invariant mass cross section is also presented. Observation of three-jet events in charged-current processes is reported for the first time. The predictions of leading-logarithm parton-shower Monte Carlo models and next-to-leading-order QCD calculations are compared to the measurements.

The design, operation, and commissioning of the HERA Collider and ZEUS Detector required the dedication of many individuals, without whom this research would not have been possible. The author would also like to personally thank Professor Claudia Glasman for providing her guidance, skill, effort and time to this work and the associated publication. Professor Juan Terron also donated invaluable assistance with the theoretical calculations and numerous helpful suggestions during the course of this work. A special thanks is also given to the author's advisors: Professor Don Reeder, Dr. Alexander Savin, and Professor Wesley Smith, for providing expert advice and broad perspective to my education.

Contents

List of Tables

List of Figures

Chapter 1

Introduction

In this thesis, measurements of charged current jet production in polarized electron-proton scattering and comparison to theoretical predictions are presented. The results presented are beneficial to the understanding of fundamental interactions and dynamics of the proton. The measurements presented were performed using the ZEUS detector at the HERA collider, which was part of the DESY accelerator complex in Hamburg, Germany. The predictions were derived from a theory called the Standard Model of Particle Physics (SM), which is briefly outlined in this chapter. The parts of the SM most relevant to this analysis and the methods used to compute the predictions are described in detail in chapter 2, and the experimental conditions are described in chapter 3. The methods used to process, simulate, and select data from the detector are described in chapters 4, 5 and 6, respectively. The techniques used to analyze the data are presented in chapter 7, and the subsequent results are presented in chapter 8. The importance of this work and potential extensions of this study are discussed in chapter 9.

1.1 Particles of The Standard Model

At present, the most complete and general description of the content and behavior of matter is the Standard Model. It is a highly successful theory, with a range of validity covering several orders of magnitude in energy, and predicted quantities which agree with observation to many significant figures. The SM describes the properties of matter as the dynamics and interactions of particles which are fundamental in the sense that they have no internal structure, and are indistinguishable among a given variety.

The particles of the SM can be organized into two major categories based on their intrinsic angular momentum: particles which possess integral spin are referred to as *bosons*, while particles which possess half-integral spin are referred to as *fermions*. The elementary bosons of the SM mediate interactions of three kinds, and come in four types: photons, γ, which mediate the electromagnetic interaction, gluons, g, which mediate the *strong* interaction, and W & Z bosons, which mediate the *weak* interaction. gravitational interactions are not described by the SM, but are widely accepted to be negligible in the conditions described in this work.

The fermions of the SM are classified into two groups *quarks*, which possess the *color charge* of the strong interaction, and *leptons*, which do not. Protons, neutrons, and other *hadrons* are described in the standard model as composite objects, comprised of quarks and gluons. Quarks and gluons are referred to collectively as *partons* when describing the content of hadrons. Quarks each possess spin $\pm 1/2$, a color of *red*, *green* or *blue*, and an electric charge of +2/3 or -1/3. Quarks with electric charge 2/3 and -1/3 are referred to as *up-type*, and *down-type*, respectively. Up-type quarks appear

in three *flavors*: *up* (u), *charm* (c) and *top* (t), as do down-types: *down* (d), *strange* (s) and *bottom* (b).

Leptons possess spin $\pm 1/2$, no color charge, and electric charge of -1 or 0. Leptons with zero mass are referred to as *neutrinos*, and charged leptons include the electron (e^-), muon (μ), and the tau (τ). Neutrinos interact solely via the weak interaction, which associates one neutrino with each charged lepton. The neutrinos thus receive names from their weak interaction partners and are called the electron- (ν_e), muon- (ν_μ), and the tau neutrino (ν_τ). This pairing partitions the leptons into three *generations* of *doublets*, where each generation differs only by the mass of the particles of each type. The weak interaction likewise partitions quarks into three generations of doublets by associating pairs of up- and down-type quarks, specifically $u - d$, $s - c$ and $t - b$. The up type and down type quarks if each generation also differ only in their masses.

For each fermion, the SM additionally describes one antifermion. Fermions and their antipartners differ only by having the equal but opposite electrical charge, and in the case of quarks, having anticolor. The antiparticle of the electron is the *positron* (e^+), and is identical to the electron in every way except for having charge +1. All other antiparticles are usually named identically as their partners, but with a prefix of anti, and are symbolically denoted with an overline. For example, the antiparticle of the up is the antiup ($\overline{u}$), which appears with color of either *antired*, *antigreen* or *antiblue*.

The weak interaction additionally partitions fermions into two categories based on their *helicity*, which is the sign of the projection of a particles spin along its direction

of motion. Particles with positive helicity are said to be *right-handed*, while particles with negative helicity are called *left-handed*. The strength of a particle's coupling to the weak bosons is indicated by the quantum number weak isospin (T_3). Left-handed charged leptons and left-handed up-type quarks have $T_z = 1/2$, while left-handed neutrinos and left-handed down-type quarks have $T_z = -1/2$. Because right-handed fermions do not participate in the weak interaction, their weak isospin is 0 for all types. Table 1.1 summarizes the most important quantum numbers for the left-handed fermions.

1.2 The Standard Model Lagrangian and its Symmetries

In the SM, the particles listed in section 1.1 are the quanta of *fields*, $\phi(x)$, which are functions that take complex vector values at each point in space-time. These functions are determined by the minimization of a scalar *action*, S. The action is the space-time integral over the *lagrangian density*, $\mathcal{L}$, which is a functional of the fields and their *covariant derivatives* $D_\mu\phi$. This is written as

$$S = \int d^4x \mathcal{L}(\phi, D_\mu\phi). \tag{1.1}$$

The covariant derivatives take the form $D_\mu \equiv \partial_\mu - igA_\mu$, were g is the coupling strength of the interactions, and A_μ are *gauge potential fields*, analogous to the electromagnetic vector potential in classical electrodynamics.

The SM lagrangian is a member of a class of lagrangians which is invariant under local phase rotations, $\Lambda(x)$ of its fields $\phi \rightarrow e^{ig\Lambda}\phi$, and corresponding transformations of the gauge fields $A_\mu \rightarrow A_\mu - 1/g\partial_\mu\Lambda$. The value of $\Lambda(x)$ is defined independently at each point in space time, and takes matrix values with dimension appropriate to

	Generation	Name	Symbol	Electric Charge	Weak Isospin	Weak Hypercharge	Mass
Leptons	I	Electron	e^-	-1	-1/2	-1	511 keV
		Positron	e^+	+1	0	+2	
		Electron Neutrino	ν_e	0	+1/2	-1	< 2 eV
		Electron Antineutrino	$\overline{\nu_e}$	0	0	0	
	II	Muon	μ^-	-1	-1/2	-1	106 MeV
		Antimuon	μ^+	+1	0	+2	
		Muon Neutrino	ν_μ	0	+1/2	-1	< 2 eV
		Muon Antineutrino	$\overline{\nu_\mu}$	0	0	0	
	III	Tau	τ^-	-1	-1/2	-1	1.78 GeV
		Antitau	τ^+	+1	0	+2	
		Tau Neutrino	ν_τ	0	+1/2	-1	< 2 eV
		Tau Antineutrino	$\overline{\nu_\tau}$	0	0	0	
Quarks	I	Up Quark	u	+2/3	+1/2	+1/3	~ 3 MeV
		Up Antiquark	$\overline{u}$	-2/3	0	-4/3	
		Down Quark	d	-1/3	-1/2	+1/3	~ 6 MeV
		Down Antiquark	$\overline{d}$	+1/3	0	+2/3	
	II	Charm Quark	c	+2/3	+1/2	+1/3	~ 1.3 GeV
		Charm Antiquark	$\overline{c}$	-2/3	0	-4/3	
		Strange Quark	s	-1/3	-1/2	+1/3	~ 100 MeV
		Strange Antiquark	$\overline{s}$	+1/3	0	+2/3	
	III	Bottom Quark	b	-1/3	-1/2	+1/3	~ 4.2 GeV
		Bottom Antiquark	$\overline{b}$	+1/3	0	+2/3	
		Top Quark	t	+2/3	+1/2	+1/3	~ 171 GeV
		Top Antiquark	$\overline{t}$	-2/3	0	-4/3	

Table 1.1: Properties of Left-Handed Fermions.

the interaction in question. Such transformations are called *gauge transformations*, Lagrangians that are invariant under these transformations are called *gauge invariant*, and theories with gauge invariant lagrangians are called *gauge theories*. Gauge transformations form mathematical groups under composition, and provide the application of group theoretic technology to SM computations. The principle point of interest here is that because gauge transformations must be compatible with the potential fields, and the potential fields determine the interaction, the gauge symmetry group of the Lagrangian determines the interaction and vice versa.

The symmetry group for electromagnetic interactions is $U(1)$, which can be represented as the multiplicative group of complex numbers of magnitude 1. The resultant field theory is referred to as Quantum Electrodynamics (QED). The symmetry group of the weak interaction is $SU(2)$, which can be represented as a two-dimensional matrix group generated by traceless Hermitian matrices, such as the three Pauli matrices. In the SM, the electromagnetic and weak interactions are unified at high energies to form the gauge group $U(1)_Y \times SU(2)_L$, where $Y = 2(Q + I_z)$ denotes *hypercharge*, and I_z denotes *isospin*. This gauge is referred to as the *electroweak gauge* and its four generators correspond to four independent gauge fields, which at low energies form fields for the neutral (γ, Z^0) and charged (W^+, W^-) electromagnetic and weak bosons.

The symmetry group for the strong interaction is $SU(3)$, which can be represented as the three dimensional matrix group generated by traceless Hermitian matrices, such as the eight Gell-Mann matrices. From eight generators arise eight independent gluon color fields. The resultant field theory is referred to as Quantum Chromodynamics (QCD). While the U(1) group is ableian, the SU(2) and SU(3)

groups are not. As a consequence, photons do not interact with other photons, allowing for the principle of superposition. Weak and strong fields, on the otherhand, are self-interacting.

1.3 Perturbative Field Theory and Renormalization

For a given observable quantity in the SM, it is often infeasable to perform an exact computation. Instead, series expansion is often perfromed which can be truncated to finite order. Often, this expansion parameter is the coupling strength of a process.

$$f(\alpha) = \sum_{n=0}^{\infty} f_n \alpha^n$$

In this case, each f_n can be represented as a Feynman diagram, where the order n corresponds to the number of interaction vertices in the diagram. *Leading-order* (LO) diagrams denote those terms if lowest order in n, while *next-to-leading-order* (NLO) denote the next highest, and so forth. Although any observable must have a finite amplitude, individual Feynman diagrams may be divergent, and must be treated with a process called renormalization in order to produce a finite prediction.

The solution when encountering these divergences is to reinterpret the measurements not in terms of the parameters of the lagrangian, called the *bare parameters*, but instead different parameters, called *renormalized parameters*. These renormalized parameters are dependent upon how the measurement is made, and this is parameterized in terms of a *renormalization scale* (μ_{R}).

The result is that the coupling strength of a renormalized theory is not constant, but varies with scale $\alpha \to \alpha(\mu_{\mathrm{R}})$. This dependence is called *running* of the coupling,

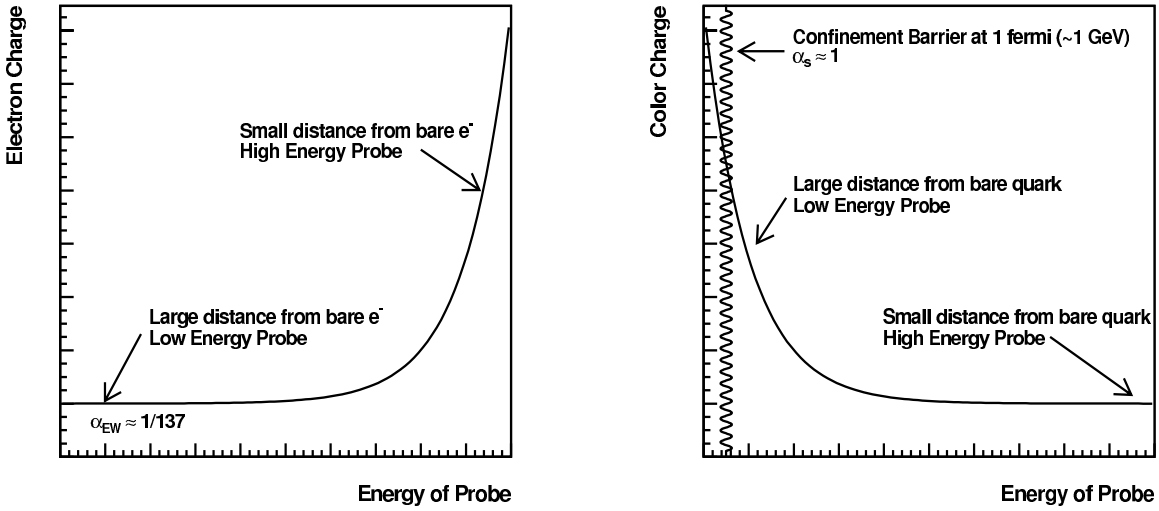

Figure 1.1: Behavior of the QED and QCD Couplings

and is a well observed phenomenon. The physical interpretation of the scale is dependent on the process, but can be thought of as proportional to the energy of a probe, or inversely proportional to the distance that a probe can resolve or penetrate.

Perturbative QCD has been used in this thesis to produce theoretical predictions, as described in sections 2.4.1 to 2.4.8. Leading order calculations are also at the core of the event simulations which are described in chapter 5.

1.4 Confinement and Asymptotic Freedom in QCD

Figure 1.1 depicts the trend of running for the QED and QCD coupling constants. Of greatest contrast is that the QED coupling asymptotically approaches a finite constant of approximately 1/137 for soft interactions, while the QCD coupling increases, and actually diverges at a factor called λ_{QCD}, whose value depends on the renormalization procedure. This increase of strength for soft particles is responsible for the feature of *confinement* which describes why colored partons are not observed

in nature, but instead are confined to groups of colorless hadrons. At large scales, the QCD coupling asymptotically approaches zero, which is called asymptotic freedom. At high center-of-mass energies, scattering of point-like electrons on composite protons can be described in terms of the scattering of electrons off of independent quarks and gluons, specifically due to asymptotic freedom.

Chapter 2

Theoretical Introduction

2.1 An Overview of ep Scattering

At leading order in the QPM, electrons and protons interact via the exchange of γ, Z^0, or W bosons. This is schematically described in figure 2.1. The exchanged boson is a probe of the proton, and it is useful to subdivide ep processes by the nature of this probe. If the exchanged boson is a nearly on-shell photon, the process is referred to as Photoproduction (PHP). PHP is a major source of background in this analysis, and great care was taken to characterize and remove it from the data sample. If the exchanged boson is a virtual photon, Z^0, or W, the process is referred to as Deep Inelastic Scattering (DIS). DIS is further subdivided into Neutral Current DIS (NC DIS) and Charged Current DIS (CC DIS). PHP and NC DIS are related to the presence of an isolated electron in the final state: $ep \to e + X$, while CC DIS is related to the process $ep \to \nu + X$, where X denotes any outgoing state.

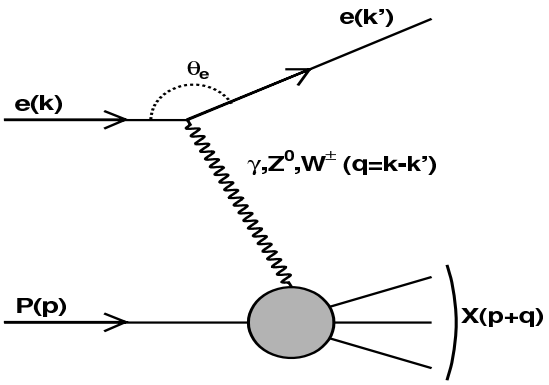

Figure 2.1: caption

2.1.1 Kinematics

To simplify discussion the initial state electron or positron will simply be referred to as the incoming lepton, and the final state electron, positron or neutrino will simply be referred to as the outgoing lepton. We label the 4-vectors of the incoming lepton, outgoing lepton, incoming proton and outgoing hadronic system as k, k', p, and p_X, respectively. Electrons will be considered massless, and the mass of the proton is labled M_p. The following are lorentz invariant quantities:

$$q^2 = (k - k')^2 = -Q^2, Q^2 > 0 \tag{2.1}$$

$$s = (p + k)^2 \tag{2.2}$$

$$W^2 = p_X^2 \tag{2.3}$$

$$\nu = \frac{p \cdot q}{M_p} = \frac{1}{2M_p}\left(W^2 + Q^2 - M_p^2\right) \tag{2.4}$$

Q, s, and W are identified as the transfer momentum, center of mass energy (CME) of the ep system, and invariant mass of the outgoing hadronic system. In the rest frame of the proton, ν is the energy difference of the incoming and outgoing lepton. The following variables will be used extensively:

$$x = \frac{Q^2}{2p \cdot q} = \frac{Q^2}{2M_p \nu} = \frac{Q^2}{W^2 + Q^2 - M_p^2} \tag{2.5}$$

$$y = \frac{p \cdot q}{p \cdot k} \tag{2.6}$$

The Bjorken scaling variable x is identified in the quark-parton model with the fraction of the momentum of the quark which participates in the hard scattering with that of the initial state proton. The variable y is referred to as the inelasticity of the interaction. Neglecting the masses of the incoming particles they are related by $Q^2 = sxz$.

2.1.2 Charged Current DIS

At leading order in CC DIS, the electron initiating the ep interaction is converted into a neutrino by the exchange of a virtual W boson, as shown in the LO Feynman diagram in figure 2.2. The neutrino in the outgoing state is not recorded by the ZEUS detector, resulting in a large amount of net measured transverse momentum ($P_{T,\text{miss}}$). This signature is the primary means of selecting CC DIS events.

2.1.3 Neutral Current DIS

At leading order in NC DIS, the electron initiating the ep interaction emerges in the final state, as shown in the LO Feynman diagram in figure 2.2. NC DIS is mediated by the exchange of virtual γ^* or Z^0 bosons. A majority of the products of

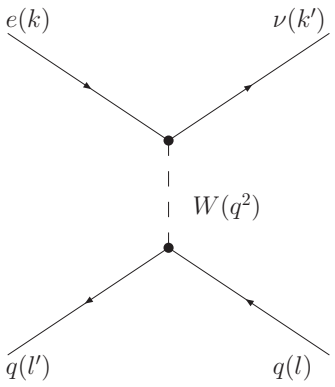

Figure 2.2: Leading-order Feynman diagram for $eq \rightarrow \nu q$, which is a principle contribution to CC DIS

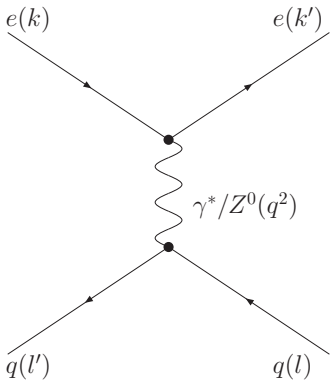

Figure 2.3: Leading-order Feynman diagram for $eq \rightarrow eq$, which is a principle contribution to NC DIS

the interaction are registered by the ZEUS detector, resulting in a small $P_{T,\text{miss}}$. The presence of an isolated electron in the final state is the primary means of rejecting NC DIS events. Further rejection is aided by selecting events with large $P_{T,\text{miss}}$.

2.1.4 Photoproduction

If a quasi-real photon is emitted by the incoming electron, then $q^2 \sim 0$, and $k \sim k'$. The outgoing electron will therefore exit the detector near the beampipe, and

may not be reconstructed. The outgoing electron will contain transverse momentum, resulting in non-zero $P_{T,\text{miss}}$. These two factors make some PHP events difficult to distinguish from CC DIS. The interaction between the photon and the proton often creates a large amount of E_T relative to $P_{T,\text{miss}}$, so a principle means of rejecting PHP is to select events where $P_{T,\text{miss}}/E_T$ is near one. During ep collisions in a general detector, some particles escape the detector close to the beampipe, causing the final measured values of energy and momentum to differ greatly from the initial values. On the otherhand, the quantity $E - p_z$ is less sensitive to these lost particles and is approximately conserved. It can be shown that at if the electron is registered in the detector in NC DIS, or if a neutrino in CC DIS has large p_t, that the measured value of $E - p_z$ will be close to twice the initial energy of the electron. If the electron is lost down the beampipe as in PHP, this value will be much smaller. This condition was used to further reject PHP.

2.1.5 Cross Sections

The results of this thesis are differential cross sections, $\frac{d\sigma}{d\Omega}$ which are defined as the rate or number of outgoing particles in a given state divided by the rate or number of incoming particles. Summing over all outgoing states results in the total cross section:

$$\sigma = \frac{d\sigma}{d\Omega} = \frac{N}{L} \tag{2.7}$$

Where N is the number of outgoing states of a given variety, and L is the *luminosity*, a measure of the incoming flux. This is related to the scattering amplitude by

$$d\sigma = \frac{1}{\text{incoming flux}} \frac{d^3k'}{dk'_0} \frac{1}{4} |\mathcal{M}|^2 \tag{2.8}$$

Where the amplitude for leading order NC scattering is given by

$$\mathcal{M}_{\mathrm{NC}} = e^2 \bar{u}(k', \lambda') \gamma^\mu u(k, \lambda) \frac{1}{q^2} \left\langle X \left| J_\mu^{\mathrm{EM}} \right| p, \sigma \right\rangle \tag{2.9}$$

and for CC is given by

$$\mathcal{M}_{\mathrm{CC}} = \frac{\sqrt{2} G_F}{1 + Q^2/M_W^2} \bar{u}(k', \lambda') \gamma^\mu \left(1 - \gamma_5\right) u(k, \lambda) \frac{1}{q^2} \left\langle X \left| J_\mu^{\mathrm{weak}} \right| p, \sigma \right\rangle \tag{2.10}$$

The generality of the outgoing hadronic state introduces ambiguity, which we account for by summing over all these states. we proceed by computing the spin-averaged cross sections via the introduction of a leptonic and hadronic tensor [24]

$$d\sigma \sim L_{\mu\nu} W^{\mu\nu} \tag{2.11}$$

$$W^{\mu\nu} \equiv \sum_N \int_{X_N} \left\langle p, \sigma \left| J^{\mu\dagger} \right| X_N \right\rangle \left\langle X_N \left| J^\nu \right| p, \sigma \right\rangle \tag{2.12}$$

Because the proton is a composite object governed by QCD outside the perturbative regime, we must write the hadronic tensor in a general form, and parameterize it through experimentally determined functions. We begin by writing all possible Lorentz invariant terms composed of the metric tensor, p, and q with preceding unitless scalar functions W_i. The choices of coefficients comes from hindsight to more easily arrive at general notation.

$$W^{\mu\nu} = -W_1 g^{\mu\nu} + \frac{W_2}{M_p} p^\mu p^\nu + W_3 i \epsilon^{\mu\nu\alpha\beta} p_\alpha q_\beta + \frac{W_4}{M_p} q^\mu q^\nu + \frac{W_5}{M_p} \left(p^\mu q^\nu + q^\mu p^\nu\right) \tag{2.13}$$

Current conservation requires $q_\mu W^{\mu\nu} = q_\nu W^{\mu\nu} = 0$, which can be used to show

$$W_4 = \frac{M_p}{q^2} W_1 + \left(\frac{p \cdot q}{q^2}\right)^2 W_2 \text{ and } W_5 = -\frac{p \cdot q}{q^2} W_2 \tag{2.14}$$

Combining these yields

$$W^{\mu\nu} = W_1 \left(\frac{q^\mu q^\nu}{q^2} - g^{\mu\nu} \right) + \frac{W_2}{M_p^2} \left(p^\mu - \frac{p \cdot q}{q^2} q^\mu \right) \left(p^\nu - \frac{p \cdot q}{q^2} q^\nu \right) + W_3 i\epsilon^{\mu\nu\alpha\beta} p_\alpha q_\beta \quad (2.15)$$

The leptonic tensor can be computed exactly, and is

$$L_{\mu\nu}(e^- p \to \nu X) \equiv \frac{1}{4} \left[\bar{\nu_e}(k') \gamma_\mu \left(1 - \gamma_5\right) e(k) \right] \left[\bar{\nu_e}(k') \gamma_\nu \left(1 - \gamma_5\right) e(k) \right] \quad (2.16)$$

for electron scattering and

$$L_{\mu\nu}(e^+ p \to \bar{\nu} X) \equiv \frac{1}{4} \left[\bar{e}(k) \gamma_\mu \left(1 - \gamma_5\right) \nu(k') \right] \left[\bar{e}(k) \gamma_\nu \left(1 - \gamma_5\right) \nu(k') \right] \quad (2.17)$$

for protons. Because we neglect the mass of the incoming electron, we can write both of these expressions as

$$L_{\mu\nu} = 2 \left[k_\mu k'_\nu + k'_\mu k_\nu - g_{\mu\nu} k \cdot k' \pm i\epsilon_{\mu\nu\alpha\beta} k'^\alpha k^\beta \right], \quad (2.18)$$

where the term takes + for electrons and − for positrons.

2.2 Structure Functions and Parton Distribution Functions

The functions W_1, W_2 and W_3 can be replaced with *structure functions*

$$\begin{aligned} F_1^C C(x, Q^2) &= M_P W_1 \\ F_1^C C(x, Q^2) &= \nu W_2 \\ F_1^C C(x, Q^2) &= \nu W_3, \end{aligned} \quad (2.19)$$

which allows us to write the differential cross section for CC DIS as

$$\frac{d^2\sigma(e^\pm p \to \nu X)}{dx dQ^2} = \frac{G_F^2}{4\pi x} \left(\frac{M_W^2}{M_W^2 + Q^2} \right) [?] \quad (2.20)$$

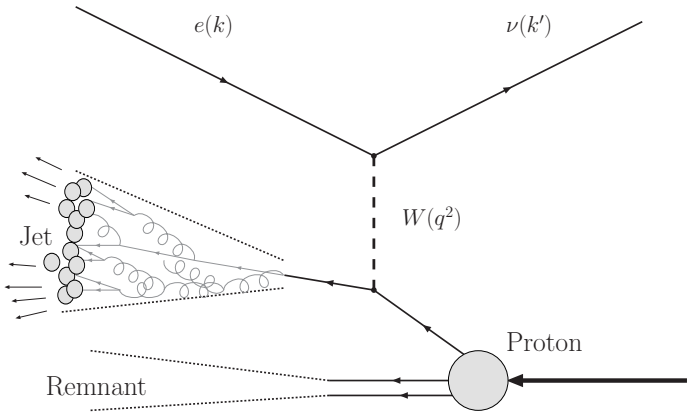

Figure 2.4: Schematic Diagram of Leading-order Jet Production in CC DIS.

2.3 Jet Production in DIS

While isolated quarks and gluons cannot be directly observed, objects which are very correlated to these states can be **??**. Because the QCD coupling constant is large for small momentum transfers, QCD radiation is largely dominated by low-p_t emission of gluons and $q\bar{q}$ pairs. This implies that the QCD radiation will not commonly diverge greatly from the quark or gluon that initiated the process, creating nearly parallel clusters of colorless particles in detectors. This is represented schematically in figure 2.4. Sprays of particles in this formation are referred to as jets. Depending on the subprocess, and the possibility of subsequent hard QCD radiation, events can also exhibit multiple separated jets.

2.3.1 The MEPJET Program

The pQCD calculations in this thesis were produced with the MEPJET 2.1 [25, 26] program, which was written for DIS by E. Mirkes. D. Zeppenfeld and S. Willfahrt. It is capable of computing partonic cross sections in DIS via exchange of photons, Z,

and W bosons at $\mathcal{O}(\alpha_{\rm S})$ or $\mathcal{O}({\alpha_{\rm S}}^2)$. For this analysis, only W exchange was calculated, with the mass of the W boson set to 80.40 GeV. The number of active quark flavors was set to 5, and $\Lambda^{(5)}_{\overline{\rm MS}}$ was set to 226 MeV, which corresponded to a strong coupling constant $\alpha_{\rm S}(M_Z) = 0.118$. $\alpha_{\rm EM}$, G_F, and M_Z were set to the same values as chosen for the MC described in section 5.4. For the inclusive-jet calculations, $\mathcal{O}(\alpha_{\rm S})$ predictions were produced, which are NLO. For dijet (three-jet) cross sections, $\mathcal{O}({\alpha_{\rm S}}^2)$ predictions were produced, which were NLO (LO).

2.3.2 Phase Space Slicing Method

The MEPJETprogram uses the phase space slicing method [27] to cancel infrared and collinear divergences. A parameter $s_{\rm min}$ was introduced, which acts as a minimum resolving power to separate partons, and effectively separates finite and infinite portions of the phase space. Integrals in regions where particles i and j satisfied $s_{ij} \cong 2p_i \cdot p_j < s_{min}$ were calculated analytically. Some divergences were matched and exactly cancelled with virtual contribution divergences, and others were subtracted as described in section 2.4.3. It has been shown that the final results are independent of the unphysical parameter $s_{\rm min}$ when $s_{\rm min}$ is less than or on the order of 0.1 GeV [26]. The remaining phase space, where the integrals were free of these divergences, were left to be calculated numerically by MC integration techniques. Leaving the finite portion of the phase space integral for the user provides a flexible system for custom modification of phase space cuts.

2.3.3 $\overline{\text{MS}}$ Renormalization Scheme

In MEPJET, the one-loop divergences in the diagrams are handled in the $\overline{\text{MS}}$ renormalization scheme. The scheme begins by introducing a dimensional regulator for loop momentum, by transforming the 4-dimensional integral over virtual particle momenta into $4 - 2\epsilon$ dimensions. This parameterizes the divergences in ϵ, but artificially introduces additional constant terms. The name stands for modified minimal subtraction, because the earlier method of subtracting only divergent parts [28] was later modified by additionally subtracting the constant terms that were introduced [29].

2.3.4 Factorization and Parton Density Functions

In addition to the choice of the renormalization scale at which the matrix elements are evaluated, an additional scale choice is made called the *factorization scale*. This scale is the delineation between the hard scattering, and the soft QCD processes in the proton. The PDFs used must be evolved from some originating scale to the factorization scale at which they are used. This evolution is accomplished via the DGLAP equations [MISSING: Explain DGLAP]

2.3.5 Scale Dependence and Uncertainty

In MEPJET, ultraviolet divergences were renormalized and absorbed into the bare coupling constant, introducing a dependence of the renormalized coupling $\alpha_{\text{S}}(\mu_{\text{R}})$. For this analysis, μ_{R} was set to Q for the central values extracted from the calculations. The dependence on μ_{R} would cancel for calculations performed at all orders in α_{S}, but for our fixed order calculations, some residual scale dependence persists. To quantify

the uncertainty introduced by our choice, the calculations were also performed for $\mu_R \equiv Q/2$ and $\mu_R \equiv 2Q$. The optimal amount of adjustment used in this technique is not universally agreed upon, but a factor of 2 is common practice for ZEUS publications.

In MEPJET, initial state collinear divergences were factorized into the bare parton densities, introducing a dependence of the final cross sections on the factorization scale μ_F. This scale was also set to Q, and modified by a factor of 2 up and down to quantify uncertainty based on this choice.

2.3.6 PDFs and PDF Uncertainty

To produce *ep* predictions, hard scattering functions must be convolved with PDFs. Calculations in this thesis were performed using the ZEUS-S[30] parameterization of the proton PDFs. PDFs must be experimentally determined, and contain both theoretical and experimental uncertainties. To understand the experimental uncertainty of the PDFs effect on results, calculations were performed using multiple different sets of PDFs, each of which contains different experimental input. To understand the theoretical uncertainty involved in the choice of parameterization, alternative calculations were performed using the CTEQ6[31, 32] and MRST [33].

2.3.7 Systematic Uncertainty Estimate for the Calculations

No alternative $\mathcal{O}({\alpha_s}^2)$ calculations exist for CC DIS processes at this time. It is therefore not possible to produce a direct estimate of the uncertainty introduced by our choice of MEPJET. However, because MEPJETalso produces NC DIS calculations, and because alternative NLO programs for these processes exist, we can compare NC DIS predictions, and consider the difference an estimate of the uncertainty introduced

from the use of MEPJET. It was observed in [34] that while MEPJETand the alternative program DISENT [35] agree for inclusive NC DIS jet cross sections on the order of 1%, the relative disagreement for NC DIS dijet cross sections is on the order of 5%.

2.3.8 Correction of the Calculations to the Hadron Level

The calculations described above produce cross sections of jets of partons. These cross sections are described as representing the *parton level*. In order to compare these predictions from cross sections which were measured, these cross sections were corrected to describe jets of hadrons. The resultant cross sections are said to describe the *hadron level*. This was perfromed using the event simulations described in chapter 5, and the techniques used to accomplish this are described in detail in chapter 7.

Chapter 3

Experimental Setup

3.1 The DESY Laboratory

The analysis presented in this thesis was performed with data from the ZEUS detector, which was situated on the Hadron-Elektron Ring Anlage (HERA), at The Deutsches Elekronen-Synchrotron (DESY) Laboratory in Hamburg Germany. DESY is part of the Helmholtz Association, and has two locations in Germany: one in Hamburg, and one in Zeuthen. DESY's facilities are used primarily for the study of natural sciences, specifically pertaining to the use of particle accelerators of varying size to probe the structure of matter. DESY hosted on average approximately 3000 scientists from 33 different countries for research related to HERA and HASYLAB, the associated syncrotron complex.

3.2 The HERA Accelerator

HERA was the world's first and only lepton-nucleon beam collider, and was the largest accelerator at the DESY complex. A nearly circular construction with a circumference of 6.3km, HERA was approved for construction in 1984, and built between

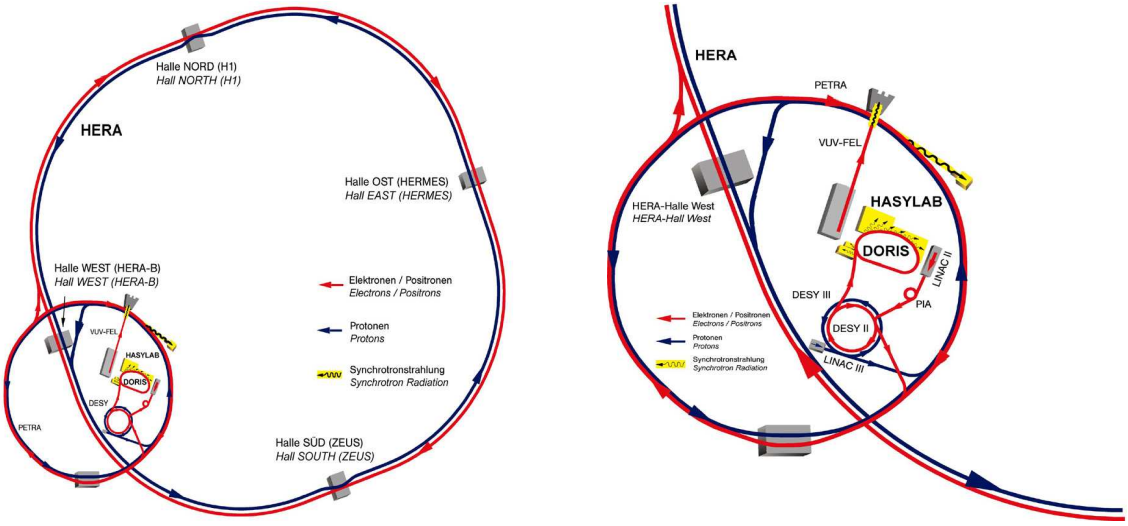

Figure 3.1: Schematic of the DESY Accelerator Complex

1984 and 1991. The commissioning of the electron ring and proton ring occurred in 1989 an 1991, respectively. HERA provided luminosity to its experiments from mid 1992 until 2 July, 2007, when it was decommissioned. Figure 3.1 is a schematic representation of HERA and the pre-accelerator elements. Particles were produced at low energies, and sequentially passed between different pre-accelerators before reaching HERA, as described below.

3.2.1 Proton Injection and Acceleration

To produce protons for collisions, hydrogen gas was ionized and accelerated in the LINAC III linear accelerator to 50 MeV. The ions were passed through a thin metal

foil to strip the remaining electron, and passed to the DESY III syncrotron for further acceleration to 7.5 GeV. DESY III is a 317 m circumference storage ring which could hold up to 11 proton bunches with approximately 10^{11} protons per bunch. From DESY III, protons were injected into PETRA II, which accelerated bunches up to 40 GeV. Protons were then injected into HERA for acceleration up to and maintained at their final energy. HERA operated at several different proton energies during its lifetime, but all data presented in this thesis arise from collisions with 920 GeV protons.

3.2.2 Lepton Injection and Acceleration

During periods of electron-proton collisions, electrons were produced by a hot metal filament. During periods of positron-proton collisions, positrons were produced by scattering electrons on tungsten sheets, resulting in the production of e^+e^- pairs by Bremsstrahlung. HERA provided both electron-proton and positron-proton collisions during separate periods. Throughout the rest of this chapter, the term *electron* will denote separately to either electrons or positrons, unless otherwise stated. After production, electrons were accelerated up to an energy of 450 MeV in the LINAC II accelerator, which is a 70 m linear accelerator. They were then gathered in PIA, a 29 m accumulator. Bunches of approximately 3.5×10^{10} electrons were then injected into DESY II, a 293 m circumference synchrotron, which accelerated them to an energy of 8 GeV. From DESY II, electrons were injected into PETRA II, a 2.3 km circumference synchrotron, which accelerated bunches to 12 GeV. Electrons were then injected into HERA, and were accelerated to and maintained at an energy of 27.5 GeV.

3.2.3 Beam Circulation and Collisions

Within HERA, electron and proton beams were stored in separate beam pipes, each with a vacuum pressure of approximately 3×10^{-11} Torr. The bunches circulated in opposite directions, with a separation of approximately 28.8 m, which in time is 96 ns, and a frequency of 10.4 MHz. HERA could theoretically have held 210 electron and 210 proton bunches, but in practice about 10 bunches of each type were left unfilled to so that a filled bunch of the opposing type could circulate without collisions. This allowed the HERA Machine group to study beam dynamics separately from interactions. Additionally, approximately 15 successive bunches of each type were left unfilled to allow time for deflection magnets to energize for beam dumps.

At two places on the ring, labled north and south halls in Figure 3.1, the two beam pipes merged into one and the beams were brought together with nearly zero crossing angle. Two experiment halls were located at the intersection points, providing space for the general purpose detectors H1 and ZEUS. Two other experiments, HERMES and HERA-B detectors were located at experiment halls labeled east and west, respectively. HERA-B studied collisions between the proton beam and wire targets to study B hadron production, while HERMES studied collisions between the electron beam and a proton gas jet to study the spin structure of the proton.

Between 1992 and 1997, HERA collided 27.52 GeV leptons with 820 GeV protons, providing ep collisions with a CME of $s \approx \sqrt{4E_pE_e} \approx 300$ GeV. The energy of the protons from 1997 to 2007 920 GeV, ep collisions with a CME of approximately 320 GeV. During the last periods of operation in 2007, The proton energy was lowered to 450 and 575 GeV, in order to investigate a previously unexplored region of phase

space.

3.2.4 HERA Luminosity

HERA began operation providing electron-proton collisions, and has alternately provided positron-proton collisions as outlined in Table **??**. The *Instantaneous luminosity*, L can be described as the incoming flux of particles participating in a reaction. At a two-particle intersecting storage ring collider like HERA, this can be estimated as $L = f\,(N_1 N_2/A)$, where f is the frequency of bunch crossings, N_i is the number of particles in each bunch in beam i, and A is the area of overlap of the two beams. Thus, the instantaneous luminosity of HERA based on its design characteristics would be

$$L_{HERA} = f\frac{N_1 N_2}{A} \approx 10.4 \times 10^6 \frac{10^{20}}{3.36 \times 10^{-5} cm^2} = 3.1 \times 10^{31} cm^{-2} s^{-1} \tag{3.1}$$

The average specific luminosity during the period 1992 to 2000 was approximately 2×10^{31} cm^{-2} s^{-1}. Between 2000 and 2002, HERA underwent a luminosity upgrade, which was primarily achieved by installing improved focusing magnets which diminished the interaction area of the two beams. The periods before and after the upgrades are referred to as *HERA I* and *HERA II*, respectively. The resulting specific luminosity for HERA II was approximately 3.8×10^{31} cm^{-2} s^{-1}. Direct detection of the instantaneous luminosity during HERA operation is described in section 3.3.3.

3.2.5 Polarized Collisions

The electron beam at HERA became naturally polarized transversely polarized due to the Sokolov-Ternov effect[36]. The characteristic build-up time expected for the HERA accelerator was approximately 40 minutes. During the 200-2002 luminos-

ity upgrade, spin rotators on either side of the H1 and ZEUS detectors were installed to change the electron polarization from transverse to longitudinal and back, providing collisions with longitudinally polarized electrons. Measurement of the electron polarization is described in section 3.3.3.

3.3 The ZEUS Detector

The ZEUS detector was a general purpose detector designed for studying various aspects of electron-proton scattering, and was located at the HERA south experiment hall. It was constructed from several independent subdetectors, which were built by universities from more than 11 countries.

The ZEUS collaboration used a right-handed cartesian coordinate system to describe the design and operation of the ZEUS detector. The origin is located at the nominal interaction point, the positive z-axis pointed in the direction of the proton beam, the positive y-axis pointed upwards, and the x-axis pointed toward the center of HERA. The polar angle, θ, is defined by 0° in the direction of the proton beam, and 90° in the direction of the positive y-axis. The azimuthal angle, ϕ is defined as being 0° in the direction of the positive x-axis, and 90° in the direction of the positive y-axis. The direction of positive and negative z will sometimes be referred to as *forward* and *backward*, respectively. Objects in these halves of the coordinate system will be described as being in the *front* and *back* of the detector, respectively. Because the central part of the ZEUS detector is cylindrically shaped, objects this region will be referred to as in the *barrel*.

The ZEUS detector was built around the HERA beampipe at the nominal interaction point, and was roughly symmetric in ϕ. The most central components were,

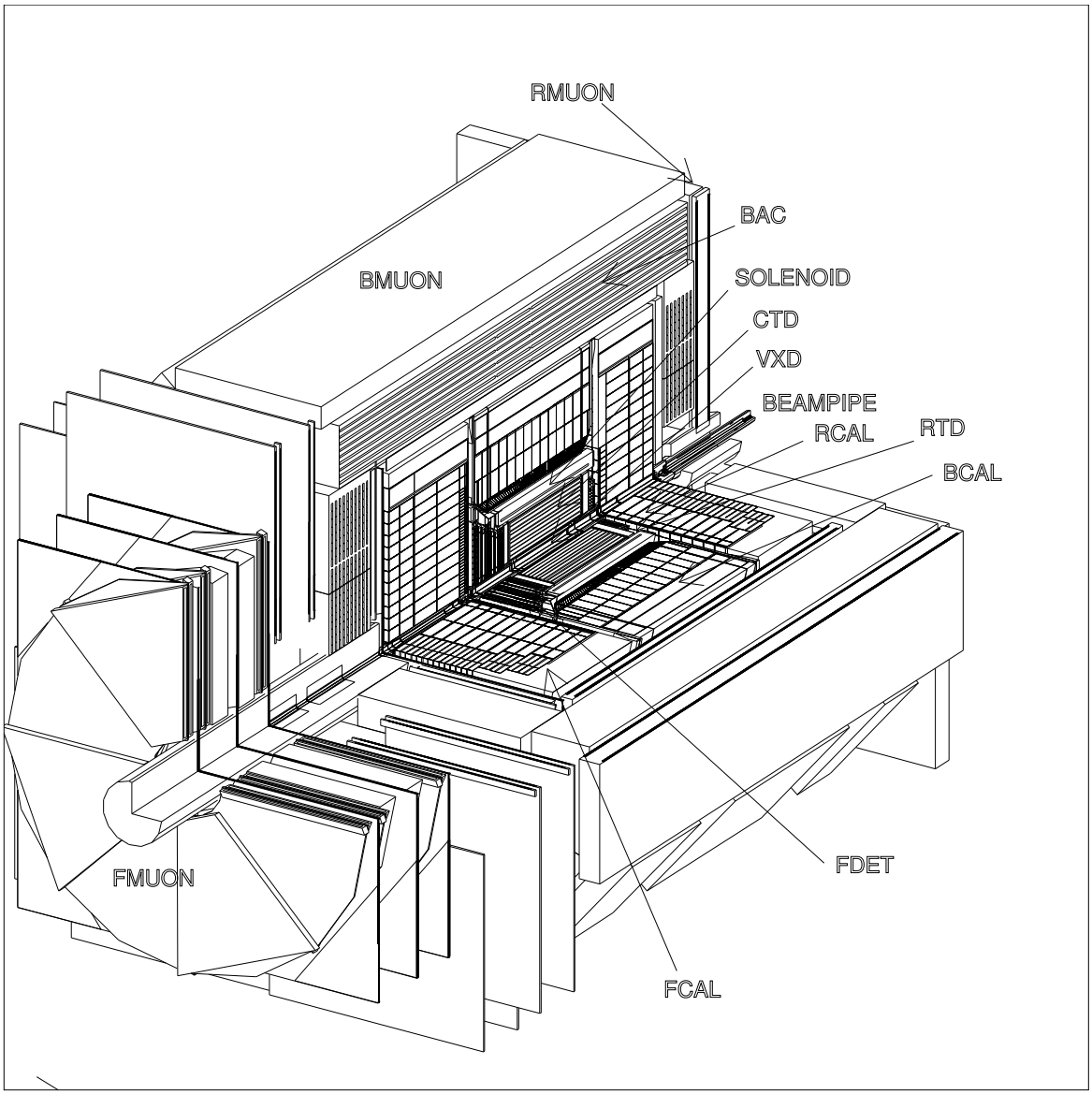

Figure 3.2: A Diagram of The ZEUS Detector

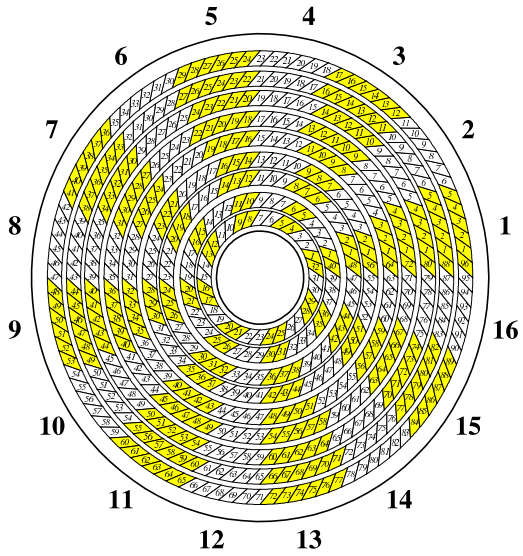

Figure 3.3: A Diagram of The ZEUS CTD, as viewed in the direction of the electron beam.

in order from the beam pipe to the outside, the micro-vertex detector, tracking system, toroid magnet, and calorimeter. These components were directly used in this analysis and will be described in more detail in the sections which follow. Around the calorimeter are the iron yoke/backing calorimeters, muon chambers, and the concrete encasement. In the negative z direction, in the direction which protons enter the detector, the "veto wall" detector was located to cancel the recording of data caused by particles associated with the proton beam, but not caused by ep interactions.

3.3.1 ZEUS Tracking Detectors

During the period of data taking relevant to this thesis, the tracking system of the ZEUS detector consisted of a silicon vertex detector, Three drift chamber detectors, and a straw-tube tracker. The drift chamber tracking detectors covered three regions: the forward (FTD), barrel, or central (CTD), and rear (RTD). The CTD is of greatest

importance to this thesis, and the FTD and RTD will not be discussed here.

The silicon-strip micro vertex detector (MVD), was installed in 2001 during the HERA upgrade shutdown. The MVD was designed to improve the overall precision of the tracking system and allow the identification of events containing secondary vertices from decays of long-lived particles[37]. The MVD was split into two sections: barrel (BMVD) and forward (FMVD).

The BMVD was 64 cm long and covers a polar angle between 30° and 150°. It consisted of three layers of silicon sensors arranged in concentric planes around the interaction point. The inner layer was placed at a radius between 3 and 5 cm from the CTD axis. Because of space restrictions cause by the elliptical beam pipe not being centered on the interaction point, the inner layer did not completely surround the beam pipe in ϕ. The second and third layers were placed at r=8.6 cm and r=12.3 cm, respectively, and each completely surrounded the beam pipe in ϕ. The BMVD was equipped with 600 single-sided strip silicon sensors of approximately 64×64 mm^2 and 320 μm-thick with p+ strips implanted into n-type bulk. Each sensor was covered with 3082 strips with a pitch of 20 μm. Two sensors were glued together next to each other with perpendicular strips on the same side. When placed in the barrel MVD, the sensors parallel to the beam pipe give the $r - \phi$ coordinate of a hit while the perpendicular ones gave the z information.

The FMVD consisted of four planes referred to as wheels, which were perpendicular to the beam axis. The four wheels were positioned at z=32, 45, 47 and 75 cm. Each wheel consisted of two back to back layers of 14 silicon sensors of the same type as in the barrel section but with a trapezoidal shape. There were 480 readout strips

per sensor. The FMVD extended the polar coverage of the MVD down to 7°.

The CTD was a cylindrical drift chamber which is filled with a mixture of argon, CO_2 and ethane. It had an active volume with length 205 cm, inner radius of 18.2 cm and an outer radius of 79.4 cm, covering a polar angle range from 15° to 164°. It was divided into eight sections called *octants*, which occupied 45° of azimuthal angle each, spanning the entire length of the CTD, this is depicted in figure 3.3. Each octant was divided into nine radial *super layers*, numbered one to nine, numbered from central to exterior. Each odd-numbered superlayer contained wires which were parallel to the beam axis. Each even-numbered superlayer contained wires which were tilted relative to the beam axis by an angle of 4.98°, −5.53°, −5.51°, and 5.62° for layers 2,4,6,8, respectively. These angles are referred to as a *stereo angle*, because the path of particles which caused a signal in two adjacent superlayers could be identified within 2 mm in the z direction.

The CTD operated in a $1.43T$ magnetic field, which caused charged particles to arc as they passed. The momentum and charge of the particles could then be determined by this curvature. As particles passed though the CTD, they imparted energy to the gas, and their energy loss as a function of distance, $\frac{dE}{dx}$, was also used in particle identification.

3.3.2 The ZEUS Calorimeter

Similar to the Tracking system, the ZEUS uranium calorimeter (CAL) was constructed in three separate parts: forward (FCAL), barrel (BCAL), and rear (RCAL). This is depicted schematically in Figure **??**. These covered polar angles of $2.2° - 39.9°$, $36.7° - 128.1°$, and $128.1° - 176.5°$ respectively. Each of these three main main regions

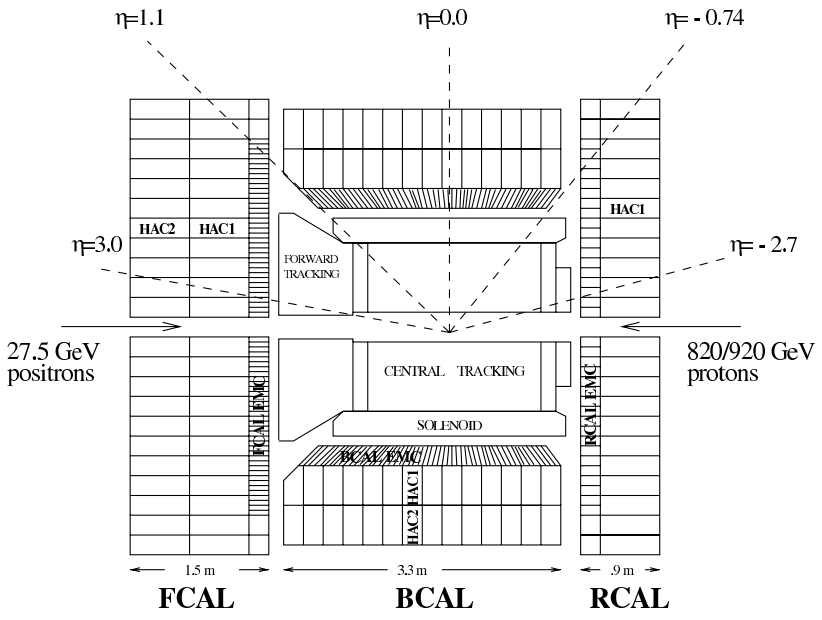

Figure 3.4: A z-y schematic diagram of the ZEUS Calorimeter.

were constructed from independent sections called *modules*, which were further divided into sections called *CAL towers*, which were then divided into *cells*. Each tower in the CAL was subdivided into electromagnetic *EMC* or hadronic *HAC* sections. In the FCAL and BCAL Each EMC section contained four longitudinal separations into EMC cells, while each HAC section was transversely separated into two HAC cells. In the RCAL each tower contains only two EMC cells and one HAC. In terms of readout, cells are the most fundamental unit of the CAL. Each cell was roughly shaped like a rectangular prism, and was constructed of alternating layers of 3.3 mm thick absorber plates and 2.6 mm thick plastic scintillator. Each absorber plate was constructed by encasing the depleted uranium ^{238}U in a steel jacket. Incident particles on the absorber showered, producing many more particles, which stimulated the scintillator tiles, producing light. Light from the scintillators was passed from two opposite sides of each

cell along two separate wavelength shifters. Each wavelength shifter was attached to one photo-multiplier tube (PMT), located on the exterior of the CAL. The two PMTs for each cell were labled as *left* and *right*. Using timing information between left and right channels for each cell, improvement in three dimensional positioning could be made. The agreement between pairs of PMTs also allowed a systematic check of response, and redundancy in case of noise.

^{238}U was chosen as absorber material for its density, stability, radiation-hardness and its own natural low level radiation. This low radiation provided a stable and well understood signal for calibration of the readout. Hadrons incident on ^{238}U create a high number of spallation neutrons, which can then excite the hydrogen nuclei of a scintillator. Electrons do not radiate the same manner because they mostly interact with atomic electrons, rather than nuclei. These EM interactions typically produce photons and e^+e^- pairs. The CAL was designed with a careful balance between the quantity of uranium and steel in each absorber plate which allowed the CAL to reach a nearly equal response from hadronic and leptonic energy. Test beam studies showed the response to be equal within 3%. This is improtant for jet physics, because it removes the need for assumptions about the leptonic and hadronic content of jets. The single particle energy resolution for electrons and hadrons was determined in test-beams to be $\frac{\sigma_E^e}{E} = 18\%/\sqrt{E}$ and $\frac{\sigma_E^h}{E/\mathrm{GeV}} = 35\%/\sqrt{E/\mathrm{GeV}}$, respectively [38]. This can be contrasted with the equivalent H1 energy resolutions of $\frac{\sigma_E^e}{E} = 12\%/\sqrt{E}$, $\frac{\sigma_E^h}{E} = 50\%/\sqrt{E}$ [39, 40].

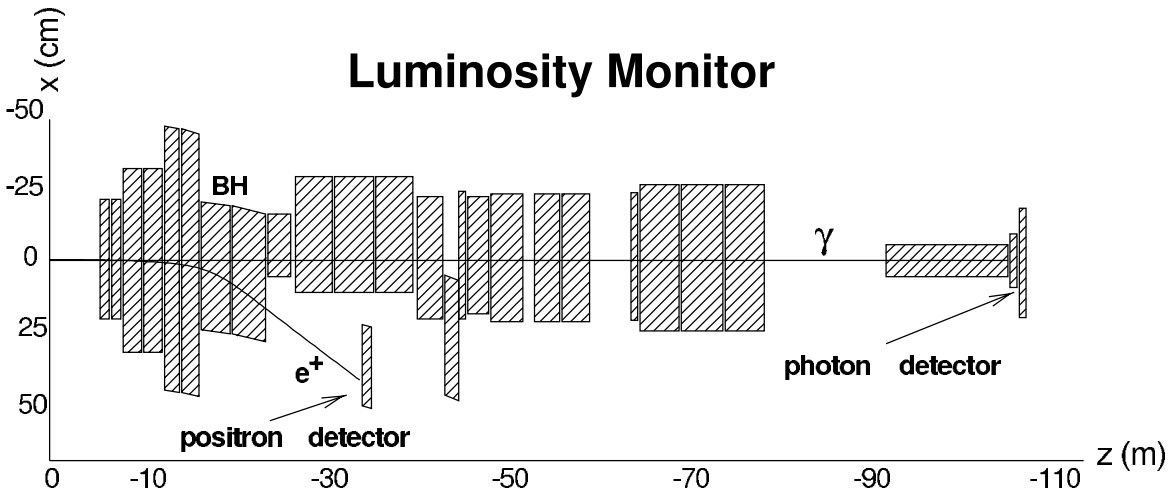

Figure 3.5: Schematic of the ZEUS Luminosity System.

3.3.3 Luminosity Monitor and Polarimeters

The *luminosity* of a data sample, $L = N/\sigma$, is defined as the number of particles produced from a process, divided by the cross section for that process. Thus in order to determine a cross section from experimental data, one must know the luminosity used to generate that measurement. At HERA, the luminosity of ep collisions was determined by measuring the rate of Bremsstrahlung photons from the Bethe-Heitler process $ep \to ep\gamma$. The theoretical cross section for this process is known to an accuracy of .5%, so a precise measurement of this process allowed a precise measurement of the luminosity.

The Bethe-Heitler measurement was performed at -107 m in the ZEUS coordinate system by a lead-scintillator calorimeter, depicted in Figure **??**. The lumi-γ system, gathered photons with a polar angle $\theta_\gamma < 0.5$ mrad with an test-beam energy resolution of $18\%/\sqrt{E}$ [41]. It was determined that the protective carbon/lead synchrotron radiation filter caused a slight degradation of performance to $18\%/\sqrt{E}$. The

lumi-γ detector had 1cm scintillator strips located $.7\chi_0$ inside, granting the ability to resolve the impact position of photons to .2cm in x and y. This system was also used to measure the electron beam-tilt and measure photons from initial-state radiation (ISR). In addition to the lumi-γ calorimeter, a second lead-scintillator calorimeter called lumi-e was located at $-27m$, which captured electrons which were deflected from the beam by the HERA bending magnets. This was originally designed to compliment the lumi-γ system, but was found to be unnecessary for luminosity measurement. The total uncertainty in the luminosity measurement was determined for this analysis to be 2.5%.

The electron beam polarization was measured using two independent polarimeters, referred to as the longitudinal polarimeter (LPOL) and transverse polarimeter (TPOL). Both devices exploited the spin-dependent cross section for Compton scattering of circularly polarized photons off of electrons. The polarimeters were able to measure the polarization in times much shorter than the polarization build-up time.

3.3.4 Veto Wall and C5 Counter

The veto wall is was a large wall of iron positioned -7m, designed to shield the ZEUS detector from particles produced in the proton beam halo. It measured $8 \times 7.6 \times 0.86$ m, with a square hole of dimension 0.95 m at the center to accommodate the beam pipe and magnets. Scintillators on either side of the wall provided information about the rate of incident particles, allowing veto information for events contaminated by these particles. The C5 counter was a scintillator attached to the C5 collimator at $z = -3.15$ m which provided timing information used to synchronize the HERA and ZEUS clocks. The C5 counter also provided veto information for beam halo

interactions.

3.3.5 Trigger and Data Acquisition

Assuming that ZEUS recorded one event from every crossing, it would have produced data at a rate of approximately 1 MB $\times$ 10MHz= 10TB/s. Because the data transmission from the detector to the event reconstruction computing farm (described in the next section) was less than 1MB/s, the rate of data was forced to be reduced by a factor of 10^6. A faster transmission rate would not have been beneficial, because not every crossing produced an *ep* interaction, and some that did produced products deemed uninteresting, or which were contaminated by signal from non-*ep* sources. Deciding which events were worth full reconstruction and storage was accomplished by the a 3-level trigger system, depicted in Figure 3.3.5. The ZEUS First Level Trigger (FLT) was a digital hardware trigger, designed to reduce the event rate to $1kHz$. In order to hold the data while electronics make a decision, raw data was stored on the detector in an analog pipeline for $5\mu s$. This allows a decision to move data off the detector to be made roughly every 50 bunch crossings. The time during the first 25 of these 50 crossings is allocated to individual component FLTs. The rest of the cycles are given to the Global First Level Trigger (GFLT), which collected decisions from the subdetector-specific FLTs, and issued global accept or abort requests. This was performed with almost zero deadtime. If a particular event was accepted by the FLT, it was then digitized and transferred to the Second Level Trigger (SLT). Due to finite transfer of data between the components deadtime occurs here at $1-2\%$ The SLT used more complete information than the first level trigger. It was designed to reduce the event rate to less than $100Hz$. Similarly to the FLT, each subdetector has its

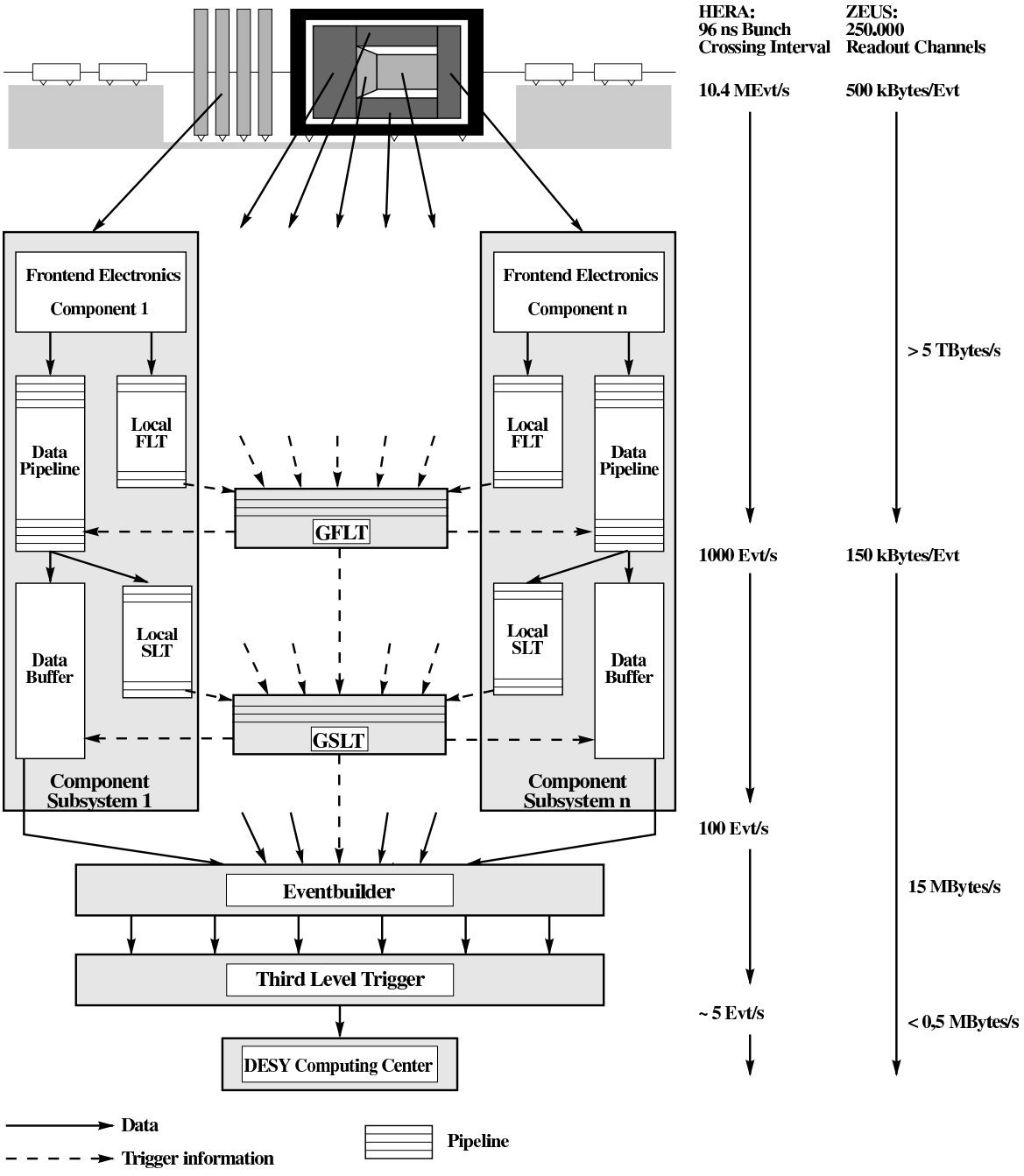

Figure 3.6: Schematic of the ZEUS System System.

own SLT which passes information to the Global Second Level Trigger (GSLT). If the event is accepted by the SLT, all components send all information to the event builder (EVB), which then combines all data into a single event record to ADAMO database tables.

Data was then passed to the Third Level Trigger (TLT), which was a purely software based trigger. The TLT partially reconstructed kinematic variables, and reduced the eventrate to 1Hz. If the event was accepted by the TLT, then it was passed to the ZEUS Physics Reconstruction Program (ZEPHYR), which uses calibration constant tables for each component to interpret detector signals as energies, times, and positions, and the event was written to data tape for storage and analysis.

Chapter 4

Event Reconstruction

Events from the ZEUS detector which passed the FLT, SLT and TLT triggers were written to tape for storage and later analysis. Reconstruction of events begins with the EVB (see section 3.3.5.) which combined all detector signals from the event into a single ADAMO table entry. Entries were then processed by the ZEPHYR program, which used calibration constant tables for each component and each run to interpret detector signals as energies, times, and positions. Offline analysis in this work was performed using the ORANGE (Overlying Routine or Analysis Ntuple GEneration) software framework, which is based on EAZE (Effortless Analysis of ZEUS Events). ORANGE and EAZE provide routines which retrieve data records, perform specialized and modifiable reconstruction of event variables, integrate the CERN libraries, and perform basic event selections.

4.1 Track and Vertex Reconstruction

While the nominal interaction point for *ep* interactions is at the origin of the ZEUS coordinate system, finite dimensions of the beam bunches caused real interactions to occur with a spread in all three dimensions. Information from the tracking

components of the ZEUS detector were used to reconstruct the tracks of individual charged particles and estimate the location of the initial ep interaction. This is performed using the VCTRACK [42] program. The VCTRACK package uses information from all tracking detectors, with primary information coming from the CTD. Track finding begins with CTD seeds, each of which contains three neighboring hits in the outermost axial superlayers of the CTD. Each seed is extrapolated iteratively towards the inner superlayers, aided by a "virtual hit" which is fixed to the beam line. As hits are added to the tracks, trajectory parameters of each track are recalculated with each iteration. Tracks that share 15% or more of their hits with other tracks at any stage are removed. An initial estimate of the z-position of each hit from the z-by-timing information is used, which is later refined using stereo superlayer hits. The next step of reconstruction proceeds by extrapolating the innermost hit of each track outward. Fitted tracks are then used as input to an algorithm which tests candidate primary and secondary vertices. Vertices are then chosen based on a χ^2 minimization routine, and tracks matched to the primary vertex are then refitted using the primary vertex as a starting point. For all events in the study, the x and y vertex positions were set to 0 after track fitting and electron finding, which is described in section 4.3.

4.2 Calorimeter Reconstruction

Information from the ZEUS calorimeter was used to reconstruct the energies and positions of particles. Each cell provides pulse amplitude and timing information from two PMTs, which are compared to ensure accuracy and provide improvements in position reconstruction. Several sources of uncertainty enter the calorimeter reconstruction. These include noise from uranium absorber decays, noise from readout

electronics and PMT *sparks*, which occurred when the high voltage from a PMT discharged spontaneously. The behavior of each PMT was monitored during operation and calibrations to ensure proper functioning, PMTs listed in a table of unreliable PMTs for each run were ignored during reconstruction. To suppress uranium radiation in reconstruction, EMC cells with $E < 80$ MeV and HAC cells with $E < 140$ MeV were neglected. To suppress PMT sparks, cells were ignored if the imbalance between left and right PMTs, $I_{\text{cell}} = \left|\left(E_{\text{L}} - E_{\text{R}}\right) / \left(E_{\text{L}} + E_{\text{R}}\right)\right| > 0.7$, and that cell had an average energy greater than 700MeV. Cell selection was performed in this analysis by the ZEUS Noise04s routine.

Simulations of the energy response of the CAL differ from that of the true response [43]. While this could be corrected by adjusting the energy values of the simulation, historically this is performed by altering the final CAL cell energies in the ZEUS data. For each FEMC cell, the energy was multiplied by a factor of 1.024. The same procedure was performed using factors of 0.941 for FHAC, 1.053 for BEMC, 1.096 for BHAC, and 1.022 for all RCAL cells. No adjustment to calorimeter cell values was applied to MC events.

4.3 Electron Reconstruction

A major source of background to CC DIS is NC DIS, which has a principle signal as an isolated electron deposit located in the calorimeter. In order to reject events arising from NC interactions, the electron finder Sinistra95 [44] was applied to all events. Sinistra is a neural network which has been trained on simulated low-Q^2 NC DIS data to produce the best separation between electromagnetic and hadronic energy deposits by using the properties of shower profiles to establish the characteristics of

the initiating particle.

Scattered particles such as single electrons often deposit their energy into more than one calorimeter cell, and often in ways which involve cells in both the BCAL and RCAL. Before input into SINISTRA, groups of calorimeter cells called *islands* [44] were formed, where each island is a potential deposit from an electron. The 17 inputs to the neural network were the total energy of the cells in the island, and 16 showering profile parameters called Zernike moments and Legendre functions. The output of SINISTRA is a real number between 0 and 1, which is interpreted as a liklihood that the island in question resulted from an isolated electron. Clusters with SINISTRA output near one are considered to be electron-like. In this analysis, only the candidate with greatest SINISTRA liklihood was considered, and events were only considered to have a candidate if the liklihood was greater than 0.9. The reconstructed energy of an electron candidate was the sum of the cell energies in its island, and the position of the candidate was determined from the energy weighted island center. For candidates with liklihood greater than 0.9 and energy greater than 10GeV, SINISTRA was estimated to have 80% purity and nearly 100% efficiency [45].

4.4 Kinematic Reconstruction

Basic kinematic quantities were reconstructed from the calorimeter energy deposits, which were treated as massless particles.

$$\text{Total energy} \;:\; E_{\text{CAL}} = \sum_i E_i \tag{4.1}$$

$$\text{Longitudinal momentum in the CAL} \;:\; p_z = \sum_i p_{z,i} \tag{4.2}$$

$$\text{Transverse momentum in the CAL} \;:\; p_{T,\text{CAL}} = \sqrt{\left(\sum_i p_{x,i}\right)^2 + \left(\sum_i p_{y,i}\right)^2} \tag{4.3}$$

$$\text{Cosine of hadronic system angle} \;:\; cos\gamma_h = \frac{p_T^2 - (E-p_z)^2}{p_T^2 + (E-p_z)^2} \tag{4.4}$$

In charged current interactions at ZEUS, the exiting neutrino escapes detection, requiring kinematic quantities to be reconstructed from the hadronic system alone. To prevent bias in our estimation of these values due to particles which escape detection down the beam pipe, the Jaquet-Blondel method [46] of reconstruction was used. This method relies only on the transverse momenta, p_T and difference in energy and z-component momenta, $E - p_z$ of each particle, which are small for particles scattered near the beamline. The reconstructed values of Q^2, x, and y are:

$$\begin{aligned} y_{\text{JBCAL}} &= \frac{E-p_z}{2E_e} \\ Q^2_{\text{JBCAL}} &= \frac{p_{T,\text{CAL}}}{1-y_{\text{JBCAL}}} \\ x_{\text{JBCAL}} &= \frac{p_T}{s y_{\text{JBCAL}}(1-y_{\text{JBCAL}})}. \end{aligned} \tag{4.5}$$

4.5 Jet Reconstruction

Calorimeter cells were combined using the k_T cluster algorithm [47] to form jets of calorimeter cells. The algorithm was also used to cluster jets of hadrons and partons

in the simulations, so in this section we will refer only to "objects" being clustered for generality. All clustering objects were considered massless. The algorithm defines the distance of each particle from the beam line as $d_i = E_{T,i}^2$, and the distance between two objects as $d_{ij} = \min\left(E_{T,i}^2, E_{T,j}^2\right) \times \left[(\eta_i - \eta_j)^2 + (\phi_i - \phi_j)^2\right]$. The algorithm begins by identifying $\min(d_i, d_{ij})$. If $d_{kl} = \min(d_i, d_{ij})$ for some k, l, then objects k, and l are merged into a cluster (here indexed as m) with properties

$$\begin{aligned} E_{T,m} &= E_{T,j} + E_{T,k} \\ \eta_m &= \frac{E_{T,j}\eta_j + E_{T,k}\eta_k}{E_{T,j} + E_{T,k}} \\ \phi_m &= \frac{E_{T,j}\phi_j + E_{T,k}\phi_k}{E_{T,j} + E_{T,k}}. \end{aligned} \tag{4.6}$$

If $d_n = \min(d_i, d_{ij})$ for some n, then object n is considered a jet, and no longer participates in the merging procedure. In this analysis, the k_T algorithm was applied in the lab frame in inclusive mode, meaning that all objects are merged into jets. Phase space requirements were applied to each jet, neglecting objects outside acceptance or poor reconstruction, which is described in section 6.3.3.

Chapter 5

Event Simulation

The calculations presented in chapter represent jets of partons, while the data which were collected represent jets of hadrons. In order to compare these, we must translate the predictions of partons onto predictions for hadrons. Moreover, the data as immediately taken from the readout includes detector specific effects which we must correct for in order to compare our data with predictions, or with other experiments. In order to accomplish these two goals, Leading Order MC (MC) simulations were employed. The MC used here simulates individual events in the ZEUS detector in several steps.

For each event, points in a predetermined phase space are selected, and leading order electron-quark matrix elements are combined with a PDF parameterization to produce a list of partons for the event. This is referred to as the hard scatter, and the information about this list of exiting partons is said to describe the event at the *parton level*. Then, a phenomenological model is employed to approximate hadronization for the partons, and the resulting list of hadrons is said to describe the event at the *hadron level*. Lastly, a complete simulation of the detector, including material interactions, magnetic fields, detector components, trigger, and data readout is used to simulate how the detector would respond to each event. The information produced by the detector

simulation is of the same structure as the data taken from the actual detector, and is analyzed in the same way. This information is said to describe the event at the *detector level*.

5.1 PDF and Hard Scatter

The incoming state of the simulated event is an electron and proton, which will interact via the protons partons. Which flavor parton will interact, and the x and Q^2 values of the interaction is determined by the proton PDFs and a pseudo-random number generator[1]. The PDFs in this analysis come from the Coordinated Theoretical-Experimental Project on QCD (CTEQ5D) [48], Martin Roberts Stirling Thorne (MRST) [49], and The ZEUS Collaboration [50].

The relative probability of processes were computed to leading order, which were stored in tables for efficient recall. Pseudorandom numbers are generated select from these processes. This component represents the hard scatter, after which the event contains an outgoing neutrino, one or two outgoing quarks or one gluon. and the proton remnant. The available outgoing states in the MC used in this analysis are depicted by the Feynman diagrams shown in section 2.4.1. All MC presented in this thesis used unpolarized matrix elements.

[1] A pseudorandom number generator is a deterministic algorithm for the production of numerical sequences which satisfy some statistical tests of randomness, such as uniform frequency and distribution of the numbers produced.

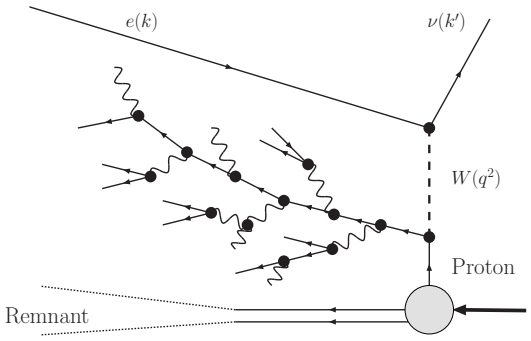

Figure 5.1: Schematic of MEPS

5.2 Parton Cascade

As described in section **??**, quarks and gluons are not observed in the detector, but instead undergo QCD radiation and hadronization. QCD radiation of hard-scatter partons is also called parton showering, and is an intrinsically non-perturbative process due to the low scales involved. Two methods of simulating a parton cascade will be considered here: Matrix-Element plus Parton Shower (MEPS) [51], and the Color Dipole Model (CDM) [52]. The MEPS approach generates parton showers from the DGLAP splitting functions. Partons become less virtual as they radiate and split until a predetertmined virtuality is reached, typically on the order of 1 GeV. This is represented in figure 5.1. Because the parton shower uses the DGLAP evolution equations, radiation is ordered strongly in decreasing k_T and increasing proton fractional momenta. Samples of LEPTO MC presented in this thesis employ MEPS as implimented via JETSET 7.4 [51, 53].

CDM describes the proton remnant and its dissociated parton as a color dipole. As the parton and remnant separate, the dipole energy increases until sufficient energy

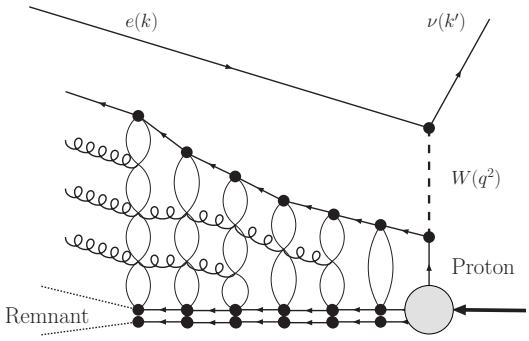

Figure 5.2: Schematic of CDM

is reached to radiate a gluon, which bifurcates the dipole. The two halves continue to stretch and split as more gluons are emitted. Unlike MEPS, CDM does not order its radiation in k_T. Samples of ARIADNE 4.08 [54] MC presented in this thesis employ CDM. This is represented in figure 5.2.

5.3 Hadronization

Free partons are never observed due to color confinement, so the partons simulated during the cascade phase discussed in section 5.2 must be converted into color singlet hadrons in order to describe physical data. This process is referred to as hadronization. Because it describes confinement, at scales of ($\mu \lesssim 1$ GeV) where α_s is large, it necessarily cannot be described by perturbative QCD. Several hadronization models are currently implimented in MC models, but only the Lund String Model [55] is used in the MC results presented in this thesis.

In the Lund String Model, the color field between a $q\bar{q}$ pair is represented as a linear potential, described as a flux-tube or string of gluons. Spatial stretching of this string results in a potential energy of $\approx$ 1 GeV/fm. If the initial $q\bar{q}$ pair separate

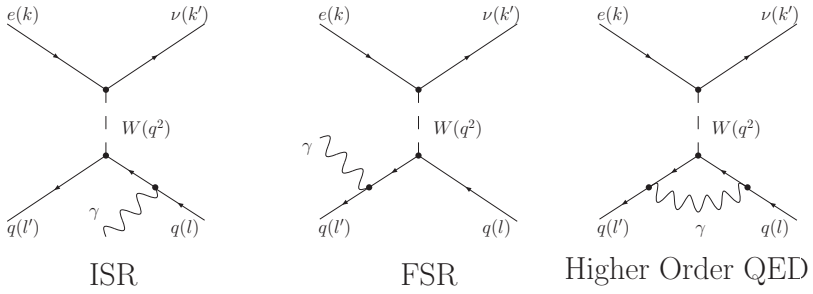

Figure 5.3: Feynman Diagrams for Higher Order QED Effects

sufficiently the color field will contain enough potential energy to produce a new $q\bar{q}$ pair. This is described in the model as occurring between the initial $q\bar{q}$ pair, as if the string had been cut. This mechanism produces quarks with an approximately gaussian p_T spectrum. This process continues until some preset cutoff, when the $q\bar{q}$ pairs have small enough relative kinetic energy to be considered on-shell hadrons. Groups of 2 and 3 quarks are then chosen to form mesons and hadrons.

5.4 Description of Initial- and Final-State QED Radiation

While MC models can generate interactions at fixed electron and proton energies. HERA data were produced with a broader kinematic spectrum, however, because of radiation of photons immediately before and after the hard interaction, as shown in figure 5.3. This type of process is referred to as initial- and final-state radiation (ISR/FSR). For this analysis, the MC implimentations used for event simulation were interfaced with the HERACLES 4.6.1 [56] program via DJANGO v1.3 [57]. The HERACLES program includes QED effects up to $\mathcal{O}(\alpha_{\text{EM}}^2)$. The physical parameters

used to compute QED effects were

$$\begin{aligned} \alpha_{\rm EM} &: 1/137.035999 \\ G_{\rm F} &: 1.664 \times 10^{-5}\ {\rm GeV}^{-2} \\ M_Z &: 91.1876\ {\rm GeV} \end{aligned} \tag{5.1}$$

5.5 Detector and Trigger Simulation

Once an event has been simulated to produce real particles with definite momenta, these particles are used as input into a full detector simulation. This simulation includes potential decays of short lived particles, the interactions with the active and passive materials in the detector, and the response of the electronics at all levels in the data-taking and reconstruction chain. Information for the modeling of the detector response comes from test-beam data, and the simulation is referred to as the MC *for ZEUS Analysis, Reconstruction and Trigger* (MOZART v2005a.1), which is based on GEANT v3.21[58].

The trigger simulation, called Complete ZGANA[2] Analysis Routine (CZAR v2005b.2) provides complete description of the ZEUS trigger system response to simulated events. The output of MOZART and CZAR is an ADOMO table of detector signals which is organized similarly to data from the ZEUS detector. The principle difference from real data is the additional information about the generator, parton,

[2]The ZEUS GEANT Analysis (ZGANA v1.5) and TLT_ZGANA are simulations of the ZEUS 1st+2nd and 3rd trigger systems, respectively. CZAR is the combination of the two, encompassing the complete trigger chain.

and hadronic portions of the simulation. These ADOMO tables were then submitted to the ZEPHYR program discussed in the beginning of chapter 4, and were reconstructed identically as the data were. This type of information is referred to as being at the *detector level*.

Chapter 6

Event Selection

6.1 Description of Data Sample

The data in this thesis were collected during the years 2004 to 2007. During this time, HERA provided collisions between protons and longitudinally polarized electrons (2005-2006), and collisions between protons and longitudinally polarized positrons (2004, 2006-2007). The luminosity collected versus lepton polarization is depicted in figure 6.1. From the figure, it can be observed that far more data was collected using left-handed longitudinally polarized leptons of either type, and that more data were collected for electron-proton collisions than for positron-proton.

6.2 Online Event Selection

As described in section 3.3.5, event selection during data taking was performed via a three level trigger system. As events were produced in the ZEUS detector, The trigger system was responsible for the decision to offload, reconstruct, and store event data from the detector. The two concerns of trigger selection is the decision that some physics event occurred in the detector, and that it was of the desired variety.

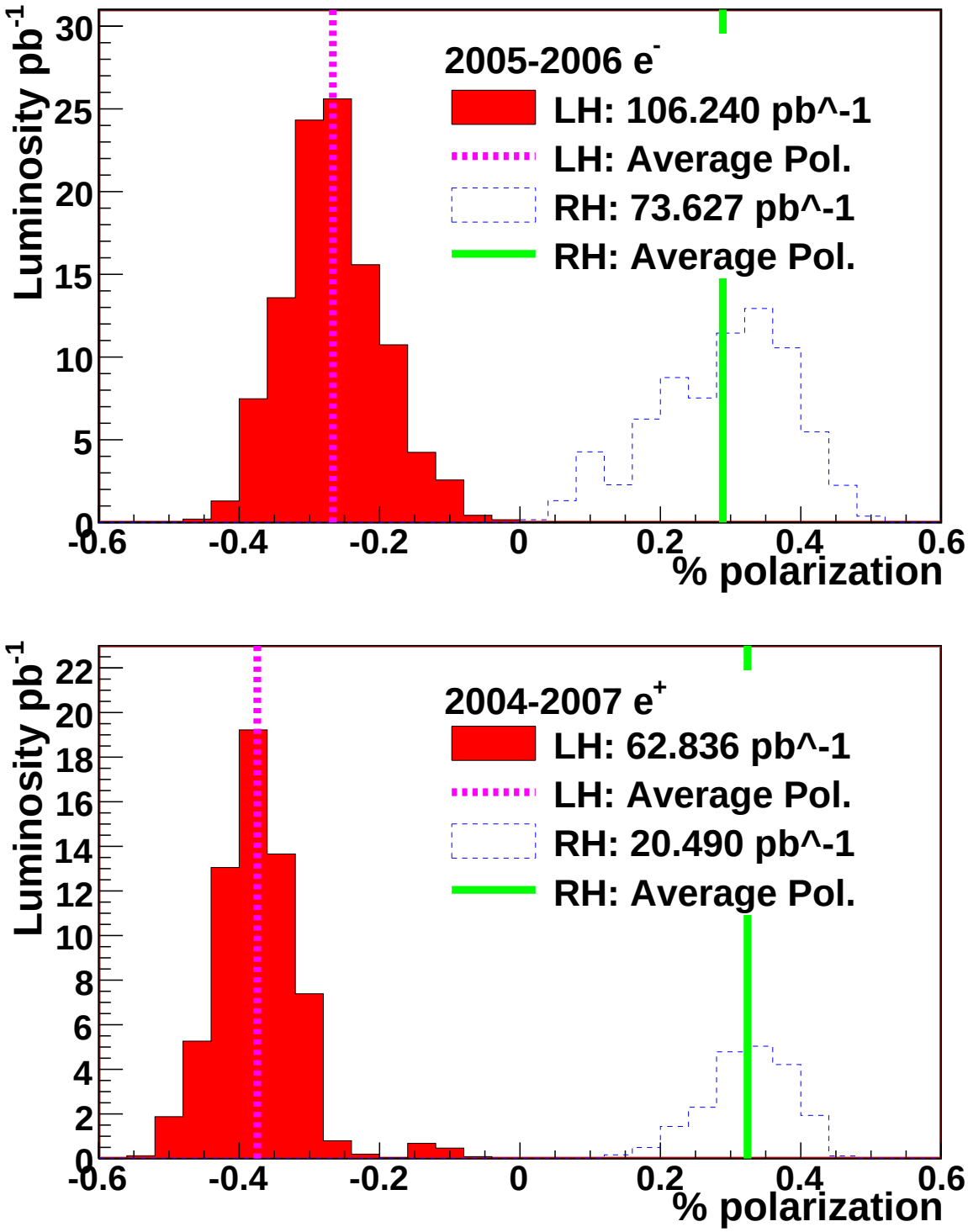

Figure 6.1: Luminosity vs. lepton polarization for data used in this analysis. The upper figure depicts data using electron-proton collisions only, while the lower depicts that for positron-proton collisions. Total integrated luminosity for each type of collision is stated in the legend, and the luminosity-averaged polarization is shown with vertical lines.

Figure 6.2: MISSING: Event Display of a Candidate Inclusive Jet Event

To this end, some trigger conditions examined the existence of energy or tracks in the detector, while others required more complicated conditions to be satisfied in order to remove background.

Two independent trigger selections were used in this analysis, and are referred to as the *principle* and *alternative*. The principle trigger selection was used to extract the cross sections, while the secondary was used to understand the systematic uncertainty introduced from trigger choice and operation. The principle selection has been previously tested and used in an inclusive HERA II CC DIS ZEUS publication [59]. The alternative trigger selection is derived from a HERA I CC DIS Jets publication [60]. The primary difference is that the alternative selection required the presence of jets, while the principle selection made no such constraint. The principle selection also required tracks, while the secondary relied more heavily on calorimeter quantities.

6.2.1 First Level Trigger Selection

The core conditions of both the principle and alternative FLT selections is the presence of large E_T in different subsections of the CAL, and the presence of CTD tracks which are consistent with *ep* interactions. The primary purpose of these requirements was to select true *ep* events over bunch crossing where no interaction occurred. Both selections also rejected events if deposits and timing information was consistent with beam-gas interactions. A detailed list of the trigger bits used in this analysis is given in appendix F.1.

6.2.2 Second Level Trigger Selection

One challenge of designing a trigger selection for CC DIS is that the signature of large $P_{T,\text{miss}}$ and E_T are also produced by beam-gas interactions. beam-gas typically deposits its energy near the beam pipe, so it is useful to select events based on the $P_{T,\text{miss}}$ and E_T not including these CAL cells. Thoughout this chapter, $E_T(-2IR)$ ($E_T(-1IR)$, $P_{T,\text{miss}}(-1IR)$) will refer to the transverse energy as measured by the calorimeter excluding the inner two rings (one ring) of cells closest to the beam pipe. The variable N_{gt} refers to the number of "good" tracks in the sense that they are reliably reconstructed, and originate from an area near the nominal vertex. This definition is specific to the ZEUS CTD, and is based on the number and distribution of hits used in the track fit. The requirement that the tracks come from near the nominal vertex helps differentiate between ep interactions and beam-gas, because beam-gas events often have tracks originating far from $z = 0$. In the principle SLT selection, events were required to satisfy the each of the following three conditions.

1. Proper timing and number of hits in the CTD

2. No deposits from off-momentum protons were detected

3. At least one of the following:

   (a) $P_{T,\text{miss}} > 6$ GeV and $E_T(-2IR) > 6$ GeV and $N_{\text{gt}} > 1$

   (b) $P_{T,\text{miss}} > 9$ GeV and $P_{T,\text{miss}}(-1IR) > 8$ GeV and $E_{FCAL} > 20$ GeV

   (c) $P_{T,\text{miss}} > 9$ GeV and $(P_{T,\text{miss}})^2 > 2.31 \times E_T$ and $E_{FCAL} > 80$ GeV

   (d) $E - p_z > 6$ GeV and $(P_{T,\text{miss}})^2 > 2.25 \times E_T$ and $N_{\text{gt}} > 1$

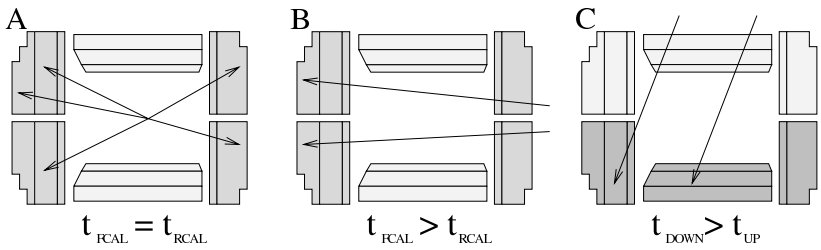

Figure 6.3: Schematic diagram of CAL timing information. Major scenarios include: A) Events originating near the nominal vertex. B) Events originating outside the detector near the beam-pipe. C) Events originating outside the detector far from the beam pipe.

Conditions 1 and 2 above attempt to reject non-*ep* events. Condition 3a and 3b selected events with large $P_{T,\mathrm{miss}}$ without being sensitive to beam-gas. Condition 3c and selected events with large $P_{T,\mathrm{miss}}$ which is large relative to the E_T of the event. This helped select CC DIS over PHP, as discussed in section 2.1.4.

The alternate selection required that all the following conditions were met:

1. $N_{\mathrm{gt}} > 1$

2. $P_{T,\mathrm{miss}} > 8$ GeV

3. $E_T(-1IR) > 8$ GeV

4. $P_{T,\mathrm{miss}}/E_T > 0.3$

In the above criteria, criteria 1 selected *ep* events, while selection 2 and 3 selected CC DIS over NC DIS. Selection 4 selected CC DIS over PHP.

A more detailed explanation of these criteria is given in table F.2.

6.2.3 Third Level Trigger Selection

In this section, the term *Up-Down CAL time difference* is used to indicate the difference of the time in which CAL hits were recorded in the upper and lower halves of the CAL. Quantities comparing CAL timing information are useful quantity because events originating in the center of the detector have $t_{\text{up}} \approx t_{\text{down}}$ and $t_{\text{RCAL}} \approx t_{\text{FCAL}}$, as depicted in figure 6.3 A. cosmic and halo muons enter the detector from outside, creating a different signature in these values, as depicted in figure 6.3 B and C.

The principle selection was satisfied if all of the following conditions were met:

1. $P_{T,\text{miss}} > 6$ GeV
2. $|z_{vtx}| < 60$ cm
3. Up-Down CAL time difference which was indicative of an interaction originating within the detector.

The third condition compares the timing information from the upper and lower half of the calorimeter. This condition rejected cosmic rays, which often come from above the ZEUS detector. The event was also accepted if all of the following conditions were met

1. $P_{T,\text{miss}} > 6$ GeV
2. $\left(E_{FCAL} > 10 \text{ GeV} \parallel N_{\text{gt}} > 0\right)$
3. No off-momentum protons were detected
4. No deposits characteristic of beam-gas interactons were observed

5. Proper numbers of tracks were observed

6. ($N_{CTDhits} < 2500 \| P_{T,\text{miss}} > 10$ GeV)

7. Up-Down CAL time difference which was indicative of an interaction originating within the detector.

The alternative trigger accepted the event if $P_{T,\text{miss}} > 8$ GeV, and either $E_T(-IR) > 8$ GeV, one jet found with the cone algorithm [61] such that $E_T^{\text{jet}} > 8$ GeV, or one k_T jet was found such that $E_T^{\text{jet}} > 8$ GeV. This is the only condition in this thesis where cone jets were considered. At all other points, a jet refers explicitly to jets found using the k_T cluster algorithm.

When an event satisfied the trigger selection criteria, it was written to data tape for storage and alter analysis. We now turn to the Offline selection, in which events were selected to fill histograms that would later become distributions and cross sections.

6.3 Offline Event Selection

The selection criteria applied to events after triggering can be separated into three categores: Preselection, in which loose cuts are applied to speed analysis, Cleaning Selections, in which background and poorly reconstructed events are rejected, and Phase space selection, in which events are selected with desired kinematic and jet properties.

6.3.1 Preselection

The performance of the ZEUS detector, luminosity monitoring systems and polarization monitoring systems varied during data taking. The ZEUS reconstruction library contains a dedicated functions which indicated wether the ZEUs detector subcomponents were in proper functioning order at the time the event was recorded, and events taken with all central components properly functioning were only used in this analysis. MC events were not subject to these selections.

The two methods of polarization measurement, LPOL and TPOL, produced comparable but different measurements of the average polarization during each data taking run. If the integrated luminosity for a given run measured by the LPOL was greater than or equal to that that of the TPOL, then data events were only selected if the LPOL was indicated as functioning properly. If $L_{\mathrm{TPOL}} > L_{\mathrm{LPOL}}$ during the run, then events were only taken if the TPOL was functioning properly. MC events were not subject to this selection. The average polarization value and integrated luminosity for each data run was exclusively taken from the LPOL if $L_{\mathrm{LPOL}} < L_{\mathrm{TPOL}}$, otherwise values from the TPOL were used.

Events were required to have $P_{T,\mathrm{miss}} > 9$ GeV, $P_{T,\mathrm{miss}}/E_T > 0.3$, and at least one calorimeter jet within $-1 < \eta^{\mathrm{jet}} < 2.5$ and $E_T^{\mathrm{jet}} > 3$ GeV, where E_T^{jet} was computed purely from CAL cell energies. These cuts are less restrictive forms of cuts which were applied later, and are described in section 6.3.3 in detail. Events meeting all these criteria were then retrieved from the ZARAH computing farm and stored on a local workstation for analysis.

6.3.2 Signal Selection and Background Rejection

This section describes selection cuts which were applied both to select signal and reject background, which are in many cases insuperable actions. The principle signal of CC DIS is missing transverse momenta, due to the neutrino which escapes detection. Many other types of *ep* and non-*ep* events create this signature in the detector, such as CAL PMT sparks, cosmic or halo muons, and particles which escape down the beam pipe at a low angle. Thus, many other selection cuts are required to remove events from these sources.

All detector level events were required to have a $p_T^{\mathrm{CAL}} > 11$ GeV as measured by the CAL without any corrections applied. This both selected CC DIS events, and ensured trigger efficiency, because many trigger conditions were set to a $P_{T,\mathrm{miss}}$ much lower.

In order to reconstruct events properly, as well as reject events not originating from *ep* interactions, a properly reconstructed vertex was required. Before this could be performed, good tracking conditions on which the vertex reconstruction relied were required. Because the phase space of jets found in the analysis aimed at reaching to $\eta^{\mathrm{jet}} \equiv 2.5$, while the CTD accpetance begins to deteriorate at $\eta \equiv 2$, special tracking requirements were formed to differentiate these two cases.

As described in section 6.3.1, all events were required to have a jet before being retrieved from tape. Events where the jet with highest highest E_T^{jet} satisfied $\eta^{\mathrm{jet}} > 2$ are referred to as *forward-jet events*. forward-jet events events have many tracks outside the CTD acceptance, and are treated specially.

Non-forward-jet events were expected to have many tracks within the CTD,

and geometric information in the CTD and CAL were expected to agree. Selection requirements for non-forward-jet events were

1. $N_{\rm gt} \geq 1$, where $N_{\rm gt}$ is the number of *good tracks*[1] in the CTD. These tracks were reconstructed with high purity, which enabled the reliable reconstruction of the event vertex.

2. $|\phi^{\rm CTD} - \phi^{\rm CAL}| < 1$ rad, where $\phi^{\rm CTD}$ is the azimuthal angle of the net momentum from tracks in the CTD and $\phi^{\rm CAL}$ is the azimuthal angle of the net momentum from cells in the CAL. This selection cut removed events where a cosmic or halo muon deposited energy in the CAL during an *ep* event.

3. $p_T^{\rm CTD} > 0.1 \times p_T^{\rm CAL}$ or $p_T^{\rm CAL} > 25$ GeV. This selection cut removed events where a cosmic or halo muon deposited energy in the CAL during an *ep* event.

Forward-jet events were exempt from these requirements, but the transverse momentum requirement for these events was tightened for these events to $p_T^{\rm CAL} > 20$ GeV.

Events were required to have a reconstructed vertex with $-35 < z_{\rm vtx} < 33$ cm. This removed many events which were triggered from beam gas and halo muons.

As described in section 2.1.4, PHP events may have a large reconstructed $P_{T,\rm miss}$, and no isolated electron in the CAL. These events were largely removed by requiring $P_{T,\rm miss}/E_T > 0.5$.

Some NC DIS events occurred in overlap with a CAL PMT spark. This cell would then carry a significant fraction of the E_T of the event. Requiring $E_T^{\rm max}/E_T < 0.7$

[1]Good tracks in the offline selection were defined as tracks which possessed a transverse momentum such that $0.15 \leq p_T^{\rm trk} \leq 150$ GeV, a polarangle such that $15 \leq \theta_{\rm trk} \leq 164^\circ$, and were fit with at least 10 degrees of freedom.

removed these events, where $E_T^{\max}$ is the E_T of the CAL cell with the largest E_T.

Some NC DIS events occurred in overlap with a halo or cosmic muon. These events left a large amount of energy in the BHAC, E_{BHAC}, relative to other parts of the CAL. Energies in the first and second hadronic parts of the BHAC are labled as E_{BHAC1} and E_{BHAC2}, respectively. These events were removed by rejecting events if either of the following were satisfied:

- $E_{\mathrm{BCAL}} > 8$ GeV and $E_{\mathrm{BHAC1}}/E_{\mathrm{BCAL}} > 0.85$
- $E_{\mathrm{BCAL}} > 2$ GeV and $E_{\mathrm{BHAC2}}/E_{\mathrm{BCAL}} > 0.5$

Some cosmic muons traversed the ZEUS detector with a very small distance of closest approach to the nominal interaction point. These types of events appear as two hadronic jets with two nearly anti-parallel tracks. These events were removed by rejecting all events with only two "good" tracks, such that the cosine of their angle was less than -0.996.

Some NC DIS events were reconstructed with large $P_{T,\mathrm{miss}}$. The were removed from the sample by identifying an isolated electron in the CAL. As described in section 4.3, candidate electrons were identified by the SINISTRAprogram. Only the highest probability candidate was considered. Variables characterizing candidate included

- E'_e, the sum energy of CAL cells associated with the candidate.
- θ_e, the polar angle of the candidate cluster
- $\mathcal{I}_e$, the *isolation* of the electron from other CAL deposits; computed as $\mathcal{I}_e = \overline{E'}_{e,7}/E'_e$, where $\overline{E'}_{e,7}$ is the energy sum of the cells belonging to the candidate

which are outside a cone of radius .7 from the center of the candidate deposit in the $\eta - \phi$ plane.

- $\mathcal{N}_e$, the *narrowness* of the electron from other CAL deposits; computed as $\mathcal{I}_e = E'_{e,3}/E'_e$, where $E'_{e,3}$ is the energy sum of the cells belonging to the candidate within a cone of radius .3 in the $\eta - \phi$ plane.

Events were rejected if the following conditions were all satisfied.

1. $E'_e \geq 10$ GeV
2. $20 \leq \theta_e \leq 140$
3. $\mathcal{I}_e \leq .1$
4. $\mathcal{N}_e \geq .9$

Events were also rejected if the electron candidate satisfied ($y_{\text{footnotesize e}} < 0.7$), where y_{e} is the inelasticity of the event computed from the electron candidate information as $y_{\text{e}} = 1 - \frac{E'_e}{2E_e}(1 - \cos(\theta_e))$, where E_e is the nominal HERA II electron beam energy of 27.5 GeV..

Electrons form NC DIS occasionally deposited their energy in a wide shower, which could be falsely reconstructed as a jet. Events were rejected if any jet in the event overlapped with the electron candidate. Specifically events were rejected if all the following were satisfied:

- $E'_e > 10$ GeV
- The distance in the $\eta - \phi$ plane between the jet and electron candidate was less than 0.1

- $|1 - E'_e/E_{\rm jet}| < 0.2$

Here, $E_{\rm jet}$ refers to the uncorrected CAL cell energy of the jet in question.

Even after these cleaning cuts, approximately 1% of the event was comprised by halo and cosmic muon events. These have a topology which is simple to identify by sight, but difficult to reliably quantify. The sample was independently visually scanned by two anilyzers, and the remaining events were removed from the sample. No MC events were removed in this manner.

6.3.3 Kinematic and Jet Selection

All Detector level events were required to have a dead-material-corrected Q^2 value greater than 200 GeV, and a corrected y less than 0.9.

All jet variables will henceforth refer solely to those corrected for detector effects unless otherwise stated. Clustered objects were only considered jets if they satisfied $-1 < \eta^{\rm jet} < 2.5$. Thus, the terms *jet with highest* E_T^{jet}, *most forward jet* etc. implicitly refer to jets selected exclusively from the set of all jets within this $\eta^{\rm jet}$ range. All data events events in the sample were required to have the jet with highest $E_T^{\rm jet}$ satisfy $E_T^{\rm jet} > 14$ GeV. Inclusive jets were defined as any jet with $E_T^{\rm jet} > 14$ GeV. Dijet systems were defined as the two jets in an event with highest $E_T^{\rm jet}$, such that they possessed $E_T^{\rm jet1} > 14$ GeV and $E_T^{\rm jet2} > 5$ GeV, where $E_T^{\rm jet1} \geq E_T^{\rm jet2}$. 3-jet systems were defined as the three jets in an event with highest $E_T^{\rm jet}$, such that $E_T^{\rm jet1} > 14$ GeV, $E_T^{\rm jet2} > 5$ GeV and $E_T^{\rm jet3} > 5$ GeV, where $E_T^{\rm jet1} \geq E_T^{\rm jet2} \geq E_T^{\rm jet3}$.

6.4 Reconstruction and Selection of Simulated Events

To produce detector level and corrected detector level distributions for MC events, all selection criteria were performed identically as for the data, with exceptions noted in section 6.3.2 and 6.3.3.

Parton- and hadron-level simulated events were only selected if $Q^2_{\text{gen}} > 200$ GeV and $y_{\text{gen}} < 0.9$, where Q^2_{gen}, y_{gen} are understood to be the generated values, not the values from the QED born level.

Parton- and hadron-level jets were found in the lab frame by applying the k_T cluster algorithm to partons and hadrons, as described in chapter 4.5. Hadronic (partonic) jets were selected with the same phase space requirements as the corrected detector level jets, as described in section 6.3.3.

Chapter 7

Analysis Method

7.1 Comparison to MC and Data

In order to measure the cross sections independent of the specific characteristics of the detector, the data were corrected to the hadron level using leading-order MC. Before this was done, it was ensured that the detector-level quantities matched well between the two. The agreement was examined both within the phase space used for the analysis, and in the nearby regions.

7.1.1 Reweighting Procedure

The generated distributions of $z_{\rm vtx}$ and Q^2 are predetermined input parameters to the MCs, and were chosen to represent the data. In order to improve the agreement between data and MC, MC histograms were filled with weights differing slightly from 1. MC events were assigned weights given by $w = w_z \times w_{Q^2} \times w_{track}$ for all detector-level quantities, and $w = w_z \times w_{Q^2}$ for all hadron- and parton-level quantities. The terms, w_z and w_{Q^2} refer to independant weights for the generated values of z_{vtx} and Q^2 respectivley. The variable w_{track} refers to a weight which accounts for a tracking

veto which was not included in the MC detector description at the time of generation. These factors are described in detail in Appendix B.

7.1.2 Detector-level Comparisons

In figures 7.1, the comparison between data and ARIADNE is shown for $e^{-}p$ inclusive jet samples. Equivalent comparisons for $e^{-}p$ are included in appendix A. It can be observed that all presented quantities shown are in good agreement, both inside and outside of the selection criteria. In figures 7.2, detector-level jet quantites are shown. Here it can be observed that data events have significantly more jets than the MC, which is expected because higher order terms are responsible for jet production. The distributions of E_T^{jet} and η^{jet} for jets with highest, second- and third-highest E_T^{jet} are all in good agreement, however, so it is still acceptable to use the MC to correct event and jet variables.

7.2 Correction Procedures Applied to Data Events

7.2.1 Inactive Material Corrections

As particles left the interaction region, they passed through the MVD, HERA beampipe, and suppourt materials before entering the active region of the CTD. particles then passed thought the solenoid and more support structures vefore before reaching the CAL. This means that particles would trasfer some of their energy before being measured, and their reconstructed quantities of the interaction do not exactly reflect the state shortly after the *ep* interaction.

In order to understand these effects, and to correct the reconstructed values of

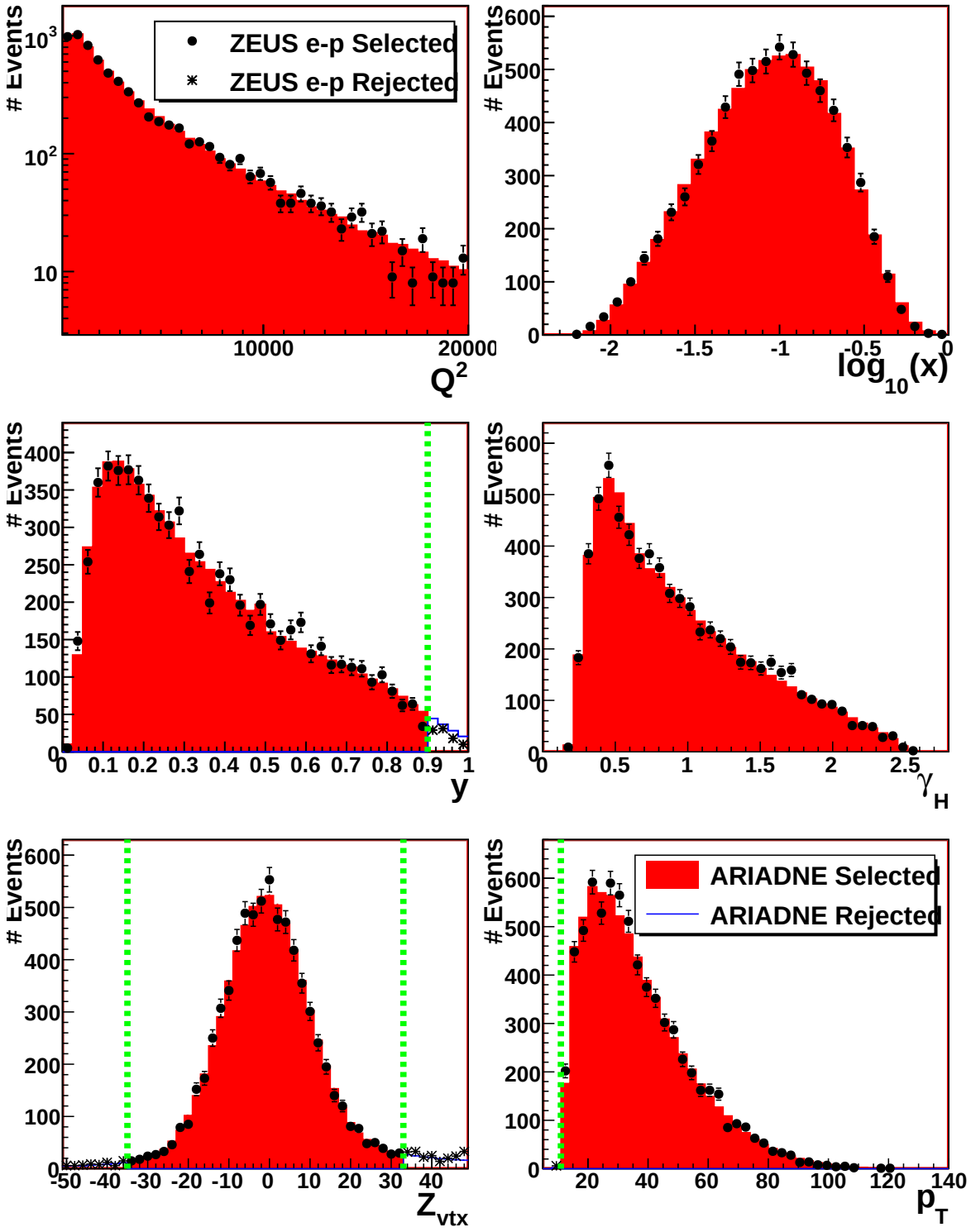

Figure 7.1: Comparison between detector level kinematic quantities of e^-p data and ARIADNE. Filled histograms and closed points represent data and MC events which were selected for the inclusive-jet sample. Stars and empty histograms represent data and MC events which fall outside the kinematic selection, but were only rejected by the selection cut indicated by the dashed line. The selection cut on $Q^2 > 200$ is applied, but not shown. The MC has been area-normalized to the data for each plot shown.

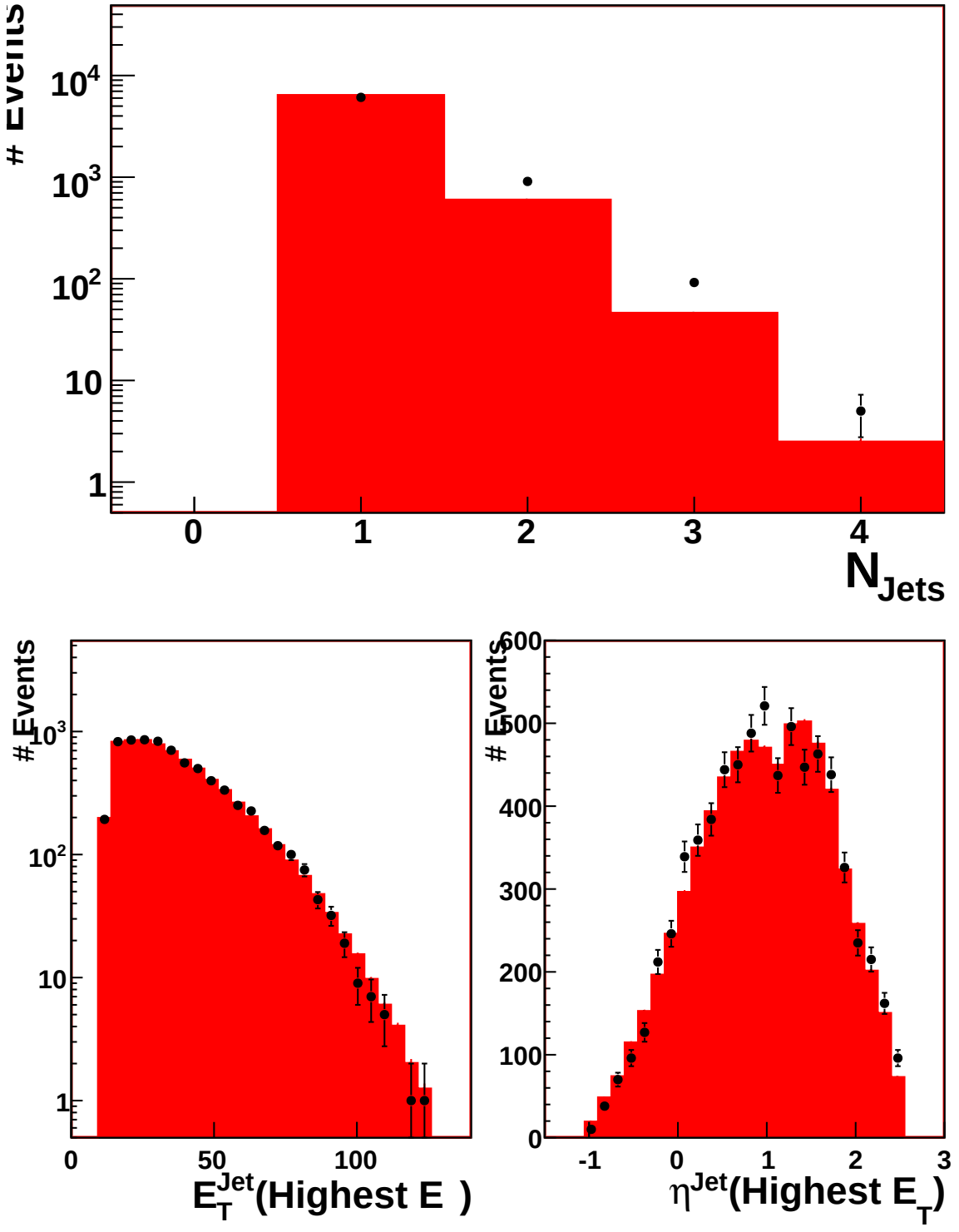

Figure 7.2: Comparison between detector level jet quantities of e^-p data and ARIADNE. All events shown appear with all inclusive-jet selection cuts applied, but no correction to jet variables has been applied. Within these plots, a jet is defined as any k_T cluster object with $E_T^{\rm jet}$ greater than 5 GeV and $-1 < \eta^{\rm jet} < 2.5$.

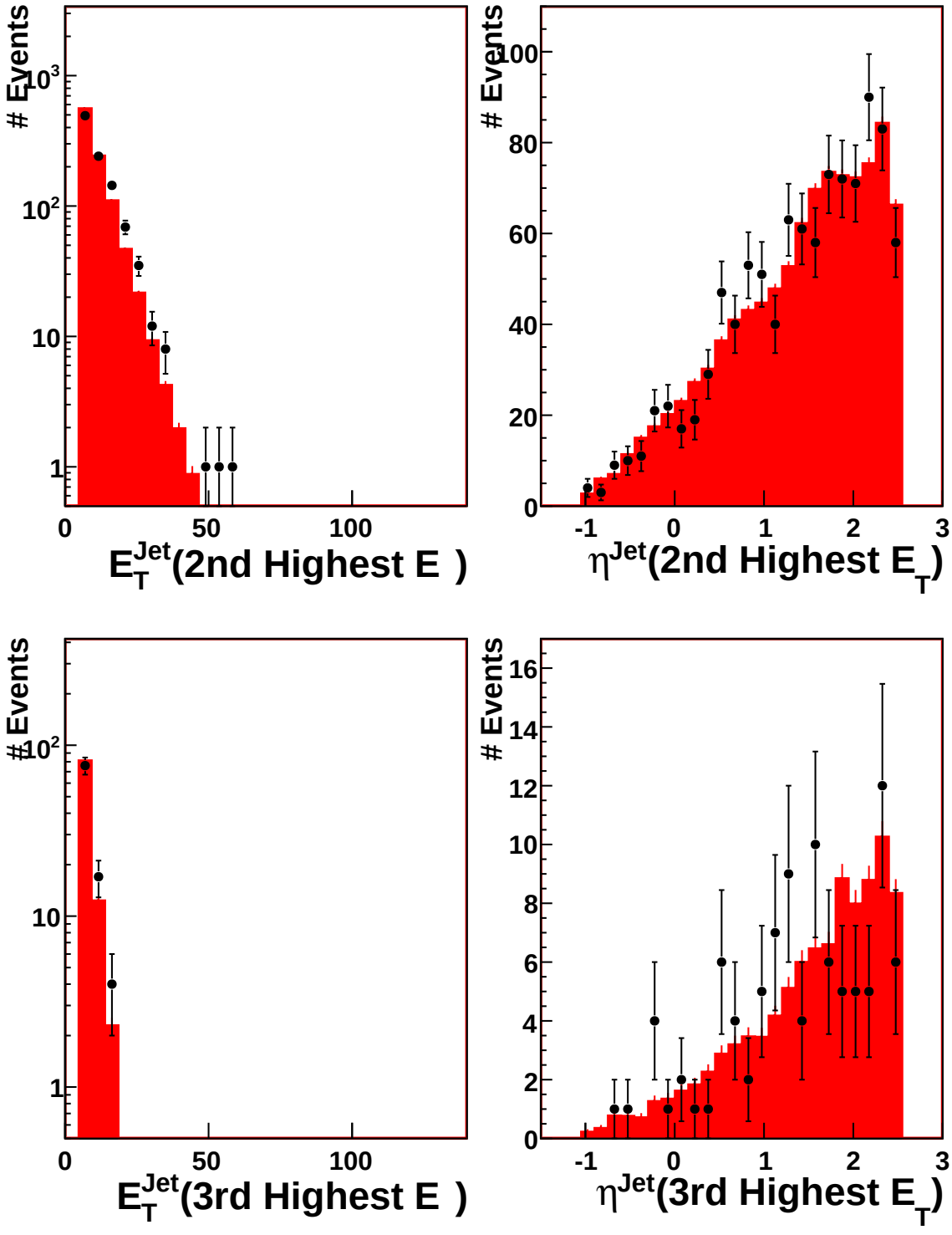

Figure 7.3: Comparison between detector level jet quantities of e^-p data and ARIADNE. All details as in figure 7.2.

energy, transverse momentum, and kinematic quantities, samples of MC were used to estimate these effects in different regions of the detector. By comparing values for each event produced at the hadron- and detector-level, estimations of energy loss or bias were performed, and correction factors were computed.

These correction factors were then appllied to data events, and MC events at the detector level, to produce values which are referred to here as at the corrected-detector level, or detector values corrected for dead material. These values were thne used for detector-level distributions, which in turn were used to produce the presented cross sections. Correction factors were first applied to $P_{T,\text{miss}}$ and y, and then these values were used as described in equation 4.5. A detailed explanation of the functions used is presented in appendix G.

In figures 7.4 and 7.5, the bias and resolution of $P_{T,\text{miss}}$ and y, respectively, are presented. MC samples presented here are from $e^{-}p$ ARIADNE samples described in section 5, and complimentary but eqivalent plots for other MC samples are shown in appendix G. The central line indicates the mean reconstructed values for each variable, before and after corrections were applied. Error bands indicate the 1-σ limits as taken from gaussian fits along the vertical axis.

From figure 7.4, it can be observed that $P_{T,\text{miss}}$ was reconstructed before corrections approximately 10% below its hadron-level value, for $P_{T,\text{miss}} > 20$ GeV. For $P_{T,\text{miss}} < 20$ GeV, the reconstructed bias in $P_{T,\text{miss}}$ decreases. After corrections,$P_{T,\text{miss}}$ was reconstructed within a few percent for $P_{T,\text{miss}} > 20$, but is biased above the hadron-level value below. The principle $P_{T,\text{miss}} > 11$ GeV cut was not applied during the production of this histogram, but the supplimentary $P_{T,\text{miss}} > 20$ GeV cleaning cut

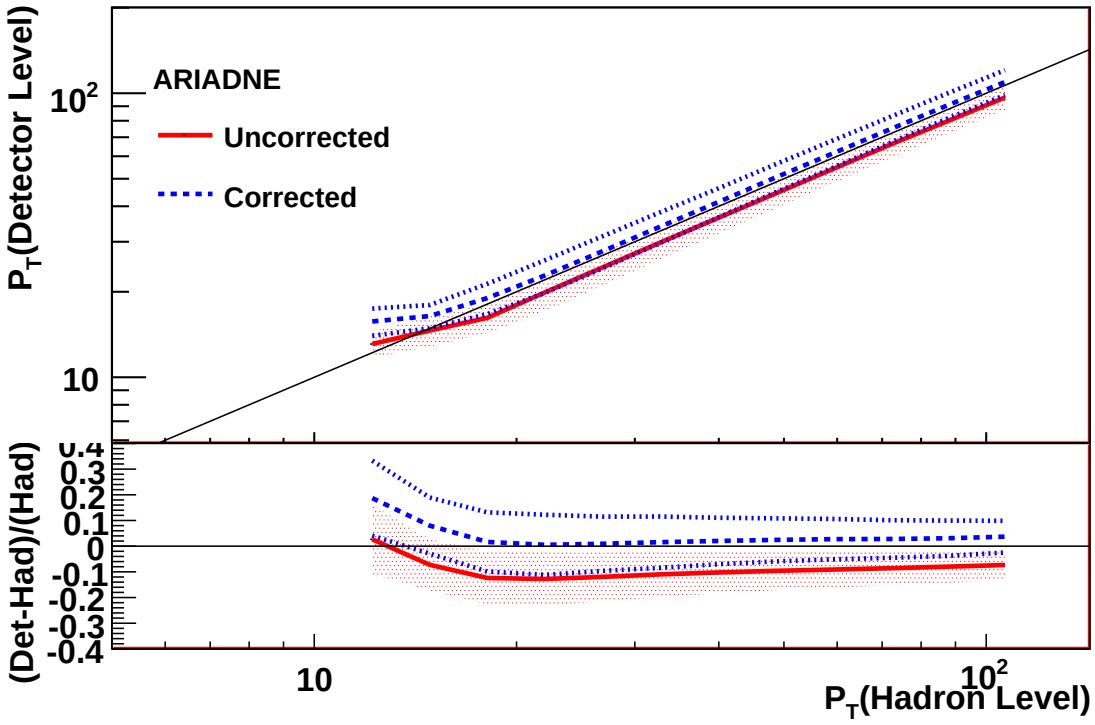

Figure 7.4: *Comparison between hadron- and detector-level $P_{T,miss}$ for e^-p ARIADNE*

for forward-jet events was retained.

From figure 7.5, it can be observed that y was reconstructed with a roughly linear bias, decreasing with increasing y. It can also be seen that the resolution of y deteriorates with increasing y. After reconstruction, no systematic shift in y can be observed below y of .9, which is the boundary of the chosen phase space.No y cut was applied during the production of this histogram.

Figure 7.6 shows that the reconstructed values of Q^2 were systematically below their hadron-level values by approximately 20% before corrections were applied. From 200 GeV^2, to 300 GeV^2, this effect was less. After corrections, the reconstructed Q^2 is much closer to the generated value, and exhibits an increasing bias with increasing Q^2. No Q^2 cut was applied during the production of this histogram.

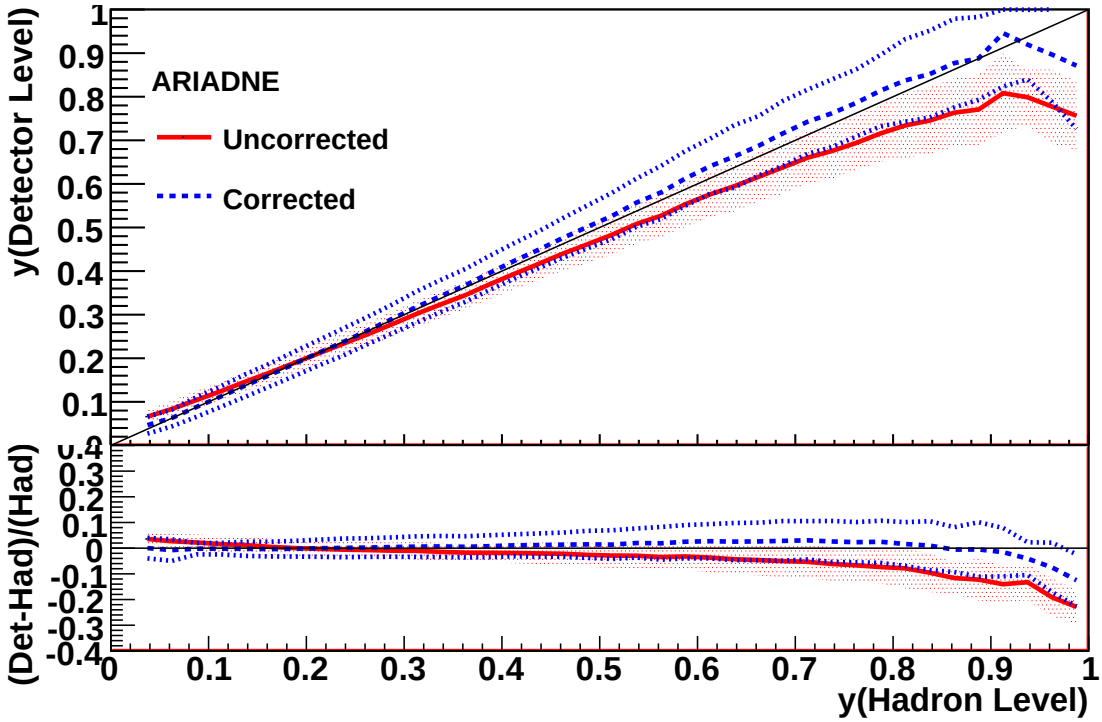

Figure 7.5: *Comparison between hadron- and detector-level y for e^-p ARIADNE*

Figure 7.7 shows the trend of reconstructed values of x, before and after corrections. It can be observed that before corrections, the reconstructed value was below the hadron-level value by nearly 20% over the range (0.01, 0.2). After corrections, the reconstructed values were typically within a few percent of their generated values.

7.2.2 Jet Energy Corrections

Figure 7.8 shows the tendencies of reconstructed E_T^{jet} values for all jets with $E_T^{\text{jet}} > 3$ GeV, within the η^{jet} range $-1.5 < \eta^{\text{jet}} < 2.5$. No other jet cuts were applied. It can be seen from the figure that the average reconstructed value for E_T^{jet} is below the hadron-level value over the entire range of accessable values,and that the resolution suffers a notable decrease below approximately 15 GeV. After corrections, the resolution remains unchanged, but the average value of reconstructed E_T^{jet} is much

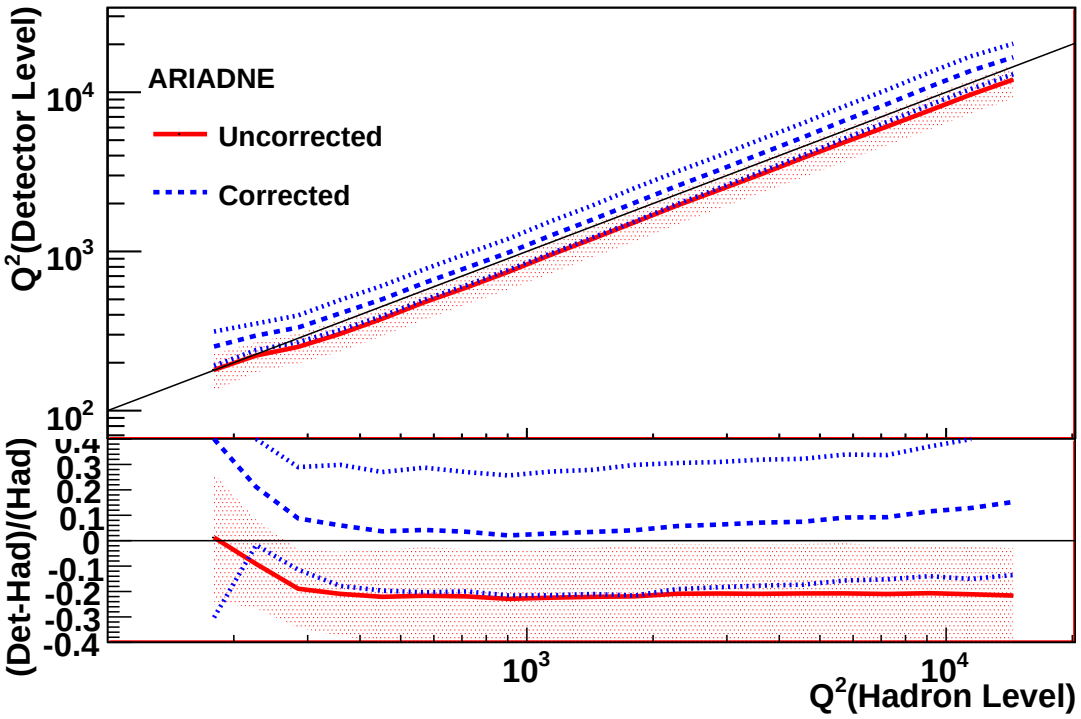

Figure 7.6: *Comparison between hadron- and detector-level Q^2 for e^-p ARIADNE*

closer to the hadron-level value. The resolution for hadron-level jets is approximately 20% in the range $5 < E_T^{\text{jet}} < 15\ GeV$, and approximately 10% for $E_T^{\text{jet}} > 15$ GeV. Figure 7.9 shows the tendencies of reconstructed η^{jet} values for all jets with $E_T^{\text{jet}} > 3$ GeV. No other jet cuts were applied. It can be seen from the figure that the average reconstructed value for η^{jet} is in agreement with the hadron-level value over the entire range of accessable values, with the exception of jets with $\eta^{\text{jet}} > 2.5$. The resolution also suffers a notable decrease at high η^{jet}. No corrections were applied to η^{jet} values.

Figure 7.10 shows the tendencies of reconstructed ϕ^{jet} values for all jets with $E_T^{\text{jet}} > 3$ GeV, $-1.5 < \eta^{\text{jet}} < 2.5$. No other jet cuts were applied. It can be seen from the figure that the average reconstructed value for ϕ^{jet} is in agreement with the hadron-level value, within aone or two degrees, and that the resolution is on average

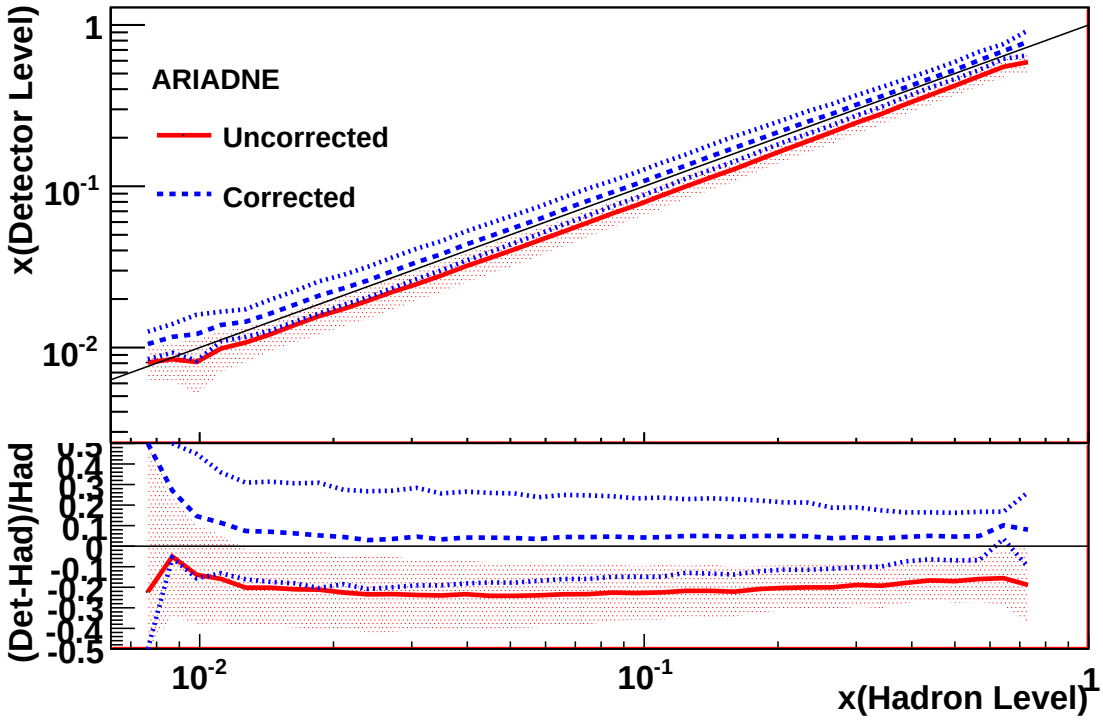

Figure 7.7: *Comparison between hadron- and detector-level x for e^-p ARIADNE*

within 5 degrees. No corrections were applied to $\eta^{\rm jet}$ values.

7.2.3 Transverse Energy Corrections

To understand the the uncertainty in the absolute energy scale of the jets, the differences between data and MC simulation in single-jet NC DIS events was studied [62]. Because the transverse energy of the single jets and electrons is expected to be equal in these events, the reconstructed transverse energy of the electron, $E_{T,\rm DA}$, provided an alternative meas of estimating the transverse energy of the jets. The ratio of $R =< E_T^{\rm jet}/E_{T,\rm DA} >$ was therefore expected to be near one. The double ratio $R_{\rm DATA}/R_{\rm MC} - 1$ vs. $\eta^{\rm jet}$ is presented in figure 7.11 before corrections factors were applied. In figure 7.11 the same ratio is plotted after correction factors were applied to the data, showing a far better agreement between data and MC. The same ratio as

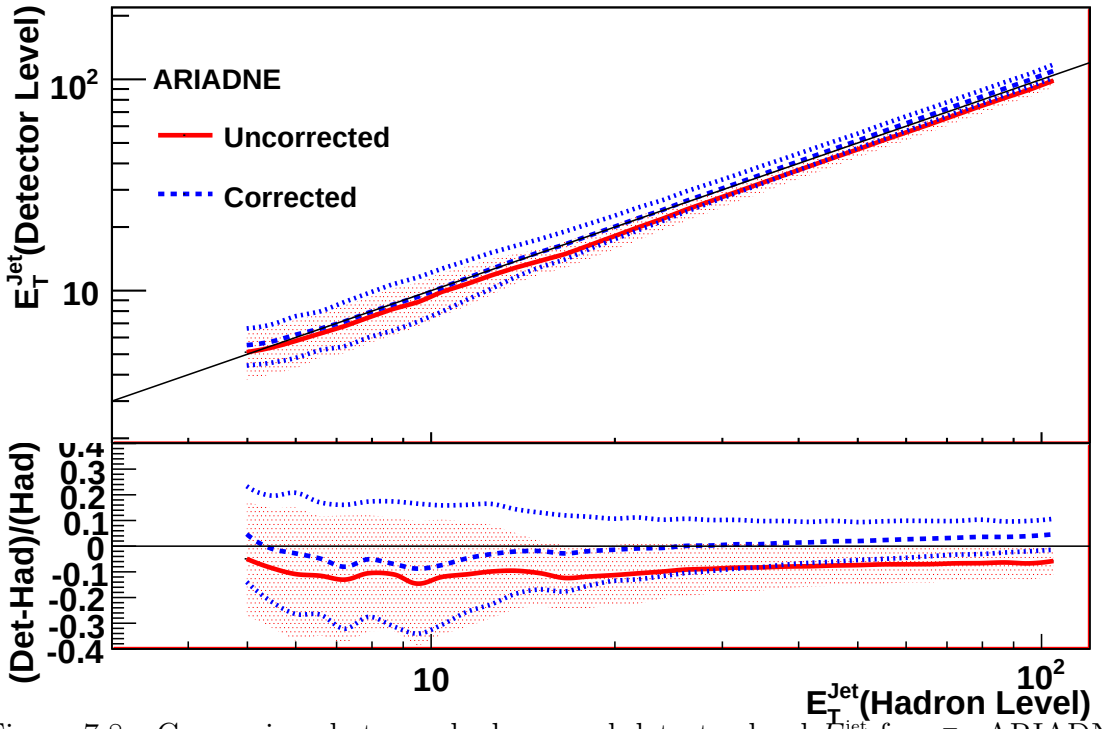

Figure 7.8: Comparison between hadron- and detector-level $E_T^{\rm jet}$ for e^-p ARIADNE.

a function of $\gamma_{\rm H}$ are presented in figures 7.12 and 7.12.

The same correction factors derived from $R_{\rm DATA}/R_{\rm MC}$ in the NC DIS sample were applied to data in the CC DIS samples presented here.

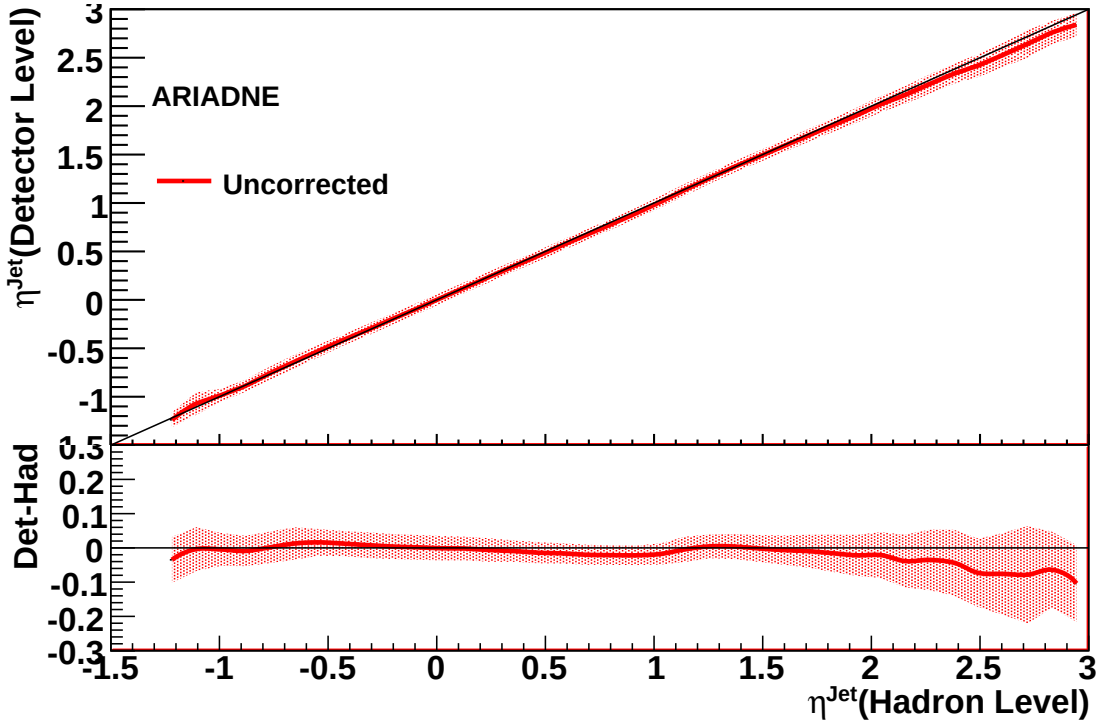

Figure 7.9: Comparison between hadron- and detector-level $\eta^{\rm jet}$ for e^-p ARIADNE.

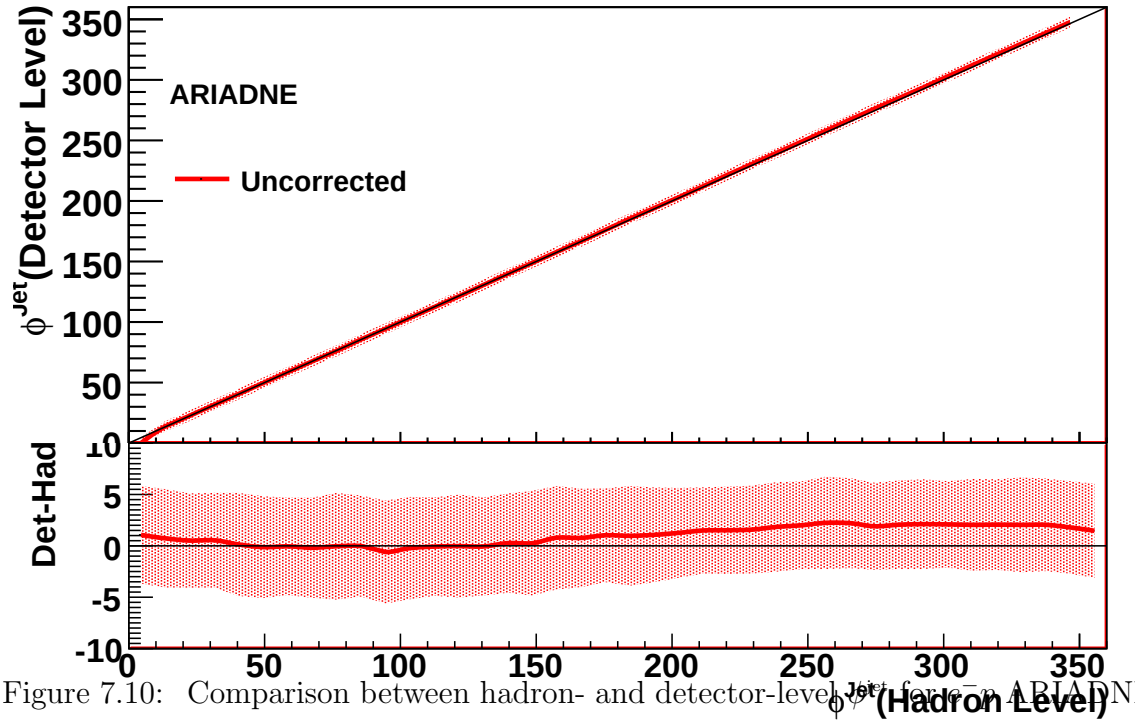

Figure 7.10: Comparison between hadron- and detector-level $\phi^{\rm jet}$ for e^-p ARIADNE.

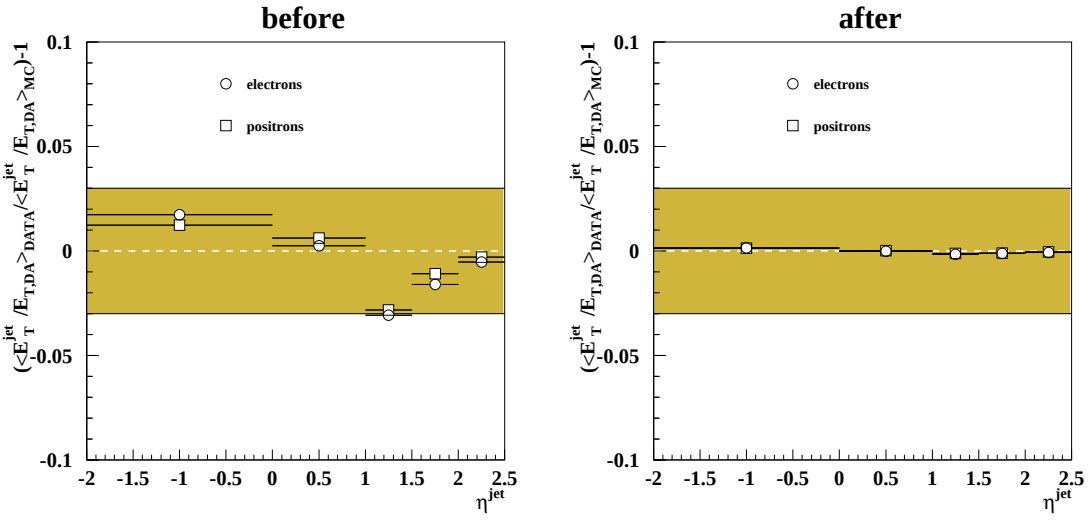

Figure 7.11: Jet transverse energy data-mc double ratios before and after corrections vs. $\eta^{\rm jet}$ for $e^- p$ ARIADNE.

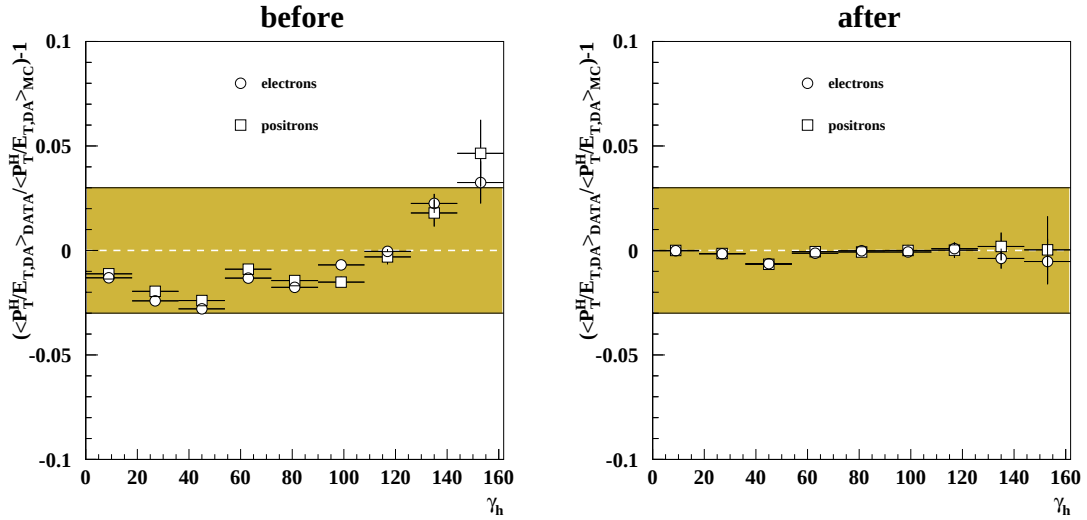

Figure 7.12: Jet transverse energy data-mc double ratios before and after corrections vs. $\gamma_{\rm H}$ for $e^- p$ ARIADNE.

7.3 Correction Procedures Applied to Theoretical Calculations

7.3.1 QED Corrections

Because the MEPJETprogram does not include QED radiative effects, correction factors were applied to the born-level partonic distributions. These correction factors, denoted δ_{QED} in the tables, were generated using the program HERACLES, with and without QED radiating effects. The Fermi coupling constant $G_F = 1.1664 \cdot 10^{-5}$ GeV^{-2} and the mass of the Z boson $M_Z = 91.1876$ GeV to determine the electroweak parameters.

7.3.2 Hadronization Corrections

In order to correct the partonic distributions from the fixed-order calculations to the hadron level, correction factors were applied individually to each bin of each histogram. These correction factors were derived from the ratios between hadronic and partonic distributions in the MC samples.

7.4 Estimation of Experimental Systematic Uncertainties

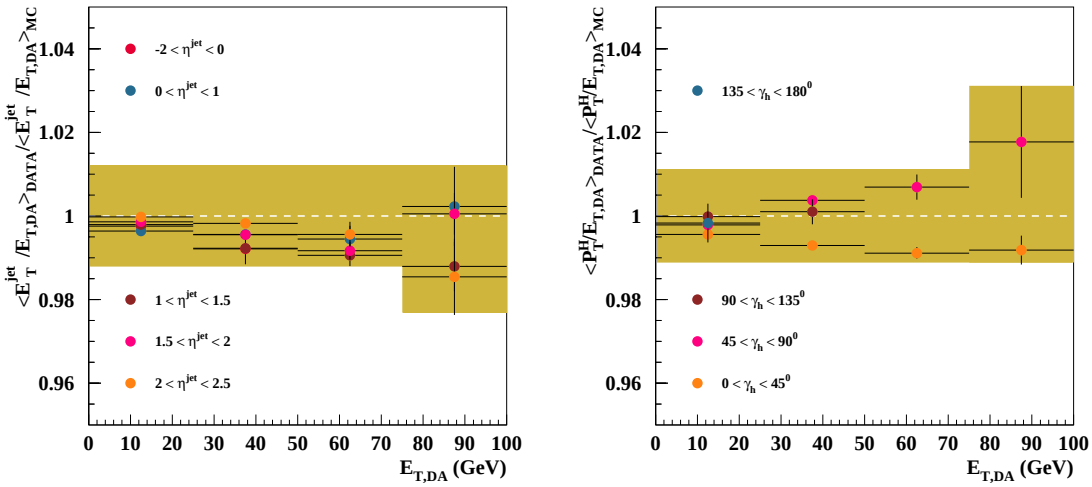

Figure 7.13: Jet Energy Scale Uncertainty vs. $\eta^{\rm jet}$ and $\gamma_{\rm H}$ for e^-p ARIADNE.

The same NC DIS data and MC samples described in section 7.2.3 were used to estimate the uncertainty of the energy scale of the jets. In figure 7.13, the double ratio $R_{\rm DATA}/R_{\rm MC}$ is presented, where individual points correspond to events with jets from specific bins of *rapjet*. The residual disagreement between data and MC in these regions give an estimate of the uncertainty in the reconstruction for jets in the CC sample. In figure 7.13, the same ratio is plotted, but with points representing events from specific bins of $\gamma_{\rm H}$.

7.5 Estimation of Theoretical Systematic Uncertainties

The uncertainty on the NLO QCD calculations due to terms beyond NLO, estimated by varying $\mu_{\rm R}$ between $Q/2$ and $2Q$, was typically below $\pm 2\%$ for the inclusive-jet cross sections and below $\pm 5\%$ for the dijet cross sections. For the LO calculations

of the three-jet cross sections the uncertainty was $\approx \pm 30\%$. For the three-jet cross sections, this uncertainty is dominant. Thus, no other theoretical uncertainty was taken into account for the three-jet cross sections.

The uncertainty on the NLO QCD calculations due to those on the proton PDFs was estimated by repeating the calculations using 22 additional sets from the ZEUS-S analysis, which takes into account the statistical and correlated systematic experimental uncertainties of each data set used in the determination of the proton PDFs. The resulting uncertainty in the inclusive-jet ep (e^+p) cross sections was below $\pm 2(4)\%$, except in the high-$E_T^{\rm jet}$, high-Q^2 and high-x regions where it reached $\pm 4(10)\%$. The resulting uncertainty in the dijet ep (e^+p) cross sections was below $\pm 5(5)\%$, except in the high-$E_T^{\rm jet}$, high-Q2 and high-x regions where it reached $\pm 7(15)\%$.

The uncertainty on the NLO QCD calculations due to that on $\alpha_{\rm S}(M_Z)$ was estimated by repeating the calculations using two additional sets of proton PDFs, for which different values of $\alpha_{\rm S}(M_Z)$ were assumed in the ts. The difference between the calculations using these various sets was scaled by a factor such as to reect the uncertainty on the current world average of $\alpha_{\rm S}(M_Z)$ [63]. The resulting uncertainty in the cross sections was below $\pm 1\%$.

The uncertainty from the modeling of the QCD cascade was estimated as the difference between the hadronization corrections obtained using the ARIADNE and LEPTO models. The resulting uncertainty on the inclusive-jet and dijet cross sections was typically below $\pm 1\%$.

The uncertainty of the calculations due to the value of $\mu_{\rm F}$ was estimated by repeating the calculations with $\mu_{\rm F} = Q/2$ and $2Q$. The effect was negligible.

Chapter 8

Results

8.1 Inclusive Jet Polarized Differential Cross Sections

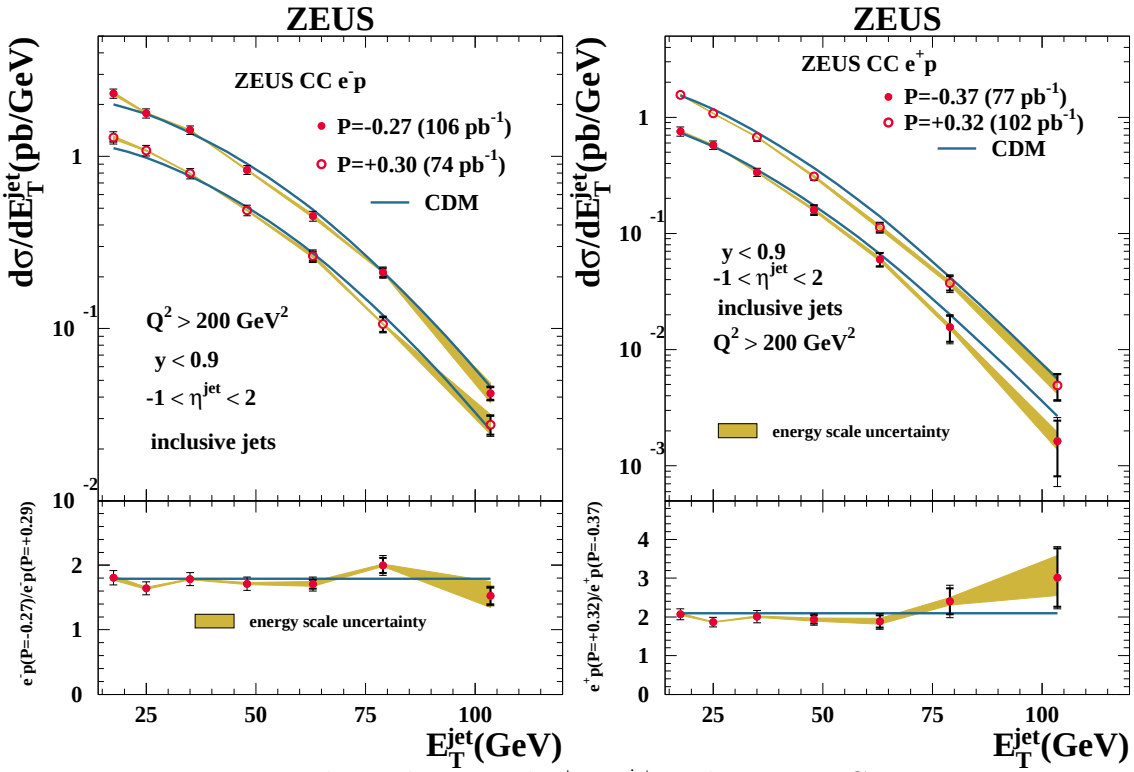

Figure 8.1: Polarized e^-p and e^+p $E_T^{\rm jet}$ Inclusive-Jet Cross sections

Differential inclusive-jet cross sections were measured in the kinematic regime $Q^2 > 200$ GeV^2 and $y < 0.9$. The cross sections were determined for jets with

$E_T^{\rm jet} > 14GeV$ and $1 < \eta^{\rm jet} < 2.5$.

The inclusive-jet differential cross sections as functions of $\eta^{\rm jet}$, $E_T^{\rm jet}$, Q^2 and x for negatively- and positively-polarized ep (e^+p) collisions are shown in Fig. 8.1a (8.1b) and Tables **??** to **??**. The predictions of the MEPJETcalculations are compared to the data in the figures. The lower parts of the figures show the ratio of the cross sections for negatively- and positively-polarized lepton beams, which is in agreement with the measured polarization ratio, $(1P_e^{neg})/(1P_e^{pos}) = 1.79 \pm 0.05$ for ep and $(1P_e^{neg})/(1P_e^{pos}) = 2.10 + 0.080.14$ for e^+p. The integrated polarized inclusive-jet cross sections, $\sigma - jets$, are shown in Table **??**. The measured cross sections are in good agreement with the predictions of the SM as given by the MEPJET calculations, also shown in Table **??**, in the kinematic range studied.

8.2 Inclusive Jet Unpolarized Differential Cross Sections

Figure 8.2-8.5 and Tables **??** to **??** show the unpolarized inclusive-jet differential cross sections as functions of $\eta^{\rm jet}$, $E_T^{\rm jet}$, Q^2 and x in CC $e^{\pm}p$ DIS.

The measured $\frac{d\sigma}{d\eta^{\rm jet}}$ has a maximum at $\eta^{\rm jet} \approx 1$. The measured $\frac{d\sigma}{dE_T^{\rm jet}}$ exhibits a fall-off of two (three) orders of magnitude in the ep (e^+p) sample. Values of $E_T^{\rm jet}$ of more than 100 GeV are accessible with the present statistics. For $200 < Q^2 < 2000$ GeV^2, the distributions display a weak dependence on Q^2. The cross sections as functions of $E_T^{\rm jet}$ and Q^2 show a less rapid fall-off than what is observed in NC DIS processes due to the presence of the massive W propagator. Furthermore, the measured cross sections for the e^+p sample decrease more rapidly as a function of $E_T^{\rm jet}$ and Q^2 than for the ep sample (see below).

The values in x accessible by the data are within the range $0.013 < x < 0.63$,

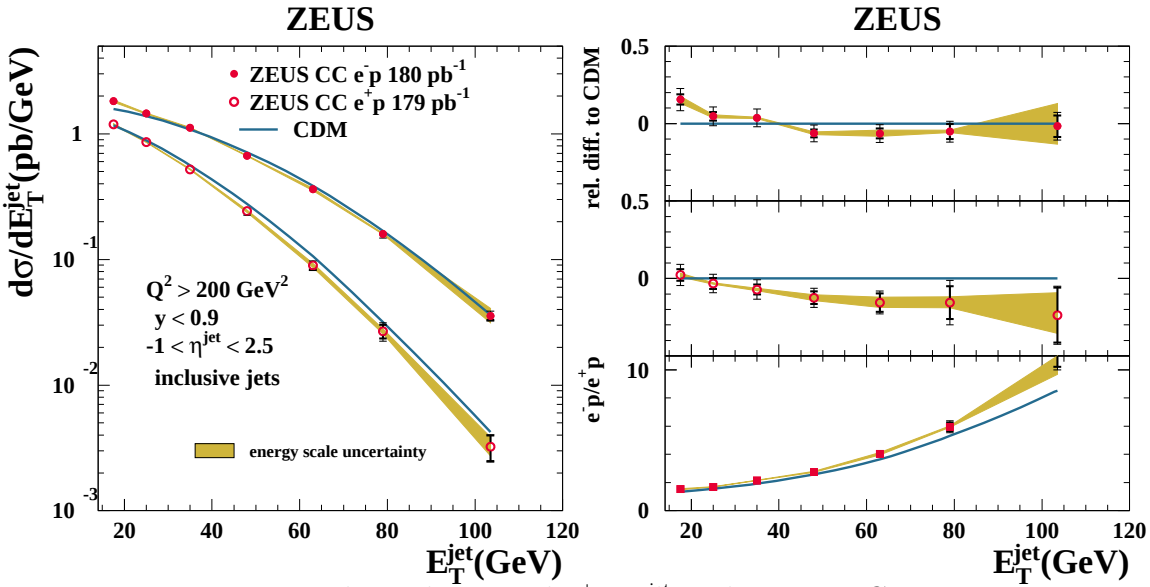

Figure 8.2: Unpolarized $e^- p$ and $e^+ p$ $E_T^{\rm jet}$ Inclusive-Jet Cross sections

as shown in Fig. 8.5a. The MEPJET predictions using the ZEUS-S PDF sets are compared to the data in **??**. Figure 8.5b shows the relative difference between the data and the predictions. The MEPJET predictions give a reasonable description of the shape and normalization of the data. Figure 8.2 also displays the ratio of the ep and e^+p differential cross sections. The measured ratio as a function of $\eta^{\rm jet}$ jet is constant and approximately 2 as predicted by QCD, since the two reactions probe a different parton content of the proton. The ratio as a function of $E_T^{\rm jet}$ (Q^2) increases as $E_T^{\rm jet}$ (Q^2) increases, in good agreement with the prediction. The increase at high values of $E_T^{\rm jet}$ and Q^2 is expected due to the increasing contribution from the valence-quark densities in the proton at high x and the fact that both reactions are sensitive to different quark flavors. The behavior observed in the ratio of the measured cross sections as a function of $Q^2$is similar to the ratio of u and d parton densities. The

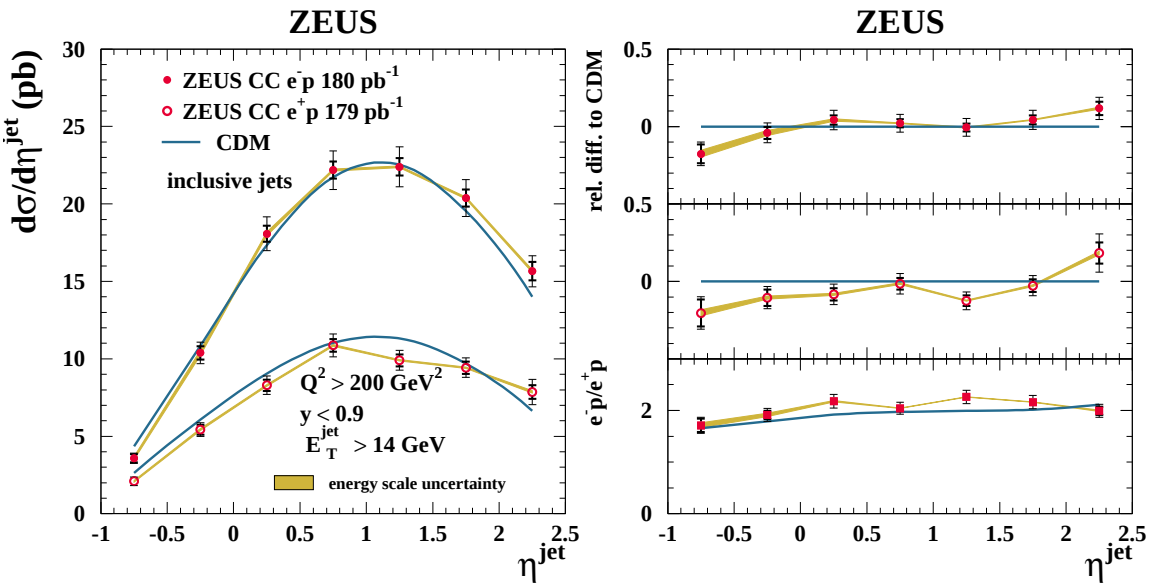

Figure 8.3: Unpolarized e^-p and e^+p $\eta^{\rm jet}$ Inclusive-Jet Cross sections

same behavior is observed as a function of x.

Figure **??** shows the contributions to the theoretical uncertainty from the terms beyond NLO, the parton-shower model and that coming from the uncertainty in the PDFs separately for e^-p and e^+p collisions. Also shown are calculations using other PDF sets. For inclusive-jet $e^{\pm}p$ CC cross sections, the uncertainty coming from that on the PDFs is dominant. At high $E_T^{\rm jet}$,$Q^2$and x, the uncertainty in the predicted cross sections for positron beams is larger than those for electron beams. This difference in the uncertainty due to the PDFs in the calculations for e and e^+ beams can be attributed to the different flavor content probed: in e^-p (e^+p) at high x the W (W^+) will couple predominantly to the u (d) valence quark in the proton; at present, the uncertainty in the d parton density is larger than that for the u quark. Furthermore, the comparison with the calculations using other PDF sets shows a wide spread in the

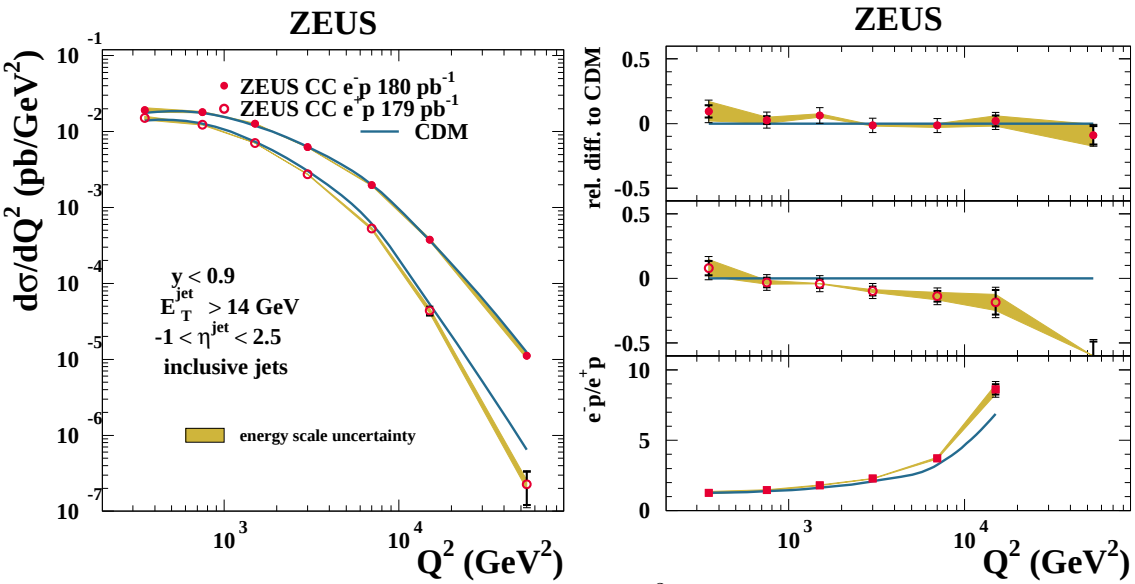

Figure 8.4: Unpolarized $e^{-}p$ and $e^{+}p$ Q^2 Inclusive-Jet Cross sections

predictions, especially for positron beams.

Therefore, these measurements, in a phase-space region where the other theoretical un- certainties are well under control, have the potential to constrain the flavor content of the proton if used together with other data in global fits. A fast and accurate method to perform fits to extract the proton PDFs on data sets that included jet cross sections in NC DIS and photoproduction was recently developed by the ZEUS Collaboration [50]; the result was a sizable reduction of the uncertainty on the gluon density at medium and high x. Using the data presented here and extending such a method to jet cross sections in CC DIS may help to constrain the u and d valence quark distributions at high x. The integrated unpolarized inclusive-jet cross sections, $\sigma-$jets , are shown in Table **??**. The measured cross sections are in good agreement

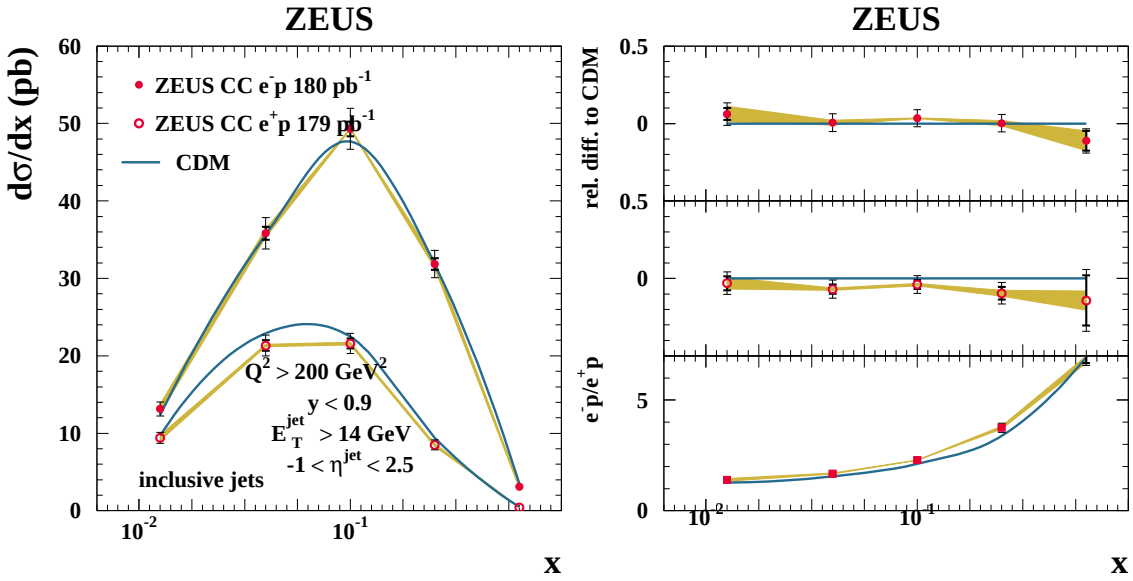

Figure 8.5: Unpolarized e^-p and e^+p x Inclusive-Jet Cross sections

with the MEPJET predictions, also shown in the table using different PDF sets.

8.3 Dijet Unpolarized Differential Cross Sections

Unpolarized dijet differential cross sections were measured in the kinematic regime $Q^2 > 200$ GeV^2 and $y < 0.9$. The cross sections were determined for jets with $E_T^{\rm jet1} > 14$ GeV, $E_T^{\rm jet2} > 5$ GeV and $1 < \eta^{\rm jet} < 2.5$. Figure **??** and Tables **??** to **??**, **??** and **??** show the unpolarized dijet differential cross sections as functions of $\overline{\eta}^{\rm jet}$, $\overline{E_T}^{\rm jet}$, Q^2 and the dijet invariant mass, $m^{\rm dijet}$, where $\overline{\eta}^{\rm jet} = (\eta^{\rm jet1} + \eta^{\rm jet2})/2$ and $\overline{E_T}^{\rm jet} = (E_T^{\rm jet1} + E_T^{\rm jet2})/2$ in CC $e^{\pm}p$ DIS. The measured jet cross section has a maximum at $\overline{\eta}^{\rm jet} \approx 1.25$. The measured cross section as a function of $\overline{E_T}^{\rm jet}$ exhibits a fall-off of two orders of magnitude for $\overline{E_T}^{\rm jet} \gtrsim 20$ GeV. For $200 < Q^2 < 2000$ GeV^2, the distribution displays a weak dependence on Q^2 . Values of $m^{\rm dijet}$ above 100 GeV

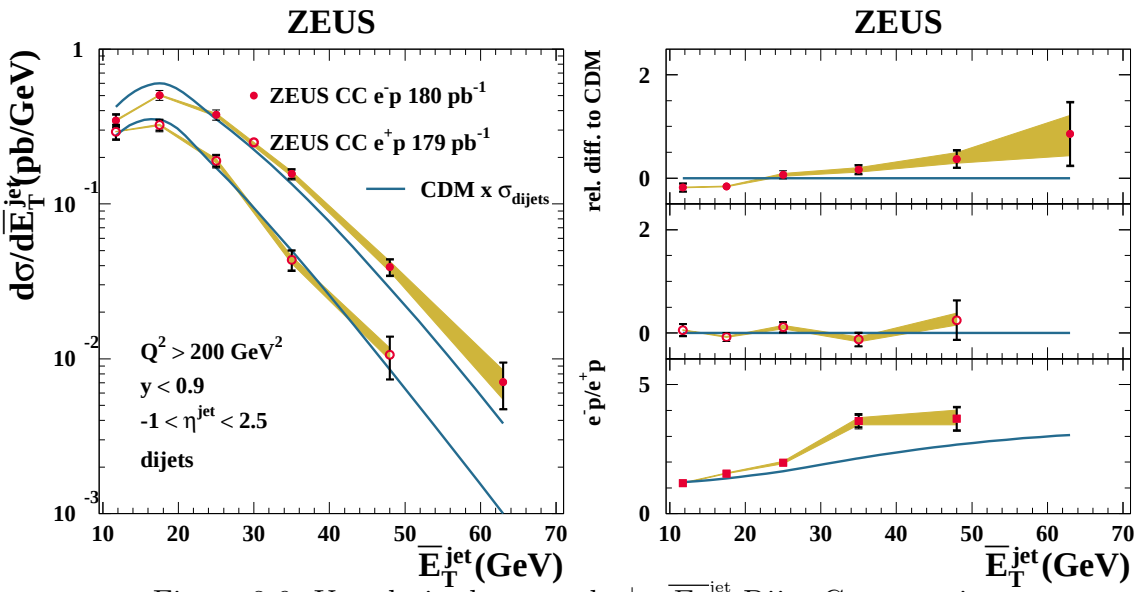

Figure 8.6: Unpolarized $e^- p$ and $e^+ p$ $\overline{E_T}^{\text{jet}}$ Dijet Cross sections

are accessible with the present statistics. The MEPJET predictions are compared to the data in Fig. **??**. Figure **??** shows the relative difference to the predictions. The MEPJET predictions do not give an adequate description in shape and normalization of the measured differential cross sections over the entire phase space considered. In particular, for m^{dijet} , the data tend to be above the predictions for $m^{\text{dijet}} \gtrsim 70$ GeV. As discussed in section 2.4.7, calculations of jet cross sections in NC DIS computed using the MEPJET program differ by 5 8% from the results from other NLO programs. Comparisons of inclusive-jet calculations for NC DIS in the kinematic range of the measurements presented here performed using MEPJET and Disent [??] showed an agreement better than 1%. However, similar comparisons for dijet cross sections showed relative differences above $\approx 5\%$. For CC DIS, it is not possible to quantify the degree of accuracy of the calculations of MEPJET since no alternative program exists.

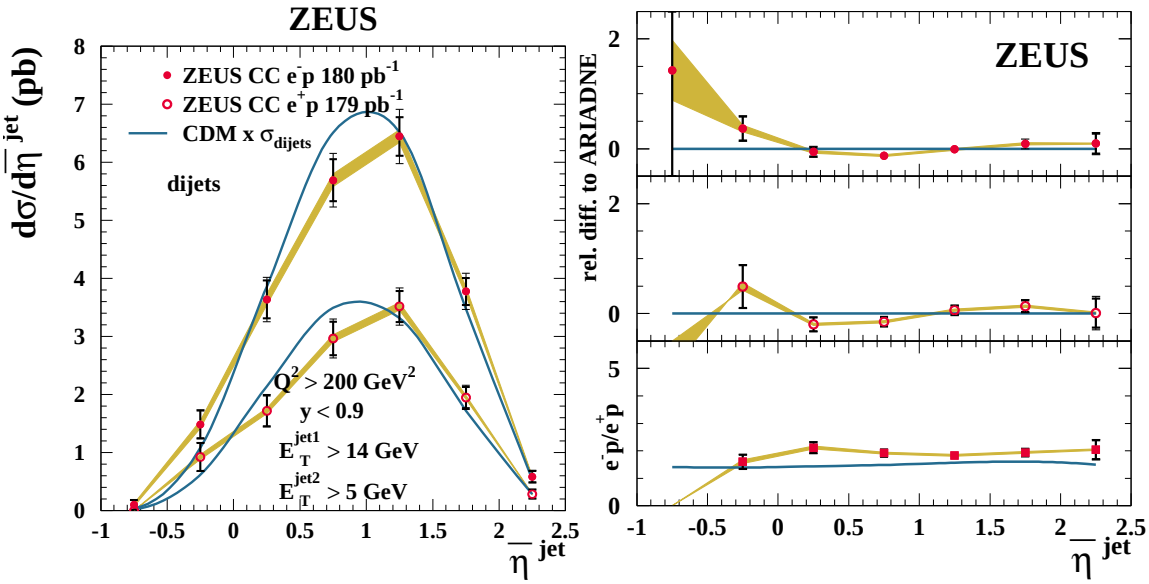

Figure 8.7: Unpolarized $e^- p$ and $e^+ p$ $\overline{\eta}^{\rm jet}$ Dijet Cross sections

The NLO predictions give a reasonable description of the ratios of the cross sections for $e^- p$ and $e^+ p$ interactions (see Fig. **??**). New implementations of the theory are crucially needed to use the differential dijet cross sections presented here in global fits to extract the proton PDFs.The integrated unpolarized dijet cross sections are shown in Table **??**. The measured cross sections are larger than the MEPJET predictions.

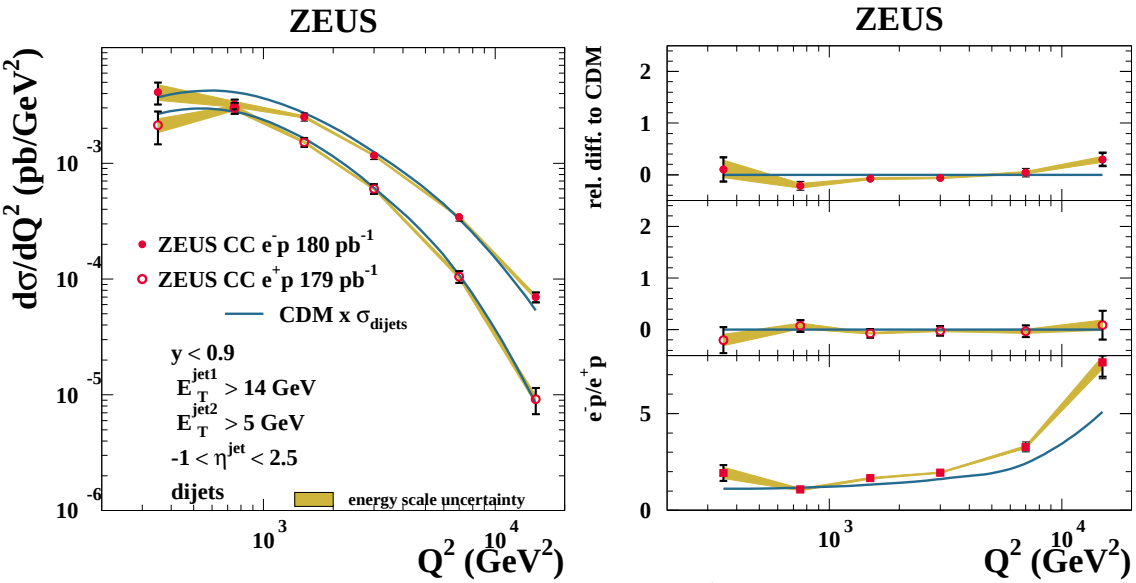

Figure 8.8: Unpolarized e^-p and e^+p Q^2 Dijet Cross sections

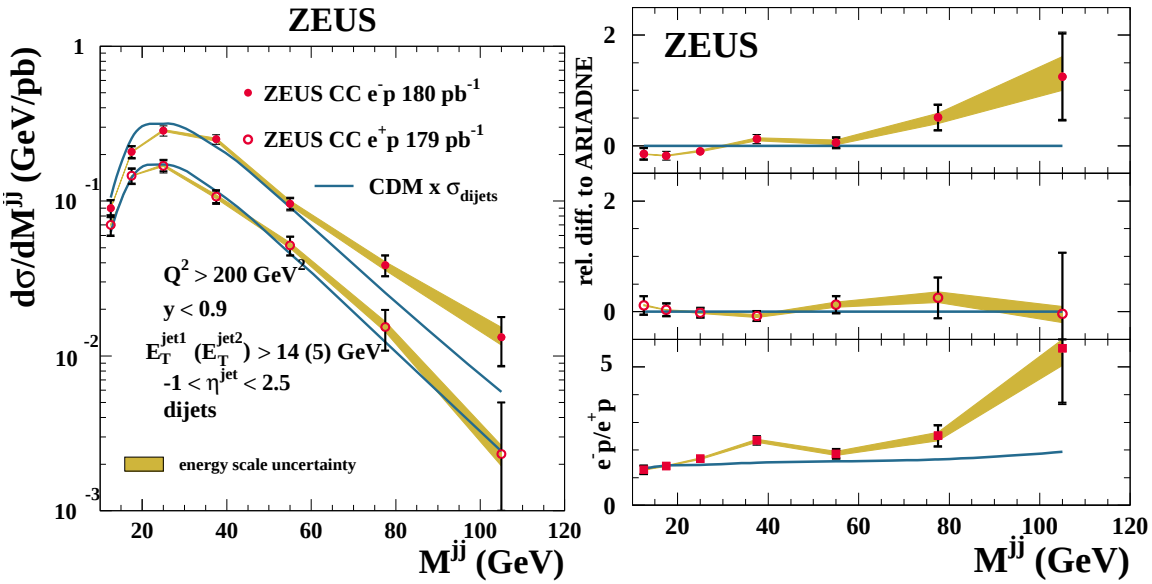

Figure 8.9: Unpolarized e^-p and e^+p m^{dijet} Dijet Cross sections

8.4 Trijet Unpolarized Differential Cross Sections

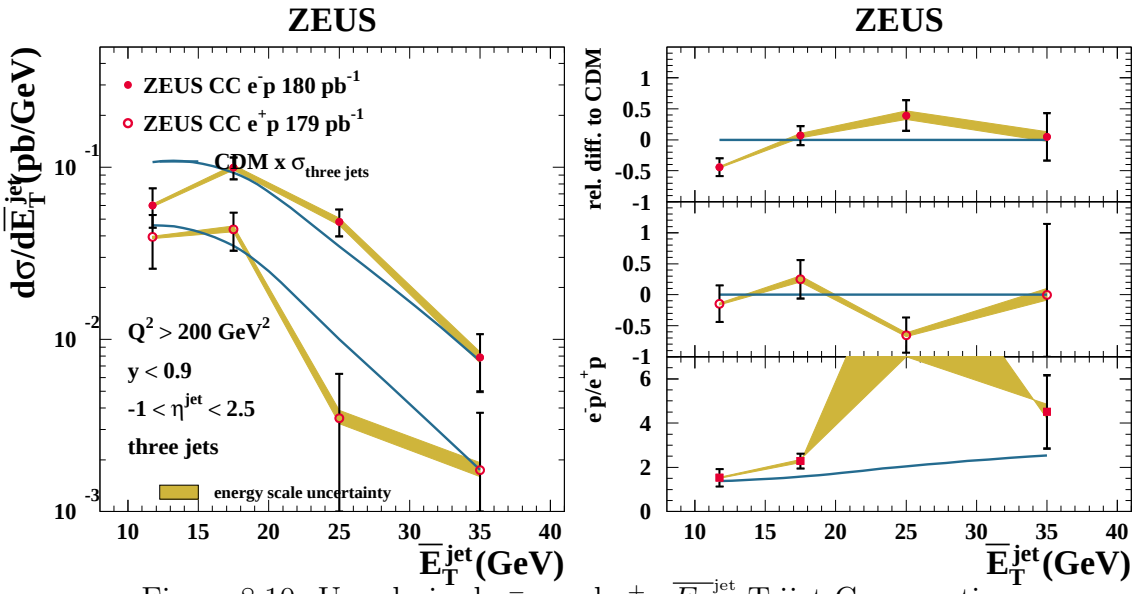

Figure 8.10: Unpolarized e^-p and e^+p $\overline{E_T}^{\text{jet}}$ Trijet Cross sections

Differential three-jet cross sections were measured in the kinematic regime $Q^2 >$ 200 GeV^2 and $y < 0.9$. The cross sections were determined for jets with $E_T^{\text{jet1}} > 14$ GeV, $E_T^{\text{jet2}} > 5$ GeV, $E_T^{\text{jet3}} > 5$ GeV and $-1 < \eta^{\text{jet}} < 2.5$. Three-jet cross sections in CC DIS were measured for the first time in $e^{\pm}p$ collisions.

Figure **??** shows a three-jet candidate event in the ZEUS detector: a clear three-jet topology and large transverse momentum are observed. The three-jet selected sample also contains 9 e^-p and 2 e^+p candidates with a fourth jet of transverse energy above 5 GeV in the η^{jet} range considered. One of these candidates is displayed in Fig. **??**: the fourth jet is clearly observed in the ZEUS detector.

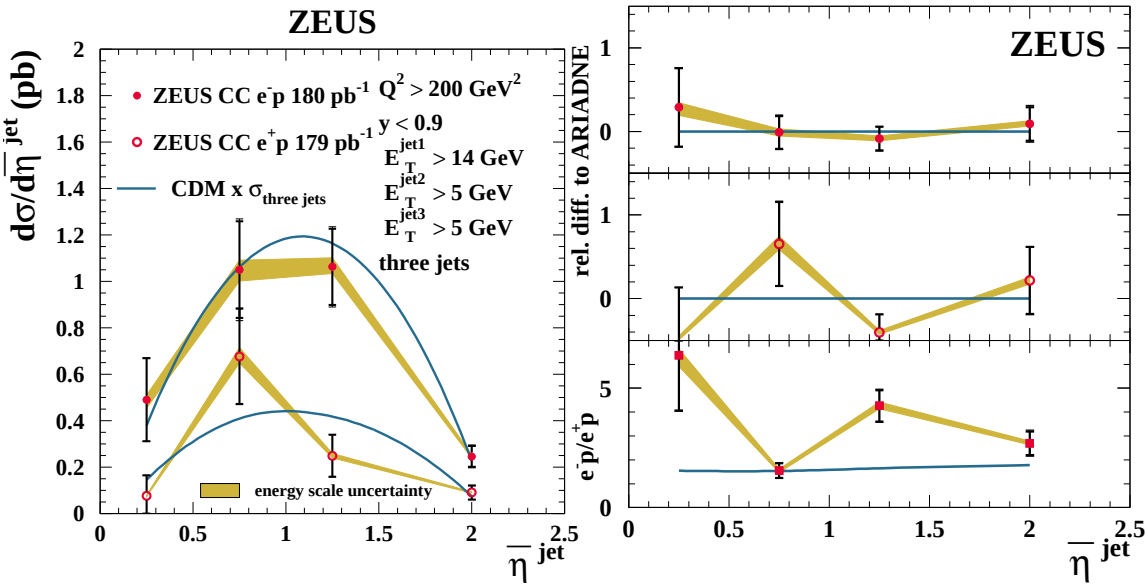

Figure 8.11: Unpolarized e^-p and e^+p $\overline{\eta}^{\rm jet}$ Trijet Cross sections

Figure **??** and Tables C.6 to C.11, C.15 and C.16 show the unpolarized three-jet differential cross sections as functions of $\overline{\eta}^{\rm jet}$, $\overline{E_T}^{\rm jet}$, Q^2 and the three-jet invariant mass, $m^{\rm trijet}$, where $\overline{\eta}^{\rm jet} = (\eta^{\rm jet1} + \eta^{\rm jet2} + \eta^{\rm jet3})/3$ and $\overline{E_T}^{\rm jet} = (E_T^{\rm jet1} + E_T^{\rm jet2} + E_T^{\rm jet3})/3$ in CC $e^{\pm}p$ DIS. Values of $m^{\rm trijet}$ above 100 GeV are accessible with the present statistics.

The predictions of LO QCD are compared to the data in Fig. **??**. The currently available QCD calculations are only lowest order and cannot predict the normalization of the data. Therefore, they were scaled by 1.92 and 1.42 for e^-p and e^+p collisions, respectively, so as to reproduce the measured integrated three-jet cross section. The scaled LO calculations give a good description of the shape of the data. Figure **??** shows the relative difference between the data and the scaled predictions. The lower part of Fig. **??** shows the ratio of the differential cross sections for the e^-p and e^+p samples.

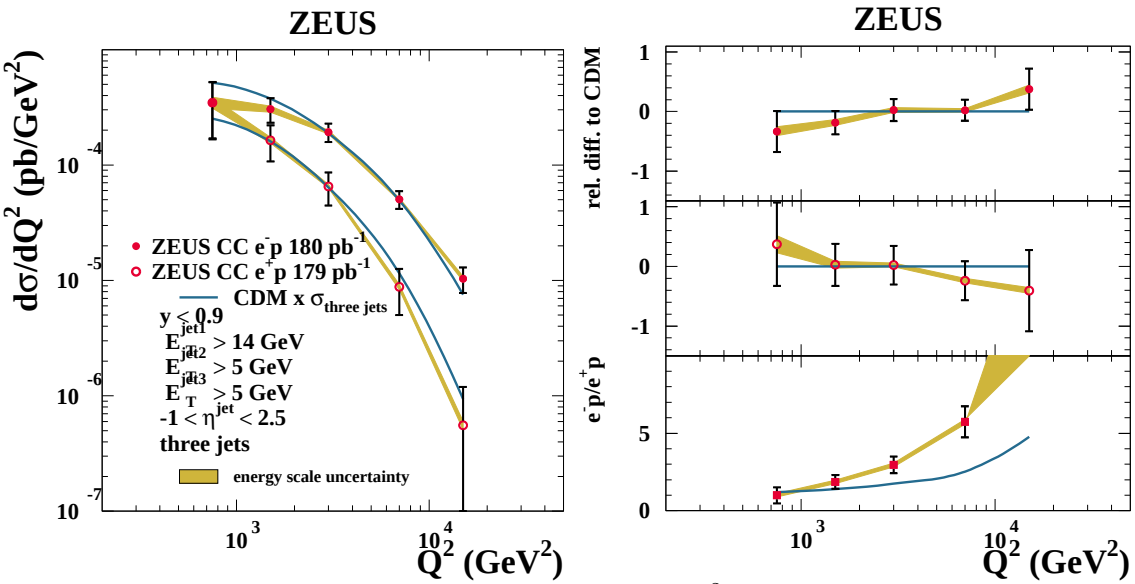

Figure 8.12: Unpolarized e^-p and e^+p Q^2 Trijet Cross sections

The integrated unpolarized three-jet cross sections are shown in Table C.14. The predictions of LO QCD are also shown in the table.

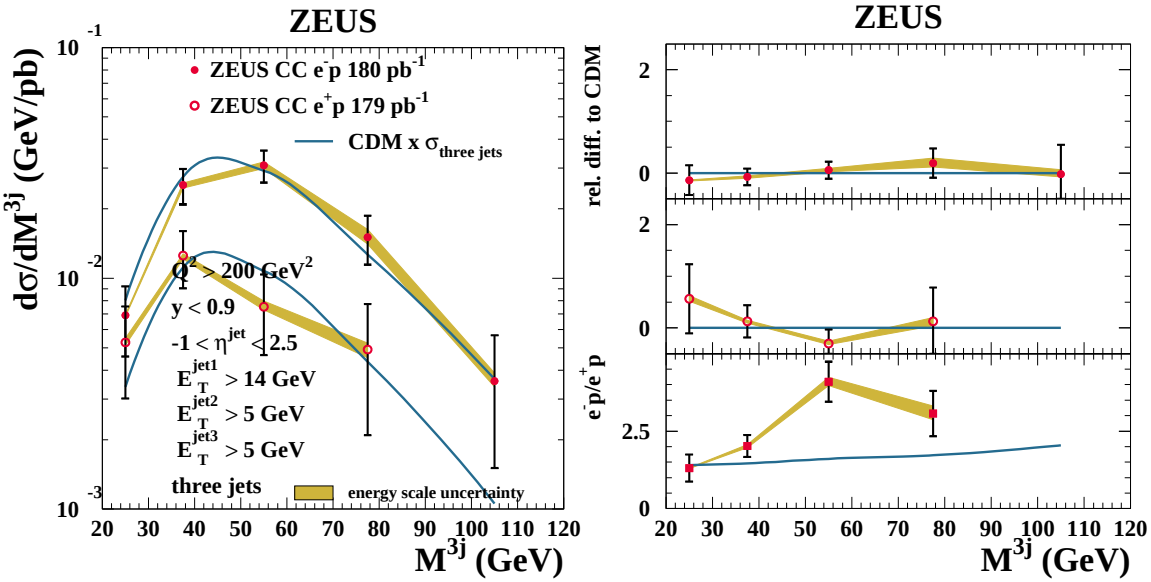

Figure 8.13: Unpolarized $e^- p$ and $e^+ p$ m^{trijet} Trijet Cross sections

Chapter 9

Conclusions

Measurements of polarized and unpolarized integrated and differential multi-jet cross sections in CC $e^{\pm}p$ DIS were made using 0.36 fb^{-1} of data collected with the ZEUS detector at HERA II. The measurements were made in the kinematic region defined by $Q^2 > 200$ GeV^2 and $y < 0.9$. Jets were identified in the laboratory frame using the k_T cluster algorithm in the longitudinally invariant inclusive mode.

Polarized inclusive-jet cross sections were measured integrated over the phase-space region considered and differentially as functions of $\eta^{\rm jet}$, $E_T^{\rm jet}$, Q^2 and x for jets with $E_T^{\rm jet} > 14$ GeV and $-1 < \eta^{\rm jet} < 2.5$. The measured cross sections are in good agreement with the SM predictions. The ratios of the differential cross sections for negative and positive longitudinally-polarized lepton beams are also well described by the predictions.

Unpolarized differential inclusive-jet cross sections were measured as functions of $\eta^{\rm jet}$, $E_T^{\rm jet}$, Q^2 and x. The ratio of the differential cross sections for e^-p and e^+p collisions as a function of $\eta^{\rm jet}$ is ≈ 2 in the $\eta^{\rm jet}$ range measured, as predicted by the theory. The ratio as a function of $E_T^{\rm jet}$ (Q^2) increases as $E_T^{\rm jet}$ (Q^2) increases, in agreement with the expected increased contribution from the valence-quark densities in the proton at

high x and the fact that both reactions are sensitive to different quark flavors. Dijet differential cross sections were measured for jets with $etjeta > 14$ GeV, $etjetb > 5$ GeV and $-1 < \eta^{\rm jet} < 2.5$.

Next-to-leading-order QCD predictions computed using the program MEPJET were compared to the data. The NLO QCD predictions give a good description of the measured inclusive-jet cross sections. A detailed study of the theoretical uncertainties was performed: they are dominated by the contribution from the PDFs. Furthermore, the uncertainties due to the PDFs are larger for e^+p than for e^-p collisions. Therefore, these measurements, if used together with other data in global fits, have the potential to constrain the flavor content of the proton at high x.

The comparison of the predictions with the measured dijet differential cross sections shows a poor agreement in shape and normalization. Improved implementations of the theory are crucially needed to use these dijet measurements in a global fit to constrain the proton PDFs.

Three-jet differential cross sections were measured for the first time in $e^{\pm}p$ collisions for jets with $E_T^{\rm jet1} > 14$ GeV, $E_T^{\rm jet2} > 5$ GeV, $E_T^{\rm jet3} > 5$ GeV and $-1 < \eta^{\rm jet} < 2.5$. The leading-order QCD predictions give a good description of the shape of the data. The three-jet sample also contains eleven candidates with a fourth jet of $E_T^{\rm jet} > 5$ GeV in the $\eta^{\rm jet}$ range considered.

Appendix A

Monte Carlo And Data Comparisons

In this appendix, supplimentary comparisons between data and monte carlo are presented for e^+p events. Equivalent comparisons are shown in section 7.1.2.

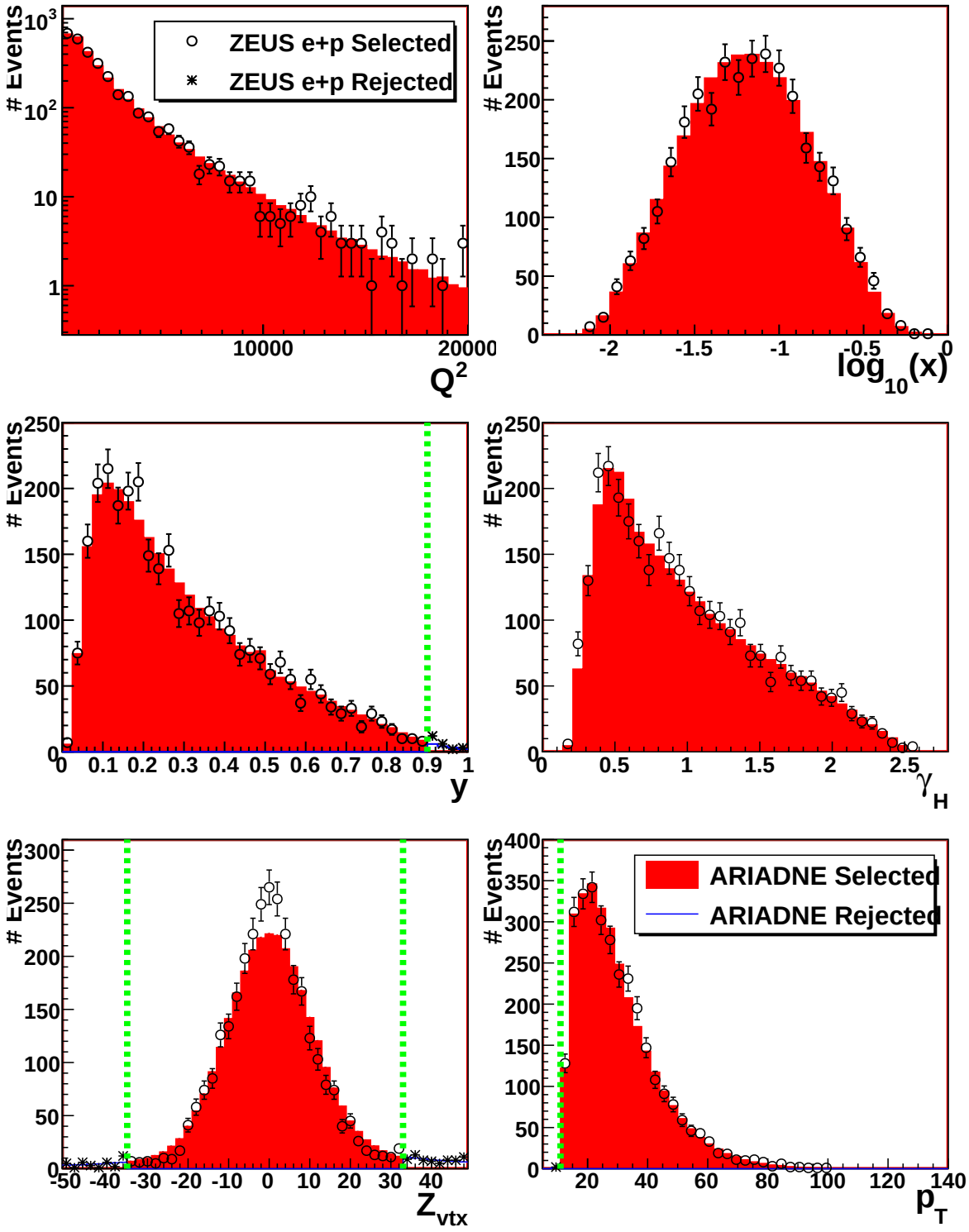

Figure A.1: Comparison between detector level kinematic quantities of e^+p data and ARIADNE. All details as in figure 7.1.

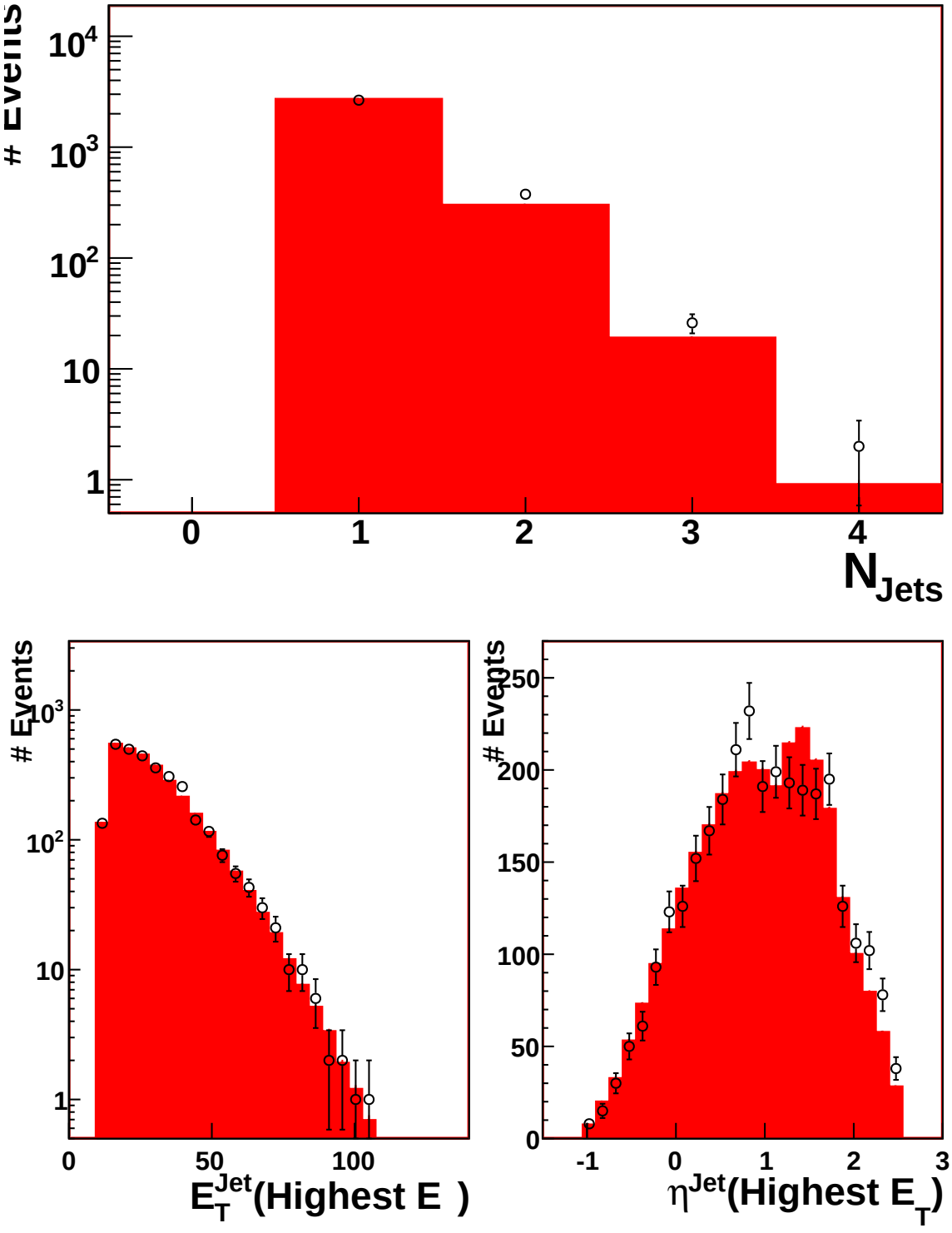

Figure A.2: Comparison between detector level jet quantities of e^+p data and ARIADNE. All details as in figure 7.2.

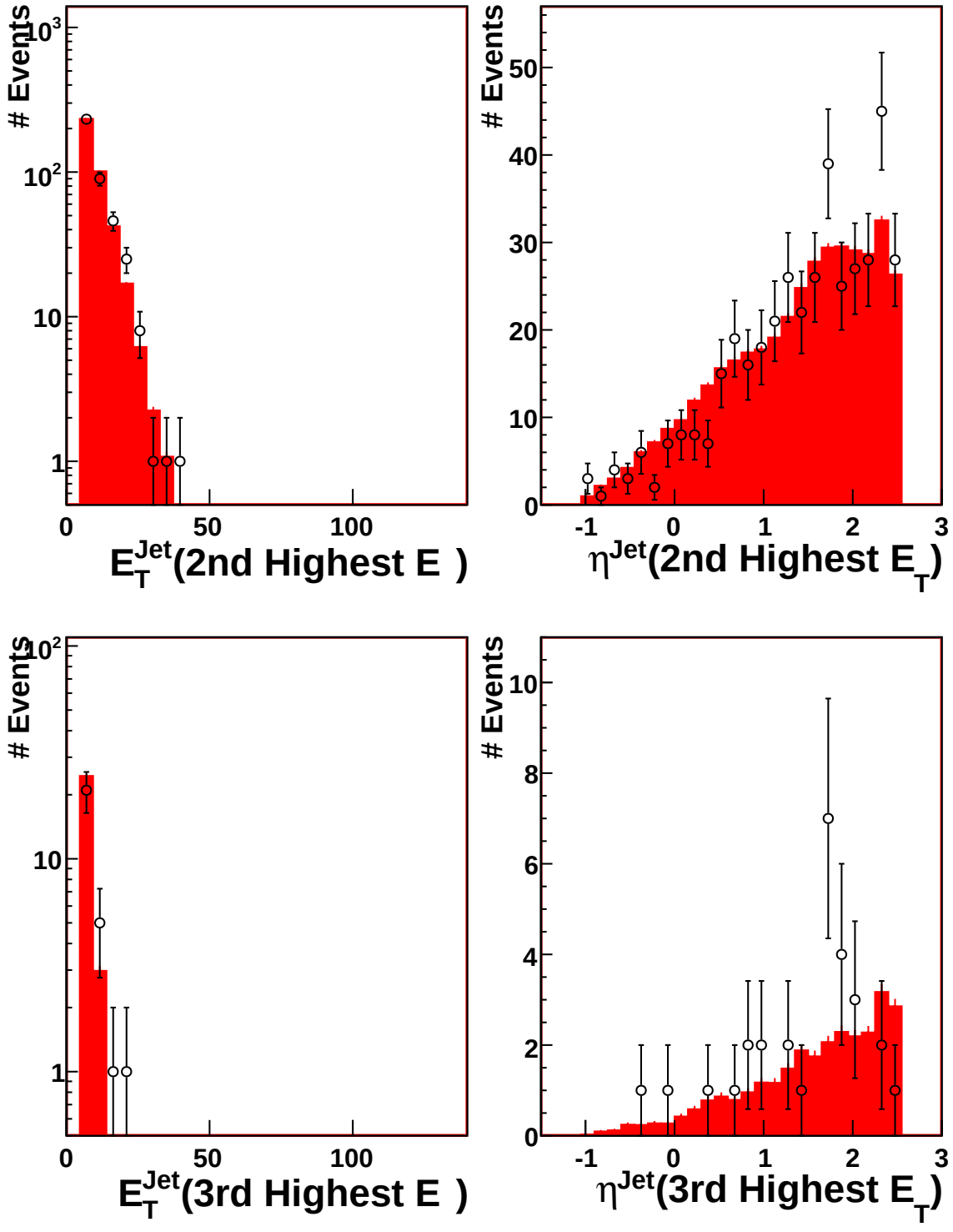

Figure A.3: Comparison between detector level jet quantities of e^+p data and ARIADNE. All details as in figure 7.2.

Appendix B

Reweighting Factors

The weight as a function of the generated z_{vtx} was computed as

$$w_z(z_{vtx}^{gen}) = 0.999 - 1.272 \times 10^{-3} * z_{vtx}^{gen} \text{ for electrons} \quad \text{(B.1)}$$

$$w_z(z_{vtx}^{gen}) = 0.982 - 4.966 \times 10^{-3} * z_{vtx}^{gen} \text{ for positrons} \quad \text{(B.2)}$$

The weight as a function of the generated Q^2 was computed as

$$w_{Q^2}(Q^2_{gen}) = 1.464 - 0.1385 \times 10^{-3} * \log_{10}(Q^2_{gen}) \text{ for electrons} \quad \text{(B.3)}$$

$$w_{Q^2}(Q^2_{gen}) = 1.5542 + -0.2147 \times 10^{-3} * \log_{10}(Q^2_{gen}) \text{ for positrons} \quad \text{(B.4)}$$

The weight function to account for the tracking veto was provided by the ZEUS tracking group, and will not be discussed here.

The effects of the reweighting are shown in figures B.1 and B.2. It can be seen from the figures that the reweighting procedure greatly improves the overal description of Q^2 for both samples. The z_{vtx} distribution for all ZEUS monte carlo is generated to empirically match the data for the run ranges considered. The difference in shape of the z_{vtx} distribution shown for positron data in figure B.2 is because the monte carlo was generated before the end of data taking, and the z_{vtx} distribution used does not represent that of the final data sample.

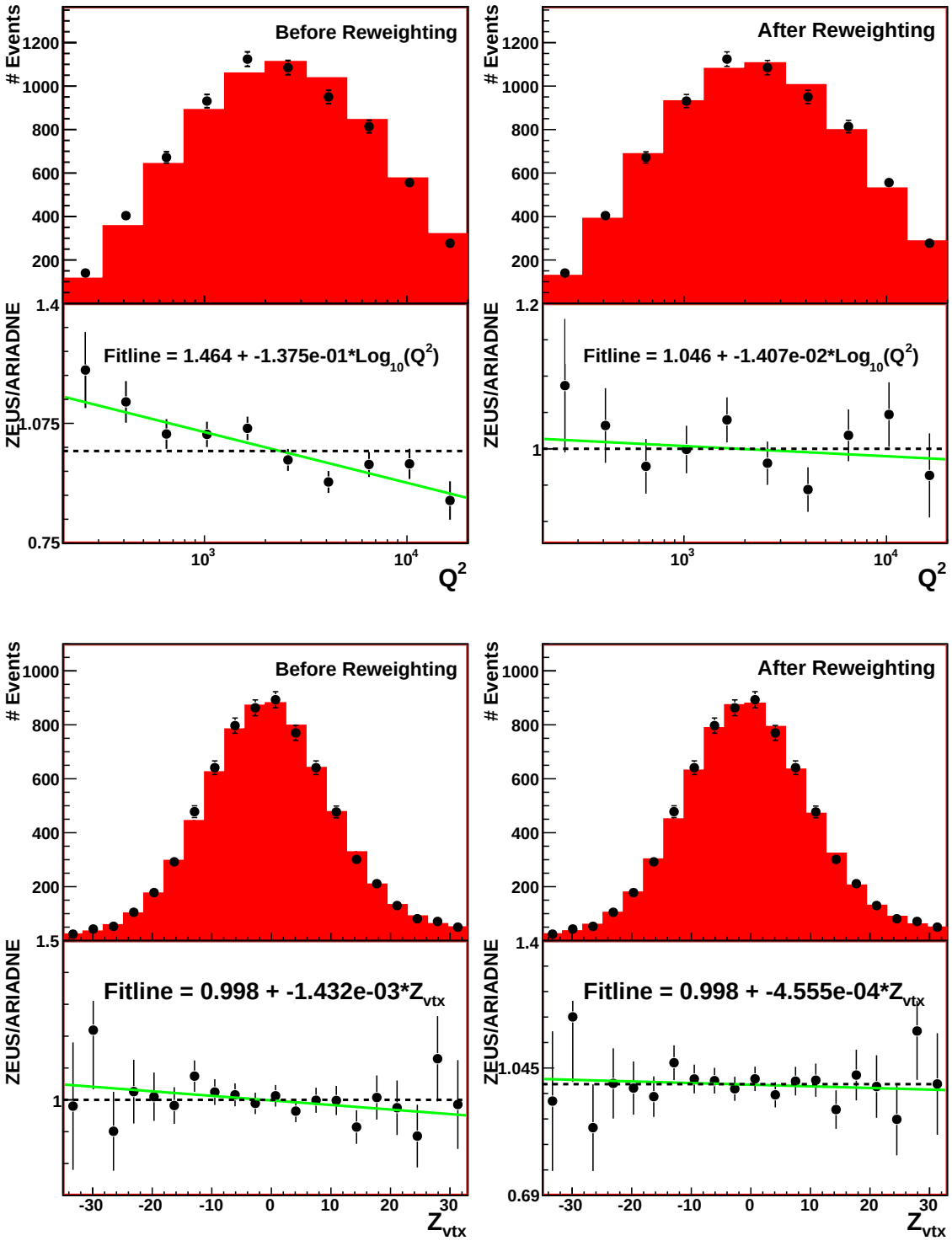

Figure B.1: Plots comparing detector level distributions of $e^- p$ data versus ARIADNE. The two upper plots show Q^2, while the bottom two show z_{vtx}. The left two plots show distributions without monte carlo reweighting, while the right two show the same data distributions, but compared to reweighted monte carlo. The monte carlo distributions have been area-normalized to the data. Below each distribution, a ratio plot is shown of data/ARIADNE. A linear χ^2 fit is shown for each ratio.

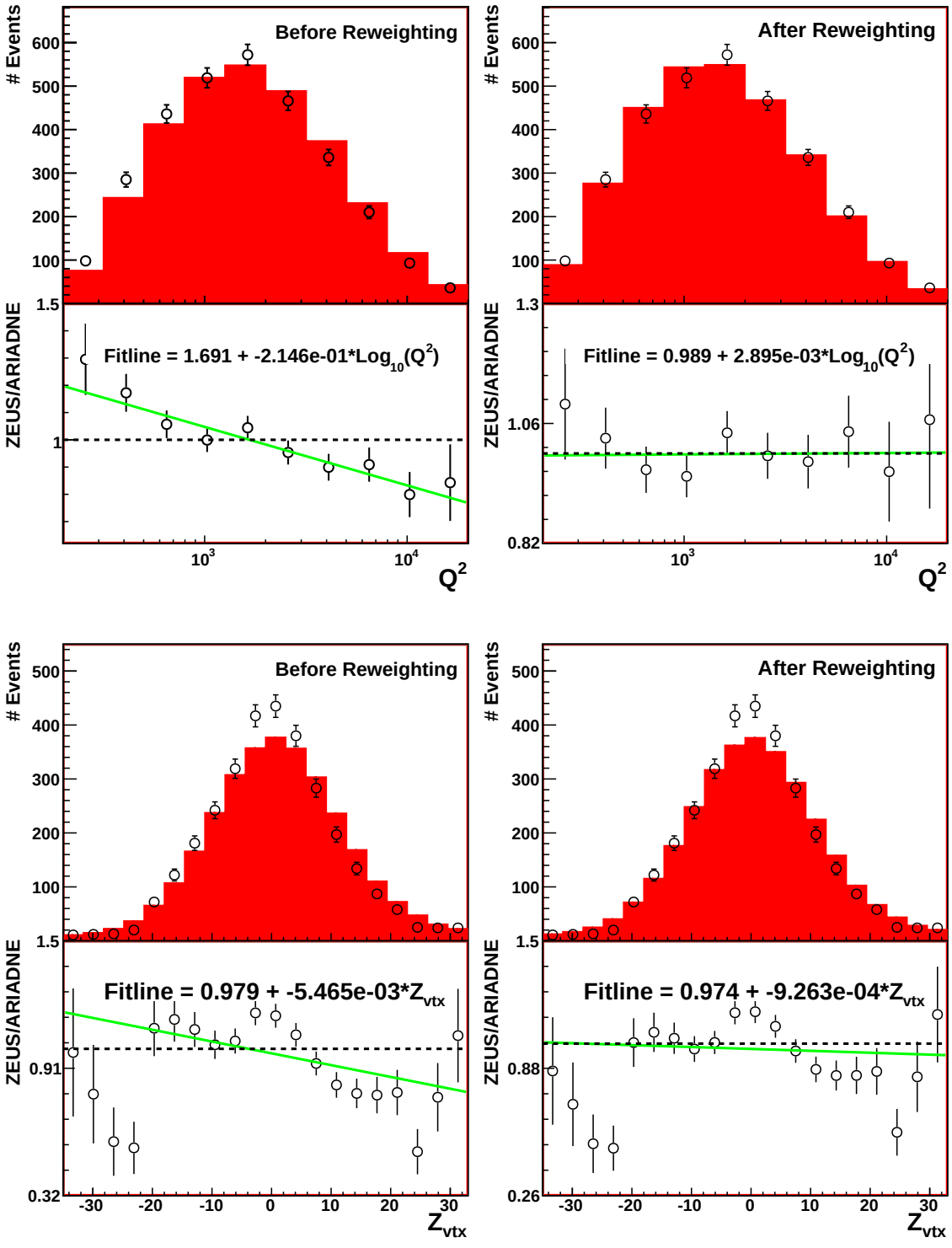

Figure B.2: Plots comparing detector level distributions of e^+p data versus ARIADNE. All details as in figure B.1.

Appendix C

Data Tables

η^{jet} bin	$d\sigma/d\eta^{\text{jet}}$ (pb)	δ_{stat}	δ_{syst}	δ_{ES}
$P_{e^-} = -0.27$ - inclusive jets				
$-1.0, -0.5$	4.22	± 0.38	± 0.32	$^{+0.17}_{-0.16}$
$-0.5, 0.0$	13.35	± 0.62	± 0.51	$^{+0.30}_{-0.29}$
$0.0, 0.5$	23.40	± 0.77	± 0.29	$^{+0.23}_{-0.22}$
$0.5, 1.0$	27.77	± 0.81	± 0.82	± 0.09
$1.0, 1.5$	28.30	± 0.82	± 0.92	$^{+0.08}_{-0.09}$
$1.5, 2.0$	24.71	± 0.79	± 0.40	$^{+0.10}_{-0.09}$
$2.0, 2.5$	19.41	± 0.87	± 2.36	± 0.15
$P_{e^-} = +0.30$ - inclusive jets				
$-1.0, -0.5$	2.81	± 0.37	± 0.21	$^{+0.11}_{-0.10}$
$-0.5, 0.0$	7.22	± 0.55	± 0.28	± 0.16
$0.0, 0.5$	12.45	± 0.67	± 0.47	$^{+0.12}_{-0.11}$
$0.5, 1.0$	16.05	± 0.74	± 0.48	± 0.05
$1.0, 1.5$	15.99	± 0.74	± 0.50	± 0.05
$1.5, 2.0$	15.34	± 0.75	± 0.42	$^{+0.06}_{-0.05}$
$2.0, 2.5$	11.39	± 0.80	± 1.37	± 0.09
$P_{e^+} = -0.37$ - inclusive jets				
$-1.0, -0.5$	1.26	± 0.28	± 0.14	± 0.04
$-0.5, 0.0$	3.33	± 0.38	± 0.16	± 0.05
$0.0, 0.5$	5.68	± 0.47	± 0.14	± 0.04
$0.5, 1.0$	6.64	± 0.49	± 0.40	± 0.04
$1.0, 1.5$	6.74	± 0.49	± 0.24	± 0.03
$1.5, 2.0$	6.52	± 0.50	± 0.07	± 0.04
$2.0, 2.5$	5.09	± 0.55	± 0.93	± 0.06
$P_{e^+} = +0.32$ - inclusive jets				
$-1.0, -0.5$	2.92	± 0.36	± 0.30	± 0.09
$-0.5, 0.0$	7.37	± 0.49	± 0.29	± 0.11
$0.0, 0.5$	10.34	± 0.54	± 0.41	± 0.08
$0.5, 1.0$	14.75	± 0.63	± 0.65	± 0.08
$1.0, 1.5$	12.38	± 0.58	± 0.65	± 0.06
$1.5, 2.0$	11.64	± 0.58	± 0.50	$^{+0.07}_{-0.06}$
$2.0, 2.5$	10.22	± 0.68	± 1.26	± 0.12

Table C.1: Differential polarized inclusive-jet cross-sections $d\sigma/d\eta^{\text{jet}}$ for jets of hadrons in the laboratory frame selected with the longitudinally invariant k_T cluster algorithm. The statistical, uncorrelated systematic and energy-scale (ES) uncertainties are shown separately.

$E_T^{\rm jet}$ bin (GeV)	$d\sigma/dE_T^{\rm jet}$ (pb/GeV)	$\delta_{\rm stat}$	$\delta_{\rm syst}$	$\delta_{\rm ES}$
$P_{e^-} = -0.27$ - inclusive jets				
14, 21	2.318	± 0.076	± 0.140	$^{+0.045}_{-0.051}$
21, 29	1.776	± 0.056	± 0.079	$^{+0.019}_{-0.018}$
29, 41	1.419	± 0.038	± 0.070	$^{+0.009}_{-0.010}$
41, 55	0.834	± 0.027	± 0.051	$^{+0.011}_{-0.010}$
55, 71	0.450	± 0.018	± 0.022	± 0.011
71, 87	0.212	± 0.012	± 0.057	$^{+0.003}_{-0.002}$
87, 120	0.0421	± 0.0035	± 0.0225	$^{+0.0063}_{-0.0050}$
$P_{e^-} = +0.30$ - inclusive jets				
14, 21	1.284	± 0.068	± 0.089	$^{+0.025}_{-0.028}$
21, 29	1.081	± 0.052	± 0.049	$^{+0.012}_{-0.011}$
29, 41	0.795	± 0.035	± 0.041	$^{+0.005}_{-0.006}$
41, 55	0.486	± 0.024	± 0.030	± 0.006
55, 71	0.263	± 0.017	± 0.016	$^{+0.007}_{-0.006}$
71, 87	0.106	± 0.010	± 0.029	± 0.001
87, 120	0.0276	± 0.0035	± 0.0149	$^{+0.0041}_{-0.0033}$
$P_{e^+} = -0.37$ - inclusive jets				
14, 21	0.761	± 0.053	± 0.058	± 0.012
21, 29	0.584	± 0.039	± 0.031	$^{+0.003}_{-0.004}$
29, 41	0.338	± 0.023	± 0.019	$^{+0.004}_{-0.003}$
41, 55	0.160	± 0.014	± 0.011	± 0.004
55, 71	0.0602	± 0.0079	± 0.0037	$^{+0.0025}_{-0.0023}$
71, 87	0.0157	± 0.0039	± 0.0047	$^{+0.0007}_{-0.0006}$
87, 120	0.00166	± 0.00083	± 0.00106	$^{+0.00032}_{-0.00025}$
$P_{e^+} = +0.32$ - inclusive jets				
14, 21	1.576	± 0.066	± 0.112	$^{+0.026}_{-0.024}$
21, 29	1.077	± 0.045	± 0.020	$^{+0.006}_{-0.007}$
29, 41	0.675	± 0.028	± 0.037	$^{+0.007}_{-0.006}$
41, 55	0.307	± 0.017	± 0.020	± 0.007
55, 71	0.1135	± 0.0094	± 0.0143	$^{+0.0047}_{-0.0043}$
71, 87	0.0374	± 0.0052	± 0.0083	$^{+0.0016}_{-0.0014}$
87, 120	0.0050	± 0.0012	± 0.0027	$^{+0.0010}_{-0.0008}$

Table C.2: Differential polarized inclusive-jet cross-sections $d\sigma/dE_T^{\rm jet}$. Other details as in the caption to Table C.1.

Q^2 bin (GeV^2)	$d\sigma/dQ^2$ (pb/GeV^2)	$\delta_{\rm stat}$	$\delta_{\rm syst}$	$\delta_{\rm ES}$
$P_{e^-} = -0.27$ - inclusive jets				
$200, 500$	0.0246	± 0.0013	± 0.0015	$^{+0.0024}_{-0.0023}$
$500, 1000$	0.02226	± 0.00079	± 0.00090	$^{+0.00061}_{-0.00059}$
$1000, 2000$	0.01578	± 0.00046	± 0.00053	± 0.00022
$2000, 4000$	0.00797	± 0.00023	± 0.00007	± 0.00004
$4000, 10000$	0.002532	± 0.000072	± 0.000134	± 0.000038
$10000, 20000$	0.000429	± 0.000022	± 0.000029	± 0.000018
$20000, 88000$	$1.4 \cdot 10^{-5}$	$\pm 1.3 \cdot 10^{-6}$	$\pm 5.7 \cdot 10^{-6}$	$\pm 1.4 \cdot 10^{-6}$
$P_{e^-} = +0.30$ - inclusive jets				
$200, 500$	0.0135	± 0.0011	± 0.0011	± 0.0013
$500, 1000$	0.01332	± 0.00074	± 0.00051	$^{+0.00036}_{-0.00035}$
$1000, 2000$	0.00926	± 0.00042	± 0.00030	± 0.00013
$2000, 4000$	0.00437	± 0.00020	± 0.00004	± 0.00002
$4000, 10000$	0.001364	± 0.000064	± 0.000075	± 0.000020
$10000, 20000$	$30.6 \cdot 10^{-5}$	$\pm 2.2 \cdot 10^{-5}$	$\pm 2.0 \cdot 10^{-5}$	$\pm 1.3 \cdot 10^{-5}$
$20000, 88000$	$8.1 \cdot 10^{-6}$	$\pm 1.2 \cdot 10^{-6}$	$\pm 3.3 \cdot 10^{-6}$	$\pm 0.8 \cdot 10^{-6}$
$P_{e^+} = -0.37$ - inclusive jets				
$200, 500$	0.00984	± 0.00096	± 0.00049	$^{+0.00091}_{-0.00087}$
$500, 1000$	0.00814	± 0.00058	± 0.00026	± 0.00016
$1000, 2000$	0.00463	± 0.00030	± 0.00022	± 0.00002
$2000, 4000$	0.00182	± 0.00013	± 0.00007	± 0.00003
$4000, 10000$	$34.1 \cdot 10^{-5}$	$\pm 3.1 \cdot 10^{-5}$	$\pm 2.0 \cdot 10^{-5}$	$\pm 1.4 \cdot 10^{-5}$
$10000, 20000$	$25.0 \cdot 10^{-6}$	$\pm 5.9 \cdot 10^{-6}$	$\pm 5.7 \cdot 10^{-6}$	$\pm 2.3 \cdot 10^{-6}$
$P_{e^+} = +0.32$ - inclusive jets				
$200, 500$	0.0198	± 0.0012	± 0.0010	$^{+0.0018}_{-0.0017}$
$500, 1000$	0.01586	± 0.00070	± 0.00023	$^{+0.00030}_{-0.00031}$
$1000, 2000$	0.00905	± 0.00036	± 0.00027	$^{+0.00004}_{-0.00004}$
$2000, 4000$	0.00345	± 0.00016	± 0.00014	$^{+0.00005}_{-0.00005}$
$4000, 10000$	$68.8 \cdot 10^{-5}$	$\pm 3.9 \cdot 10^{-5}$	$\pm 5.6 \cdot 10^{-5}$	$\pm 2.7 \cdot 10^{-5}$
$10000, 20000$	$61.3 \cdot 10^{-6}$	$\pm 8.0 \cdot 10^{-6}$	$\pm 10.0 \cdot 10^{-6}$	$\pm 5.6 \cdot 10^{-6}$
$20000, 88000$	$3.5 \cdot 10^{-7}$	$\pm 1.8 \cdot 10^{-7}$	$\pm 2.8 \cdot 10^{-7}$	$\pm 0.6 \cdot 10^{-7}$

Table C.3: Differential polarized inclusive-jet cross-sections $d\sigma/dQ^2$. Other details as in the caption to Table C.1.

x bin	$d\sigma/dx$ (pb/GeV)	δ_{stat}	δ_{syst}	δ_{ES}
$P_{e^-} = -0.27$ - inclusive jets				
$0.006, 0.025$	16.17	± 0.70	± 0.83	$^{+1.06}_{-1.01}$
$0.025, 0.063$	46.9	± 1.3	± 1.6	± 0.9
$0.063, 0.16$	60.6	± 1.4	± 0.9	± 0.2
$0.16, 0.40$	39.7	± 1.1	± 1.7	± 0.7
$0.40, 1.0$	3.94	± 0.33	± 0.53	± 0.29
$P_{e^-} = +0.30$ - inclusive jets				
$0.006, 0.025$	9.71	± 0.65	± 0.76	$^{+0.64}_{-0.61}$
$0.025, 0.063$	24.3	± 1.1	± 0.9	± 0.5
$0.063, 0.16$	36.6	± 1.3	± 0.6	± 0.1
$0.16, 0.40$	23.2	± 1.0	± 1.2	± 0.4
$0.40, 1.0$	2.21	± 0.30	± 0.38	± 0.16
$P_{e^+} = -0.37$ - inclusive jets				
$0.006, 0.025$	6.10	± 0.54	± 0.28	$^{+0.35}_{-0.34}$
$0.025, 0.063$	13.59	± 0.81	± 0.53	± 0.15
$0.063, 0.16$	14.90	± 0.82	± 0.62	± 0.16
$0.16, 0.40$	5.22	± 0.47	± 0.30	± 0.13
$0.40, 1.0$	0.33	± 0.11	± 0.12	± 0.02
$P_{e^+} = +0.32$ - inclusive jets				
$0.006, 0.025$	12.34	± 0.67	± 0.56	$^{+0.71}_{-0.69}$
$0.025, 0.063$	28.1	± 1.0	± 1.0	± 0.3
$0.063, 0.16$	26.57	± 0.95	± 0.88	± 0.29
$0.16, 0.40$	11.55	± 0.60	± 0.65	± 0.28
$0.40, 1.0$	0.50	± 0.12	± 0.06	± 0.04

Table C.4: Differential polarized inclusive-jet cross-sections $d\sigma/dx$. Other details as in the caption to Table C.1.

lepton and polarization	σ_{jets} (pb)	δ_{stat} (pb)	δ_{syst} (pb)	δ_{ES} (pb)	SM prediction (pb)
$P_{e^-} = -0.27 \pm 0.01$	70.54	0.97	0.58	$^{+0.43}_{-0.40}$	69.17
$P_{e^-} = +0.29 \pm 0.01$	40.53	0.88	0.45	$^{+0.24}_{-0.23}$	38.67
$P_{e^+} = -0.37^{+0.01}_{-0.02}$	17.55	0.60	0.57	± 0.11	16.86
$P_{e^+} = +0.32 \pm 0.01$	34.51	0.72	1.05	$^{+0.23}_{-0.22}$	35.33

Table C.5: Integrated polarized inclusive-jet cross-sections σ_{jets} for jets of hadrons in the laboratory frame selected with the longitudinally invariant k_T cluster algorithm. The statistical, uncorrelated systematic and energy-scale (ES) uncertainties are shown separately. The uncertainty coming from the luminosity measurement is not shown. The predictions of the Standard Model as given by the MEPJETcalculation are shown in the last column.

η^{jet} bin	$d\sigma/d\eta^{\text{jet}}$ (pb)	δ_{stat}	δ_{syst}	δ_{ES}	C_{QED}	C_{had}
unpolarized - inclusive jets						
$-1.0, -0.5$	3.58	± 0.28	± 0.30	$^{+0.15}_{-0.13}$	0.97	0.93
$-0.5, 0.0$	10.38	± 0.43	± 0.35	$^{+0.24}_{-0.22}$	0.97	0.98
$0.0, 0.5$	18.06	± 0.53	± 0.34	± 0.17	0.98	0.99
$0.5, 1.0$	22.17	± 0.57	± 0.75	± 0.07	0.97	1.00
$1.0, 1.5$	22.38	± 0.58	± 0.90	± 0.07	0.97	1.00
$1.5, 2.0$	20.33	± 0.57	± 0.31	$^{+0.08}_{-0.07}$	0.96	1.01
$2.0, 2.5$	15.59	± 0.61	± 1.85	± 0.12	0.96	1.01
$\overline{\eta}^{\text{jet}}$ bin	$d\sigma/d\overline{\eta}^{\text{jet}}$ (pb)	δ_{stat}	δ_{syst}	δ_{ES}	C_{QED}	C_{had}
unpolarized - dijets						
$-1.0, -0.5$	0.103	± 0.073	± 0.003	$^{+0.033}_{-0.032}$	0.80	0.60
$-0.5, 0.0$	1.48	± 0.26	± 0.52	± 0.09	0.96	0.81
$0.0, 0.5$	3.63	± 0.33	± 0.88	± 0.12	0.97	0.89
$0.5, 1.0$	5.68	± 0.37	± 0.43	$^{+0.14}_{-0.13}$	0.98	0.91
$1.0, 1.5$	6.43	± 0.34	± 0.07	$^{+0.12}_{-0.11}$	0.97	0.92
$1.5, 2.0$	3.77	± 0.24	± 0.14	± 0.07	0.95	0.92
$2.0, 2.5$	0.58	± 0.10	± 0.05	± 0.01	0.93	0.88
unpolarized - three jets						
$0.0, 0.5$	0.49	± 0.18	± 0.49	$^{+0.03}_{-0.05}$	0.95	0.75
$0.5, 1.0$	1.05	± 0.21	± 0.15	$^{+0.05}_{-0.06}$	0.93	0.78
$1.0, 1.5$	1.06	± 0.17	± 0.13	$^{+0.04}_{-0.03}$	0.99	0.80
$1.5, 2.5$	0.246	± 0.046	± 0.053	$^{+0.009}_{-0.007}$	0.99	0.80

Table C.6: Differential unpolarized inclusive-jet, dijet and three-jet cross-sections $d\sigma/d\eta^{\text{jet}}$ and $d\sigma/d\overline{\eta}^{\text{jet}}$ in $e^- p$ collisions for jets of hadrons in the laboratory frame selected with the longitudinally invariant k_T cluster algorithm. The statistical, uncorrelated systematic and jet-energy-scale (ES) uncertainties are shown separately. The multiplicative corrections for QED radiative effects, C_{QED}, and the corrections for hadronization effects, C_{had}, to be applied to the parton-level NLO QCD calculations, are shown in the last two columns.

$\eta^{\rm jet}$ bin	$d\sigma/d\eta^{\rm jet}$ (pb)	$\delta_{\rm stat}$	$\delta_{\rm syst}$	$\delta_{\rm ES}$	$C_{\rm QED}$	$C_{\rm had}$
unpolarized - inclusive jets						
$-1.0, -0.5$	2.12	± 0.24	± 0.21	$^{+0.07}_{-0.06}$	0.92	0.94
$-0.5, 0.0$	5.45	± 0.34	± 0.23	± 0.08	0.94	0.98
$0.0, 0.5$	8.34	± 0.39	± 0.22	± 0.06	0.95	0.99
$0.5, 1.0$	10.90	± 0.43	± 0.54	± 0.06	0.95	1.00
$1.0, 1.5$	9.95	± 0.42	± 0.42	± 0.05	0.95	1.00
$1.5, 2.0$	9.48	± 0.42	± 0.26	$^{+0.06}_{-0.05}$	0.94	1.01
$2.0, 2.5$	7.88	± 0.48	± 1.15	± 0.09	0.93	1.02
$\overline{\eta}^{\rm jet}$ bin	$d\sigma/d\overline{\eta}^{\rm jet}$ (pb)	$\delta_{\rm stat}$	$\delta_{\rm syst}$	$\delta_{\rm ES}$	$C_{\rm QED}$	$C_{\rm had}$
unpolarized - dijets						
$-0.5, 0.0$	0.92	± 0.23	± 0.33	$^{+0.07}_{-0.05}$	0.94	0.83
$0.0, 0.5$	1.75	± 0.28	± 0.42	$^{+0.06}_{-0.05}$	0.94	0.90
$0.5, 1.0$	3.01	± 0.32	± 0.24	$^{+0.07}_{-0.06}$	0.95	0.94
$1.0, 1.5$	3.52	± 0.28	± 0.06	$^{+0.07}_{-0.06}$	0.95	0.94
$1.5, 2.0$	1.95	± 0.20	± 0.11	± 0.04	0.94	0.94
$2.0, 2.5$	0.287	± 0.073	± 0.043	$^{+0.008}_{-0.005}$	0.93	0.91
unpolarized - three jets						
$0.0, 0.5$	0.079	± 0.079	± 0.079	$^{+0.006}_{-0.003}$	0.92	0.72
$0.5, 1.0$	0.68	± 0.23	± 0.09	$^{+0.04}_{-0.03}$	0.93	0.79
$1.0, 1.5$	0.254	± 0.086	± 0.033	$^{+0.011}_{-0.010}$	0.94	0.81
$1.5, 2.5$	0.087	± 0.029	± 0.019	± 0.003	0.91	0.83

Table C.7: Differential unpolarized inclusive-jet, dijet and three-jet cross-sections $d\sigma/d\eta^{\rm jet}$ and $d\sigma/\overline{\eta}^{\rm jet}$ in e^+p collisions. Other details as in the caption to Table C.6.

$E_T^{\rm jet}$ bin (GeV)	$d\sigma/dE_T^{\rm jet}$ (pb/GeV)	$\delta_{\rm stat}$	$\delta_{\rm syst}$	$\delta_{\rm ES}$	$C_{\rm QED}$	$C_{\rm had}$
unpolarized - inclusive jets						
$14, 21$	1.819	± 0.053	± 0.120	$^{+0.035}_{-0.040}$	1.03	0.99
$21, 29$	1.449	± 0.040	± 0.040	$^{+0.016}_{-0.014}$	1.01	1.00
$29, 41$	1.118	± 0.027	± 0.042	$^{+0.007}_{-0.008}$	0.97	1.00
$41, 55$	0.668	± 0.019	± 0.039	± 0.008	0.95	1.00
$55, 71$	0.361	± 0.013	± 0.031	± 0.009	0.92	0.99
$71, 87$	0.1596	± 0.0082	± 0.0360	$^{+0.0020}_{-0.0015}$	0.88	0.99
$87, 120$	0.0355	± 0.0026	± 0.0190	$^{+0.0053}_{-0.0042}$	0.83	0.98
$\overline{E_T}^{\rm jet}$ bin (GeV)	$d\sigma/d\overline{E_T}^{\rm jet}$ (pb/GeV)	$\delta_{\rm stat}$	$\delta_{\rm syst}$	$\delta_{\rm ES}$	$C_{\rm QED}$	$C_{\rm had}$
unpolarized - dijets						
$9.5, 14$	0.345	± 0.032	± 0.017	± 0.004	1.03	0.88
$14, 21$	0.502	± 0.028	± 0.077	$^{+0.007}_{-0.004}$	0.99	0.91
$21, 29$	0.375	± 0.021	± 0.030	± 0.010	0.94	0.92
$29, 41$	0.156	± 0.011	± 0.005	± 0.007	0.92	0.90
$41, 55$	0.0390	± 0.0049	± 0.0107	$^{+0.0037}_{-0.0026}$	0.88	0.90
$55, 71$	0.0070	± 0.0023	± 0.0007	$^{+0.0014}_{-0.0016}$	0.90	0.95
$71, 87$	0.0021	± 0.0021	± 0.0021	$^{+0.0014}_{-0.0000}$	1.00	0.94
unpolarized - three jets						
$8, 9.5$	0.0096	± 0.0096	± 0.0025	$^{+0.0016}_{-0.0017}$	1.02	0.72
$9.5, 14$	0.060	± 0.015	± 0.015	± 0.001	1.02	0.77
$14, 21$	0.099	± 0.015	± 0.003	± 0.004	0.96	0.79
$21, 29$	0.0481	± 0.0087	± 0.0036	$^{+0.0030}_{-0.0027}$	0.92	0.78
$29, 41$	0.0078	± 0.0029	± 0.0008	$^{+0.0007}_{-0.0006}$	0.86	0.85

Table C.8: Differential unpolarized inclusive-jet, dijet and three-jet cross-sections $d\sigma/dE_T^{\rm jet}$ and $d\sigma/d\overline{E_T}^{\rm jet}$ in $e^- p$ collisions. Other details as in the caption to Table C.6.

$E_T^{\rm jet}$ bin (GeV)	$d\sigma/dE_T^{\rm jet}$ (pb/GeV)	$\delta_{\rm stat}$	$\delta_{\rm syst}$	$\delta_{\rm ES}$	$C_{\rm QED}$	$C_{\rm had}$
unpolarized - inclusive jets						
$14, 21$	1.200	± 0.046	± 0.087	$^{+0.020}_{-0.019}$	0.99	1.00
$21, 29$	0.863	± 0.033	± 0.029	$^{+0.005}_{-0.006}$	0.96	1.00
$29, 41$	0.522	± 0.019	± 0.025	± 0.005	0.93	1.00
$41, 55$	0.242	± 0.012	± 0.016	± 0.006	0.91	0.99
$55, 71$	0.0901	± 0.0067	± 0.0078	$^{+0.0037}_{-0.0034}$	0.87	0.99
$71, 87$	0.0269	± 0.0035	± 0.0067	$^{+0.0011}_{-0.0010}$	0.84	0.98
$87, 120$	0.00329	± 0.00078	± 0.00179	$^{+0.00064}_{-0.00050}$	0.79	0.97
$\overline{E_T}^{\rm jet}$ bin (GeV)	$d\sigma/d\overline{E_T}^{\rm jet}$ (pb/GeV)	$\delta_{\rm stat}$	$\delta_{\rm syst}$	$\delta_{\rm ES}$	$C_{\rm QED}$	$C_{\rm had}$
unpolarized - dijets						
$9.5, 14$	0.288	± 0.033	± 0.017	$^{+0.001}_{-0.002}$	0.99	0.90
$14, 21$	0.330	± 0.026	± 0.052	± 0.004	0.95	0.93
$21, 29$	0.190	± 0.018	± 0.015	$^{+0.007}_{-0.006}$	0.93	0.93
$29, 41$	0.0433	± 0.0066	± 0.0023	$^{+0.0026}_{-0.0022}$	0.88	0.93
$41, 55$	0.0112	± 0.0032	± 0.0031	$^{+0.0014}_{-0.0010}$	0.90	0.95
unpolarized - three jets						
$8, 9.5$	0.019	± 0.019	± 0.005	± 0.002	0.82	0.73
$9.5, 14$	0.040	± 0.013	± 0.010	± 0.001	0.96	0.76
$14, 21$	0.043	± 0.012	± 0.002	± 0.002	0.93	0.80
$21, 29$	0.0034	± 0.0024	± 0.0003	$^{+0.0003}_{-0.0002}$	0.86	0.82
$29, 41$	0.0018	± 0.0018	± 0.0002	$^{+0.0003}_{-0.0002}$	0.88	0.86

Table C.9: Differential unpolarized inclusive-jet, dijet and three-jet cross-sections $d\sigma/dE_T^{\rm jet}$ and $d\sigma/d\overline{E_T}^{\rm jet}$ in e^+p collisions. Other details as in the caption to Table C.6.

Q^2 bin (GeV^2)	$d\sigma/dQ^2$ (pb/GeV^2)	$\delta_{\rm stat}$	$\delta_{\rm syst}$	$\delta_{\rm ES}$	$C_{\rm QED}$	$C_{\rm had}$
unpolarized - inclusive jets						
$200, 500$	0.01921	± 0.00087	± 0.00131	$^{+0.00190}_{-0.00180}$	0.98	0.97
$500, 1000$	0.01803	± 0.00056	± 0.00047	$^{+0.00049}_{-0.00048}$	0.99	1.00
$1000, 2000$	0.01268	± 0.00032	± 0.00017	± 0.00018	0.98	1.00
$2000, 4000$	0.00623	± 0.00016	± 0.00006	± 0.00003	0.97	1.00
$4000, 10000$	0.001963	± 0.000050	± 0.000097	± 0.000029	0.95	1.00
$10000, 20000$	0.000376	± 0.000016	± 0.000045	$^{+0.000015}_{-0.000016}$	0.94	1.00
$20000, 88000$	$1.121 \cdot 10^{-5}$	$\pm 0.091 \cdot 10^{-5}$	$\pm 0.706 \cdot 10^{-5}$	$^{+0.113}_{-0.114} \cdot 10^{-5}$	0.93	1.00
unpolarized - dijets						
$200, 500$	0.00409	± 0.00091	± 0.00112	$^{+0.00094}_{-0.00083}$	1.00	0.91
$500, 1000$	0.00323	± 0.00031	± 0.00037	$^{+0.00027}_{-0.00026}$	0.97	0.92
$1000, 2000$	0.00251	± 0.00016	± 0.00004	± 0.00009	0.97	0.91
$2000, 4000$	0.001170	± 0.000071	± 0.000112	$^{+0.000024}_{-0.000023}$	0.96	0.91
$4000, 10000$	0.000343	± 0.000021	± 0.000029	± 0.000011	0.95	0.89
$10000, 20000$	$69.8 \cdot 10^{-6}$	$\pm 6.9 \cdot 10^{-6}$	$\pm 23.9 \cdot 10^{-6}$	$\pm 4.1 \cdot 10^{-6}$	0.99	0.87
$20000, 88000$	$2.11 \cdot 10^{-6}$	$\pm 0.37 \cdot 10^{-6}$	$\pm 1.62 \cdot 10^{-6}$	$\pm 0.26 \cdot 10^{-5}$	0.96	0.86
unpolarized - three jets						
$500, 1000$	0.00034	± 0.00018	± 0.00015	$^{+0.00006}_{-0.00005}$	0.98	0.78
$1000, 2000$	0.000306	± 0.000073	± 0.000025	$^{+0.000027}_{-0.000026}$	0.96	0.78
$2000, 4000$	0.000193	± 0.000034	± 0.000024	$^{+0.000011}_{-0.000010}$	0.95	0.79
$4000, 10000$	$5.04 \cdot 10^{-5}$	$\pm 0.93 \cdot 10^{-5}$	$\pm 2.18 \cdot 10^{-5}$	$\pm 0.20 \cdot 10^{-5}$	0.95	0.79
$10000, 20000$	$1.04 \cdot 10^{-5}$	$\pm 0.25 \cdot 10^{-5}$	$\pm 0.70 \cdot 10^{-5}$	$^{+0.09}_{-0.08} \cdot 10^{-5}$	0.95	0.75
$20000, 88000$	$1.34 \cdot 10^{-7}$	$\pm 0.99 \cdot 10^{-7}$	$\pm 0.06 \cdot 10^{-7}$	$\pm 0.19 \cdot 10^{-7}$	0.92	0.77

Table C.10: Differential unpolarized inclusive-jet, dijet and three-jet cross-sections $d\sigma/dQ^2$ in $e^- p$ collisions. Other details as in the caption to Table C.6.

Q^2 bin (GeV^2)	$d\sigma/dQ^2$ (pb/GeV^2)	$\delta_{\rm stat}$	$\delta_{\rm syst}$	$\delta_{\rm ES}$	$C_{\rm QED}$	$C_{\rm had}$
unpolarized - inclusive jets						
$200, 500$	0.01525	± 0.00082	± 0.00074	$^{+0.00141}_{-0.00134}$	0.96	0.97
$500, 1000$	0.01241	± 0.00050	± 0.00018	± 0.00024	0.96	1.00
$1000, 2000$	0.00707	± 0.00026	± 0.00021	± 0.00003	0.95	1.00
$2000, 4000$	0.00273	± 0.00011	± 0.00010	± 0.00004	0.94	1.00
$4000, 10000$	0.000530	± 0.000027	± 0.000037	± 0.000021	0.91	1.00
$10000, 20000$	$4.35 \cdot 10^{-5}$	$\pm 0.53 \cdot 10^{-5}$	$\pm 0.71 \cdot 10^{-5}$	$\pm 0.40 \cdot 10^{-5}$	0.88	1.00
$20000, 88000$	$2.3 \cdot 10^{-7}$	$\pm 1.1 \cdot 10^{-7}$	$\pm 1.5 \cdot 10^{-7}$	$\pm 0.4 \cdot 10^{-7}$	0.81	1.00
unpolarized - dijets						
$200, 500$	0.00204	± 0.00072	± 0.00051	$^{+0.00042}_{-0.00037}$	0.98	0.92
$500, 1000$	0.00301	± 0.00033	± 0.00033	$^{+0.00025}_{-0.00024}$	0.96	0.93
$1000, 2000$	0.00152	± 0.00014	± 0.00003	$^{+0.00004}_{-0.00003}$	0.95	0.93
$2000, 4000$	0.000605	± 0.000058	± 0.000060	± 0.000016	0.94	0.92
$4000, 10000$	0.000106	± 0.000013	± 0.000011	± 0.000006	0.91	0.92
$10000, 20000$	$9.3 \cdot 10^{-6}$	$\pm 2.4 \cdot 10^{-6}$	$\pm 3.2 \cdot 10^{-5}$	$^{+1.1}_{-1.0} \cdot 10^{-6}$	0.92	0.92
$20000, 88000$	$7.4 \cdot 10^{-8}$	$\pm 7.4 \cdot 10^{-8}$	$\pm 5.8 \cdot 10^{-8}$	$\pm 1.1 \cdot 10^{-8}$	0.93	0.88
unpolarized - three jets						
$500, 1000$	0.00038	± 0.00020	± 0.00017	± 0.00006	0.97	0.78
$1000, 2000$	0.000156	± 0.000055	± 0.000013	$^{+0.000014}_{-0.000013}$	0.91	0.80
$2000, 4000$	0.000065	± 0.000021	± 0.000008	$^{+0.000003}_{-0.000002}$	0.91	0.80
$4000, 10000$	$9.2 \cdot 10^{-6}$	$\pm 4.4 \cdot 10^{-6}$	$\pm 4.1 \cdot 10^{-6}$	$\pm 0.7 \cdot 10^{-6}$	0.88	0.79
$10000, 20000$	$4.6 \cdot 10^{-7}$	$\pm 4.6 \cdot 10^{-7}$	$\pm 3.1 \cdot 10^{-7}$	$\pm 0.6 \cdot 10^{-7}$	1.00	0.82

Table C.11: Differential unpolarized inclusive-jet, dijet and three-jet cross-sections $d\sigma/dQ^2$ in e^+p collisions. Other details as in the caption to Table C.6.

x bin	$d\sigma/dx$ (pb)	$\delta_{\rm stat}$	$\delta_{\rm syst}$	$\delta_{\rm ES}$	$C_{\rm QED}$	$C_{\rm had}$
unpolarized - inclusive jets						
$0.006, 0.025$	13.12	± 0.50	± 0.74	$^{+0.86}_{-0.82}$	0.95	1.01
$0.025, 0.063$	35.82	± 0.85	± 1.13	$^{+0.70}_{-0.69}$	0.98	1.00
$0.063, 0.16$	49.26	± 0.98	± 0.09	± 0.14	0.97	0.99
$0.16, 0.40$	31.81	± 0.77	± 1.30	$^{+0.53}_{-0.54}$	0.97	0.99
$0.40, 1.0$	3.11	± 0.23	± 0.30	± 0.23	0.95	0.98

Table C.12: Differential unpolarized inclusive-jet cross-sections $d\sigma/dx$ in $e^- p$ collisions. Other details as in the caption to Table C.6.

x bin	$d\sigma/dx$ (pb)	$\delta_{\rm stat}$	$\delta_{\rm syst}$	$\delta_{\rm ES}$	$C_{\rm QED}$	$C_{\rm had}$
unpolarized - inclusive jets						
$0.006, 0.025$	9.49	± 0.47	± 0.41	$^{+0.54}_{-0.53}$	0.93	1.01
$0.025, 0.063$	21.40	± 0.71	± 0.76	± 0.24	0.96	1.00
$0.063, 0.16$	21.64	± 0.69	± 0.76	$^{+0.24}_{-0.23}$	0.95	0.99
$0.16, 0.40$	8.55	± 0.41	± 0.48	± 0.21	0.93	0.98
$0.40, 1.0$	0.439	± 0.090	± 0.084	± 0.032	0.91	0.98

Table C.13: Differential unpolarized inclusive-jet cross-sections $d\sigma/dx$ in $e^+ p$ collisions. Other details as in the caption to Table C.6.

lepton/ jet multiplicity	σ_{jets} (pb)	δ_{stat} (pb)	δ_{syst} (pb)	δ_{ES} (pb)	QCD predictions (pb)		
					ZEUS-S	CTEQ6	MRST
e^-/inclusive jet	56.18	0.68	0.53	$^{+0.34}_{-0.32}$	54.47 ± 0.75	54.05	54.56
e^+/inclusive jet	26.88	0.51	0.82	$^{+0.18}_{-0.17}$	26.77 ± 0.45	25.85	26.49
e^-/dijet	10.87	0.34	0.80	$^{+0.24}_{-0.23}$	9.14 ± 0.35	9.05	9.26
e^+/dijet	5.83	0.29	0.45	$^{+0.13}_{-0.12}$	4.57 ± 0.19	4.38	4.55
e^-/three jet	1.52	0.15	0.09	± 0.06	0.79 ± 0.22	0.79	0.82
e^+/three jet	0.563	0.110	0.037	$^{+0.025}_{-0.022}$	0.397 ± 0.118	0.386	0.409

Table C.14: Integrated unpolarized jet cross-sections σ_{jets} for jets of hadrons in the laboratory frame selected with the longitudinally invariant k_T cluster algorithm. The statistical, uncorrelated systematic and energy-scale (ES) uncertainties are shown separately. The predictions of QCD as given by the MEPJETcalculations using the ZEUS-S PDFs are shown at NLO for the inclusive-jet and dijet cross sections and at LO for the three-jet cross sections, together with the total theoretical uncertainty. Also shown are the total cross sections predicted by QCD using the CTEQ6 or MRST PDF sets.

m^{dijet} bin (GeV)	$d\sigma/dm^{\text{dijet}}$ (pb/GeV)	δ_{stat}	δ_{syst}	δ_{ES}	C_{QED}	C_{had}
unpolarized - dijets						
$10, 15$	0.090	± 0.011	± 0.010	± 0.001	1.02	0.87
$15, 20$	0.207	± 0.018	± 0.011	± 0.002	0.99	0.88
$20, 30$	0.284	± 0.016	± 0.032	$^{+0.005}_{-0.004}$	0.97	0.89
$30, 45$	0.250	± 0.014	± 0.028	$^{+0.006}_{-0.007}$	0.96	0.90
$45, 65$	0.0960	± 0.0083	± 0.0191	$^{+0.0051}_{-0.0038}$	0.95	0.94
$65, 90$	0.0385	± 0.0060	± 0.0058	$^{+0.0023}_{-0.0032}$	0.94	0.96
$90, 120$	0.0132	± 0.0046	± 0.0035	$^{+0.0023}_{-0.0016}$	0.97	0.96
m^{trijet} bin (GeV)	$d\sigma/dm^{\text{trijet}}$ (pb/GeV)	δ_{stat}	δ_{syst}	δ_{ES}	C_{QED}	C_{had}
unpolarized - three jets						
$20, 30$	0.0069	± 0.0024	± 0.0017	± 0.0001	0.99	0.83
$30, 45$	0.0253	± 0.0045	± 0.0009	$^{+0.0006}_{-0.0008}$	0.99	0.76
$45, 65$	0.0307	± 0.0049	± 0.0012	$^{+0.0012}_{-0.0011}$	0.97	0.77
$65, 90$	0.0150	± 0.0034	± 0.0054	$^{+0.0014}_{-0.0012}$	0.94	0.79
$90, 120$	0.0036	± 0.0022	± 0.0001	$^{+0.0004}_{-0.0003}$	0.94	0.85

Table C.15: Differential unpolarized dijet and three-jet cross-sections $d\sigma/dm^{\text{dijet}}$ and $d\sigma/dm^{\text{dijet}}$ in $e^- p$ collisions. Other details as in the caption to Table C.6.

m^{dijet} bin (GeV)	$d\sigma/dm^{\text{dijet}}$ (pb/GeV)	δ_{stat}	δ_{syst}	δ_{ES}	C_{QED}	C_{had}
unpolarized - dijets						
$10, 15$	0.069	± 0.011	± 0.007	± 0.001	0.96	0.90
$15, 20$	0.146	± 0.017	± 0.010	$^{+0.001}_{-0.002}$	0.96	0.90
$20, 30$	0.171	± 0.015	± 0.022	± 0.003	0.95	0.91
$30, 45$	0.108	± 0.010	± 0.013	± 0.003	0.95	0.93
$45, 65$	0.0522	± 0.0077	± 0.0103	$^{+0.0023}_{-0.0025}$	0.94	0.95
$65, 90$	0.0169	± 0.0052	± 0.0026	$^{+0.0015}_{-0.0011}$	0.94	0.97
$90, 120$	0.0020	± 0.0020	± 0.0002	$^{+0.0003}_{-0.0002}$	0.92	0.99
m^{trijet} bin (GeV)	$d\sigma/dm^{\text{trijet}}$ (pb/GeV)	δ_{stat}	δ_{syst}	δ_{ES}	C_{QED}	C_{had}
unpolarized - three jets						
$20, 30$	0.0051	± 0.0024	± 0.0013	± 0.0001	0.91	0.84
$30, 45$	0.0124	± 0.0037	± 0.0006	$^{+0.0005}_{-0.0003}$	0.95	0.75
$45, 65$	0.0076	± 0.0029	± 0.0007	± 0.0004	0.94	0.78
$65, 90$	0.0049	± 0.0024	± 0.0018	$^{+0.0005}_{-0.0004}$	0.90	0.81

Table C.16: Differential unpolarized dijet and three-jet cross-sections $d\sigma/dm^{\text{dijet}}$ and $d\sigma/dm^{\text{trijet}}$ in e^+p collisions. Other details as in the caption to Table C.6.

Appendix D

Purities, Efficiencies, Acceptances

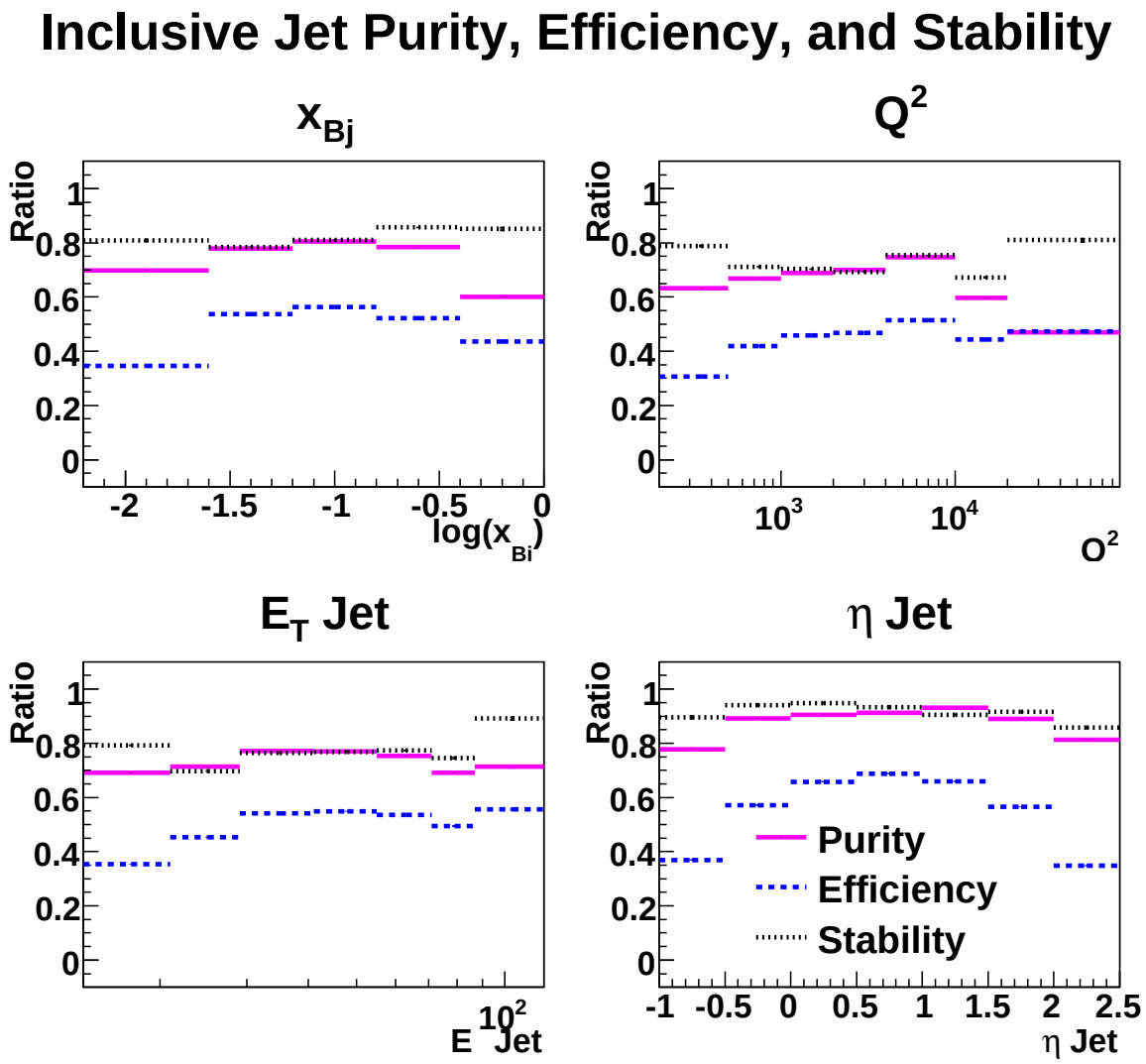

Figure D.1: Purity, Efficency and Correction Factors for Inclusive Jet Cross Sections

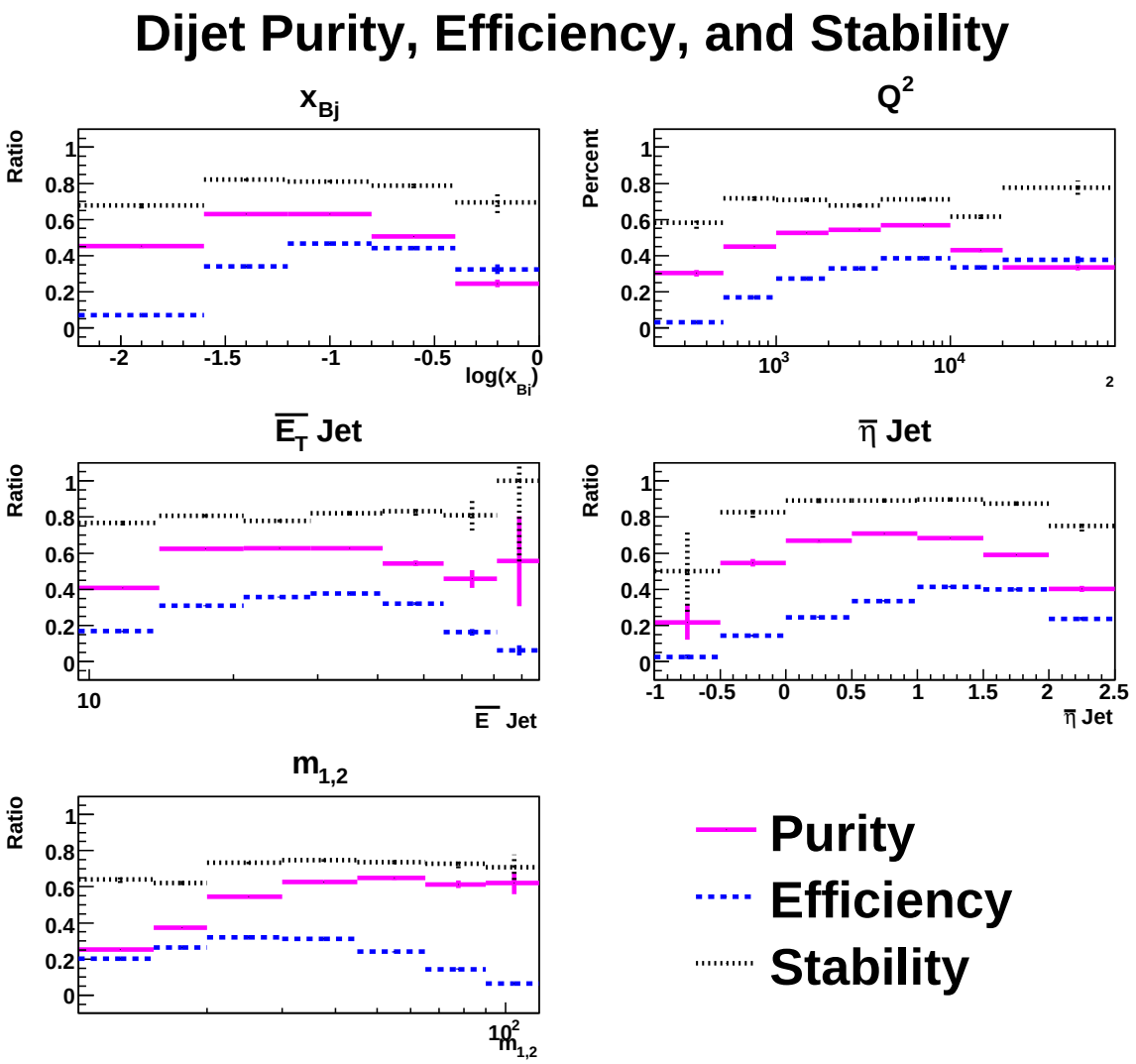

Figure D.2: Purity, Efficency and Correction Factors for Dijet Cross Sections

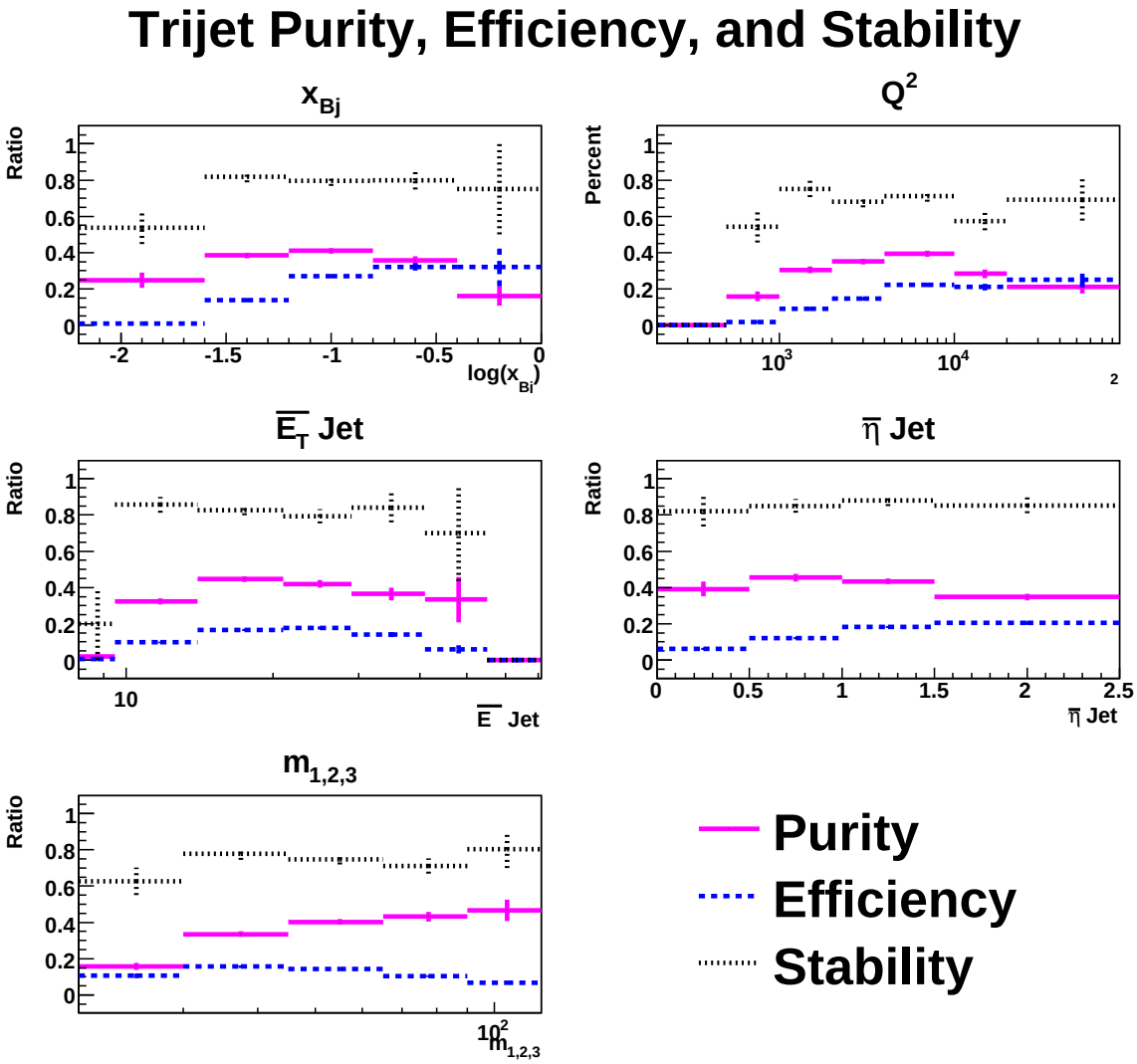

Figure D.3: Purity, Efficency and Correction Factors for Trijet Cross Sections

Appendix E

Systematic Uncertainties

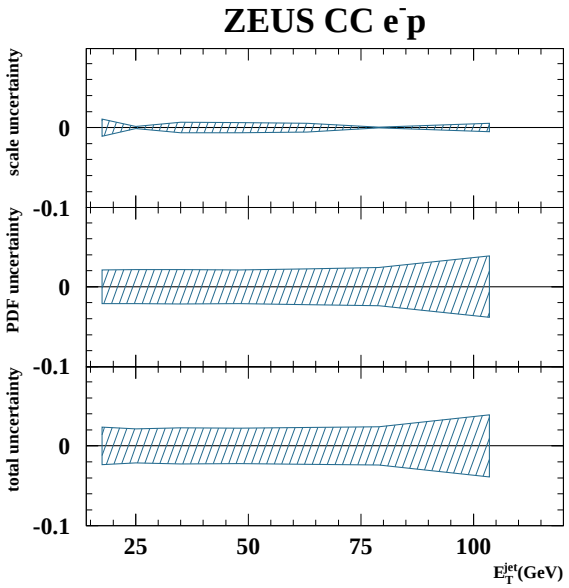

Figure E.1: Theoretical Uncertainty $E_T^{\rm jet}$ $e^- p$ 1Jet

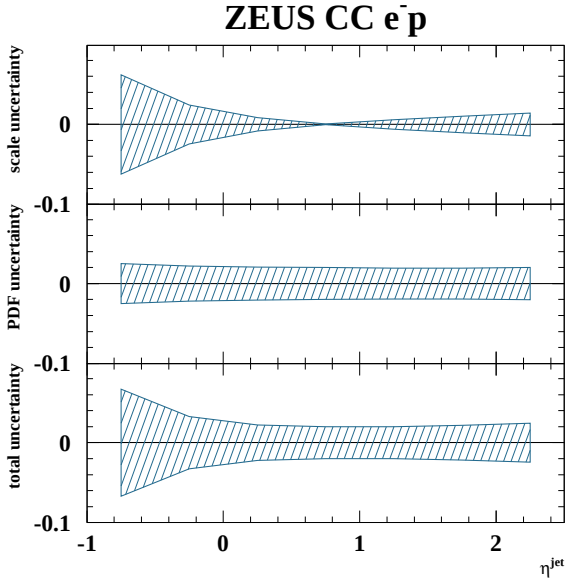

Figure E.2: Theoretical Uncertainty η^{jet} $e^{-}p$ 1Jet

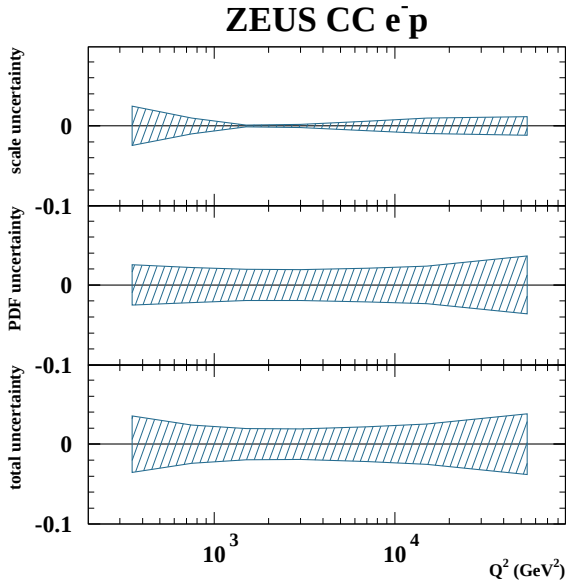

Figure E.3: Theoretical Uncertainty Q^2 $e^- p$ 1Jet

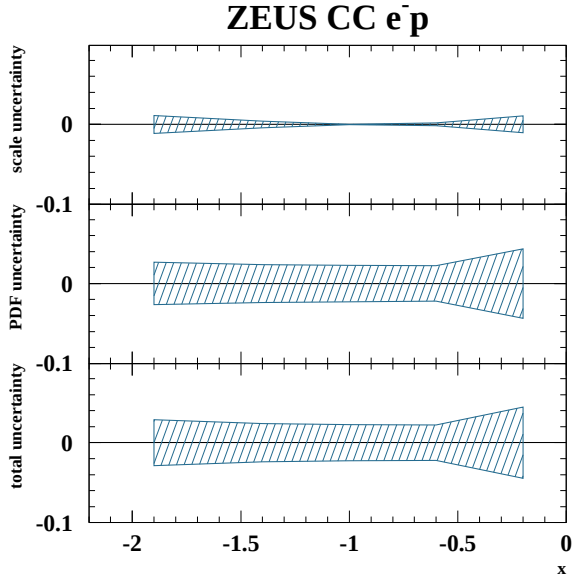

Figure E.4: Theoretical Uncertainty $e^{-}p$ x 1Jet

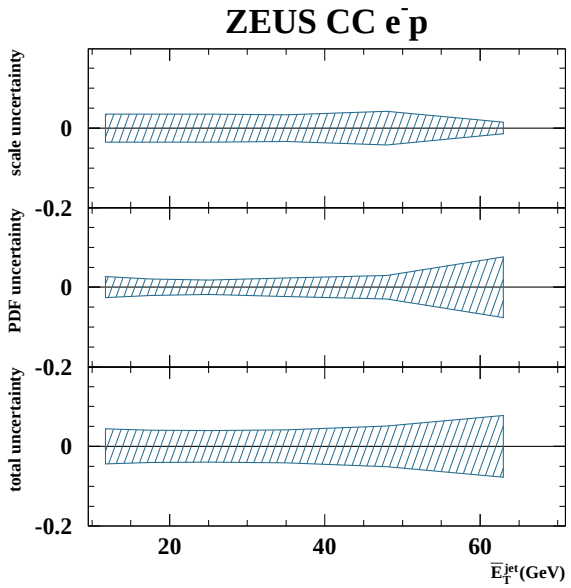

Figure E.5: Theoretical Uncertainty $e^{-}p$ $E_T^{\rm jet}$ Dijet

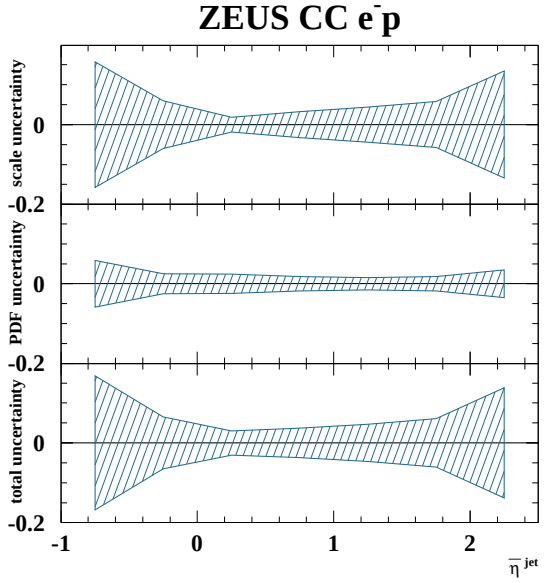

Figure E.6: Theoretical Uncertainty $e^{-}p$ η^{jet} Dijet

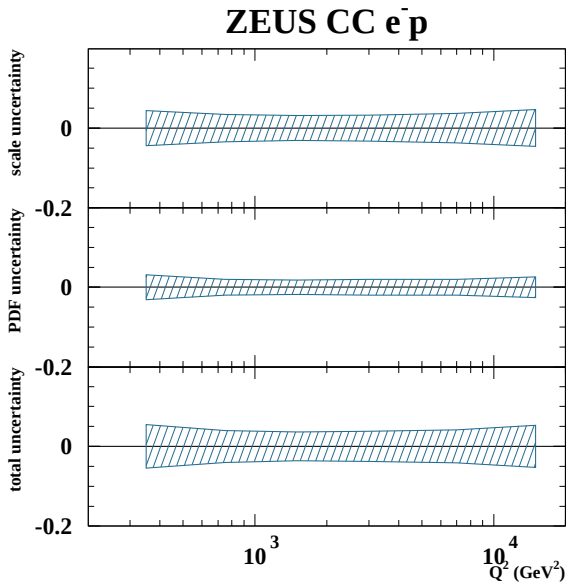

Figure E.7: Theoretical Uncertainty $e^{-}p$ Q^2 Dijet

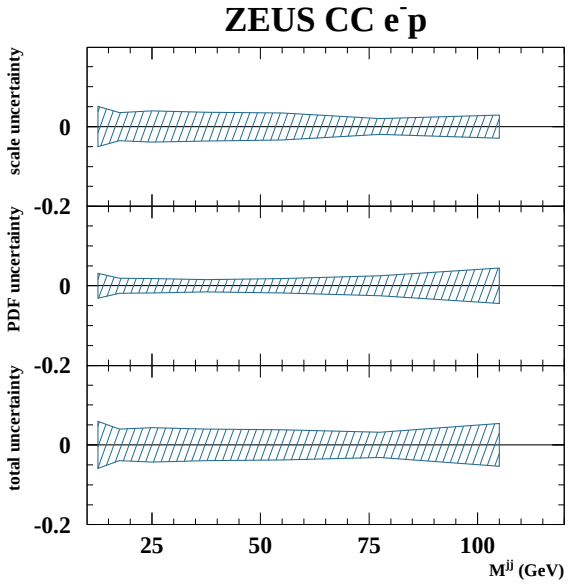

Figure E.8: Theoretical Uncertainty $e^{-}p$ m Dijet

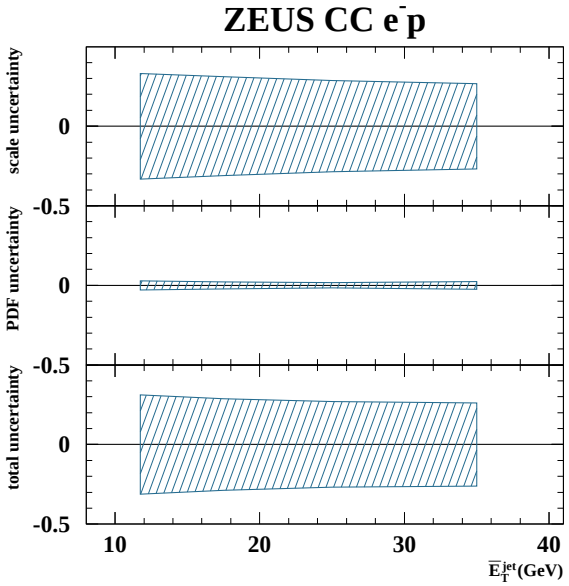

Figure E.9: Theoretical Uncertainty $e^- p$ E_T^{jet} Trijet

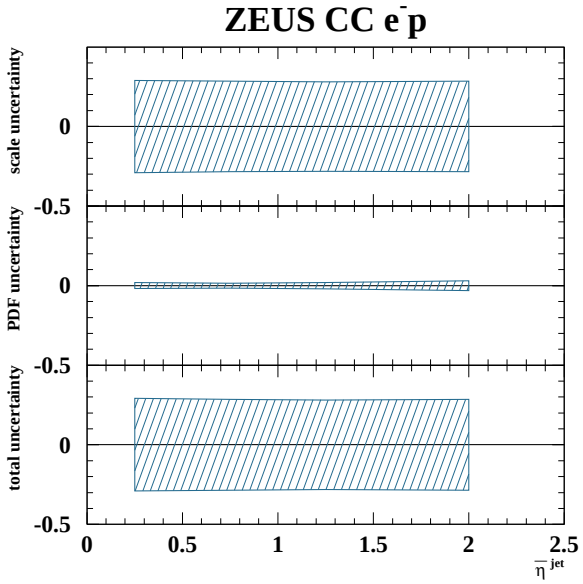

Figure E.10: Theoretical Uncertainty $e^- p$ η^{jet} Trijet

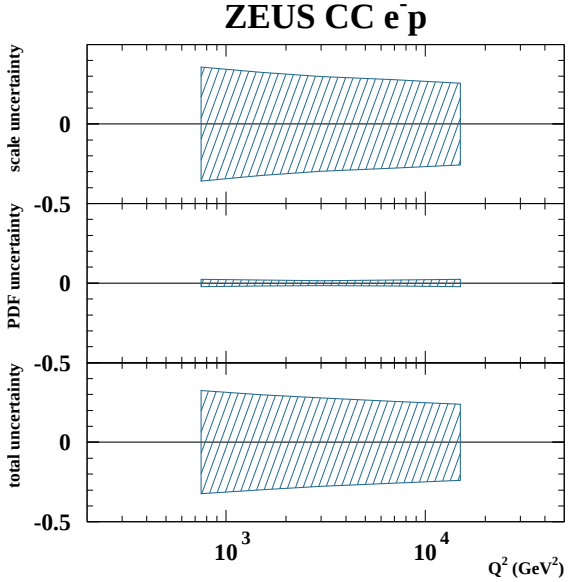

Figure E.11: Theoretical Uncertainty $e^- p$ Q^2 Trijet

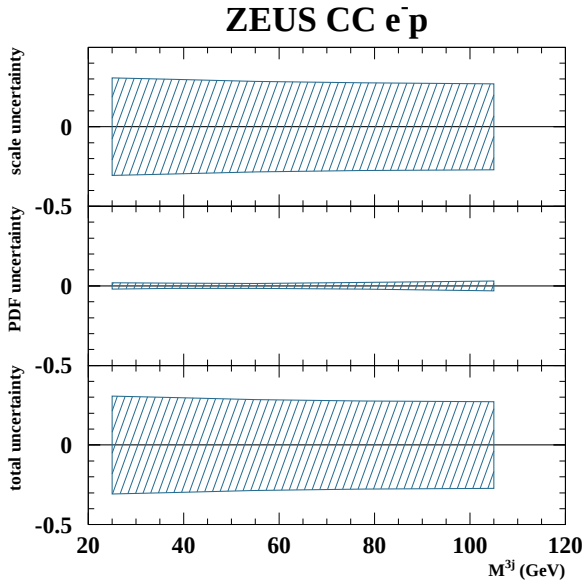

Figure E.12: Theoretical Uncertainty m Trijet

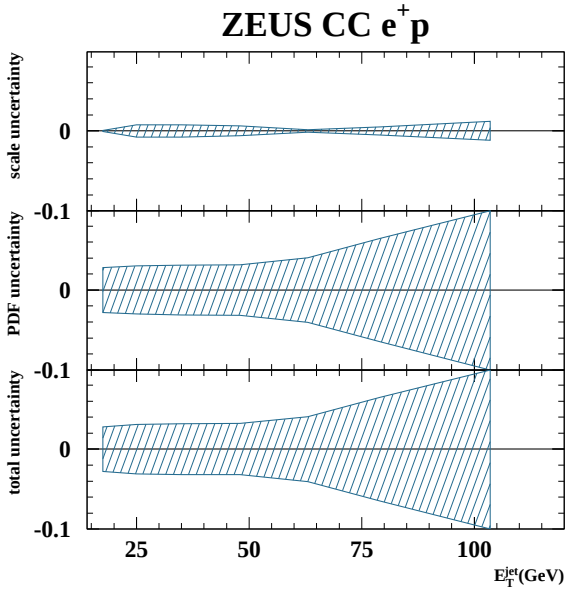

Figure E.13: Theoretical Uncertainty E_T^{jet} e^+p 1Jet

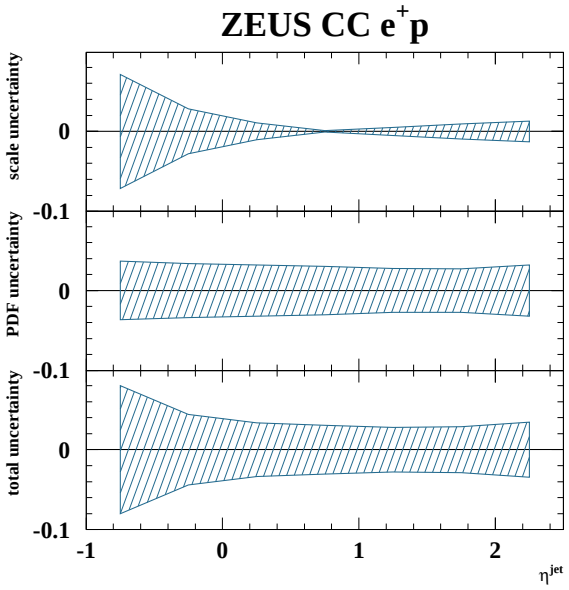

Figure E.14: Theoretical Uncertainty η^{jet} $e^{+}p$ 1Jet

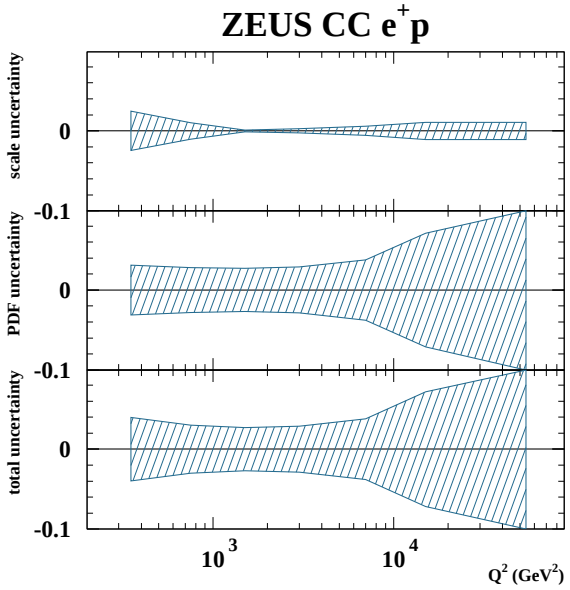

Figure E.15: Theoretical Uncertainty Q^2 e^+p 1Jet

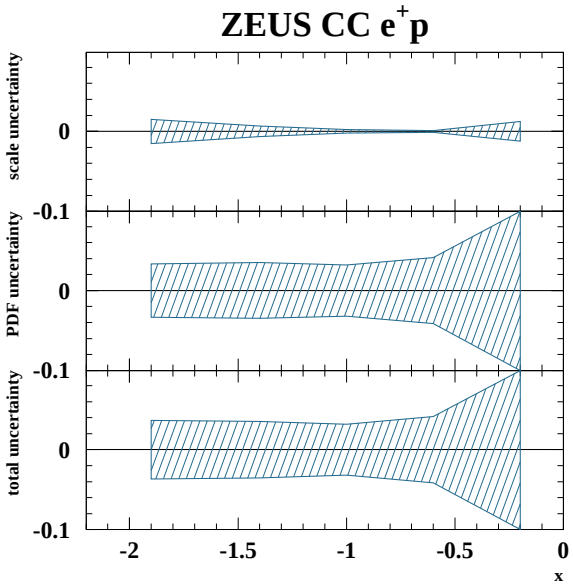

Figure E.16: Theoretical Uncertainty e^+p x 1Jet

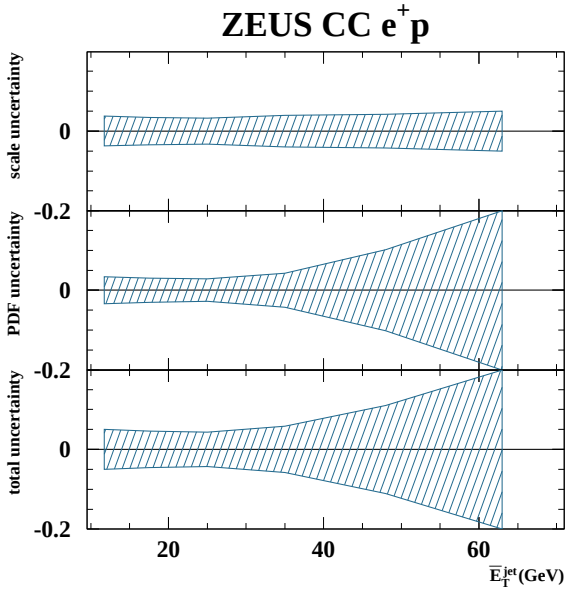

Figure E.17: Theoretical Uncertainty e^+p $E_T^{\rm jet}$ Dijet

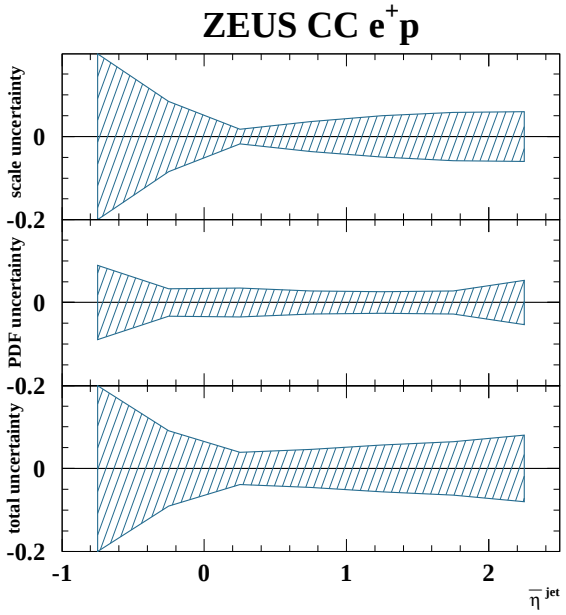

Figure E.18: Theoretical Uncertainty e^+p η^{jet} Dijet

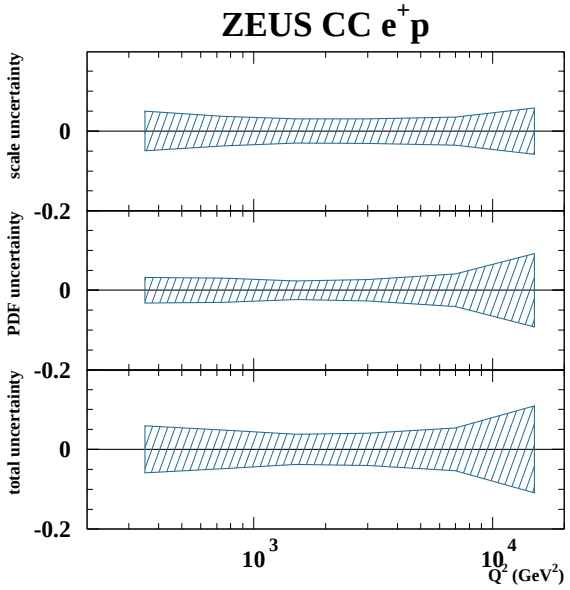

Figure E.19: Theoretical Uncertainty e^+p Q^2 Dijet

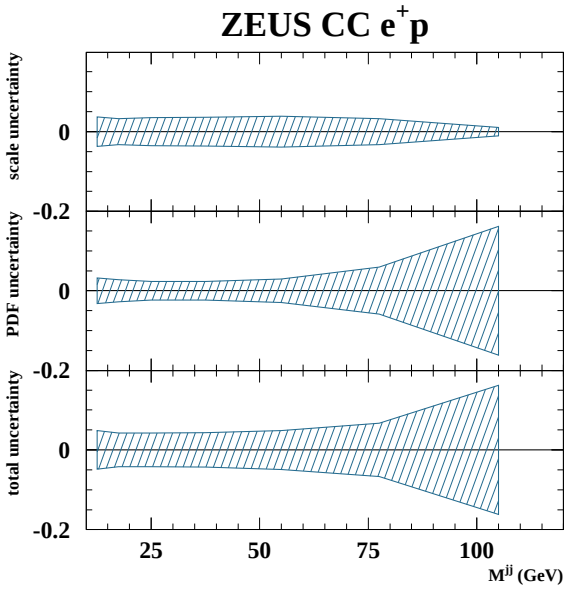

Figure E.20: Theoretical Uncertainty e^+p m Dijet

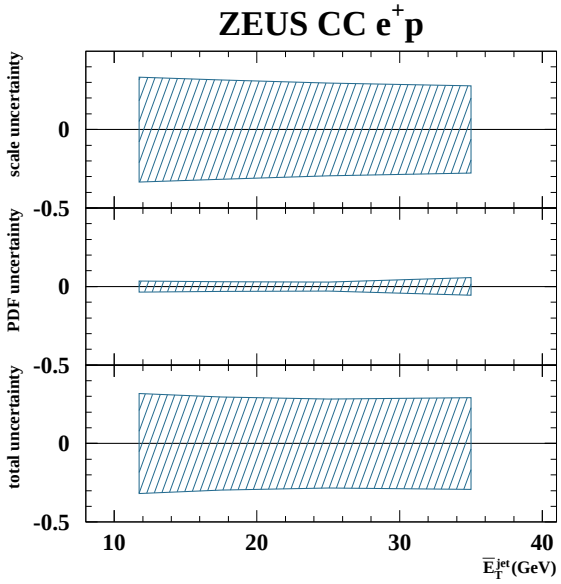

Figure E.21: Theoretical Uncertainty $e^{+}p$ E_T^{jet} Trijet

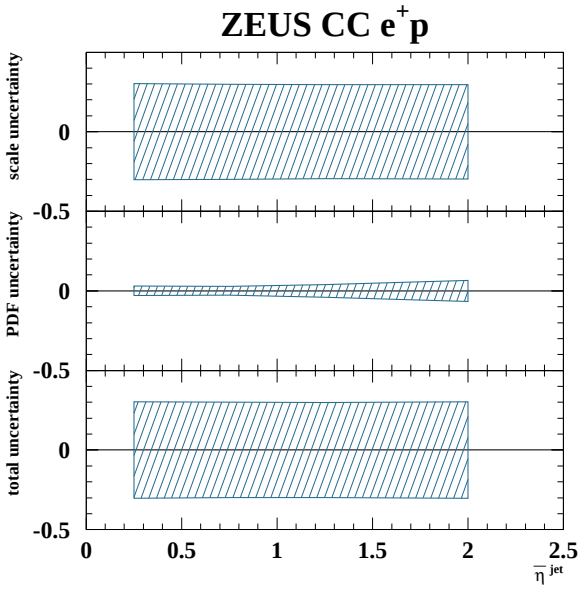

Figure E.22: Theoretical Uncertainty e^+p $\eta^{\rm jet}$ Trijet

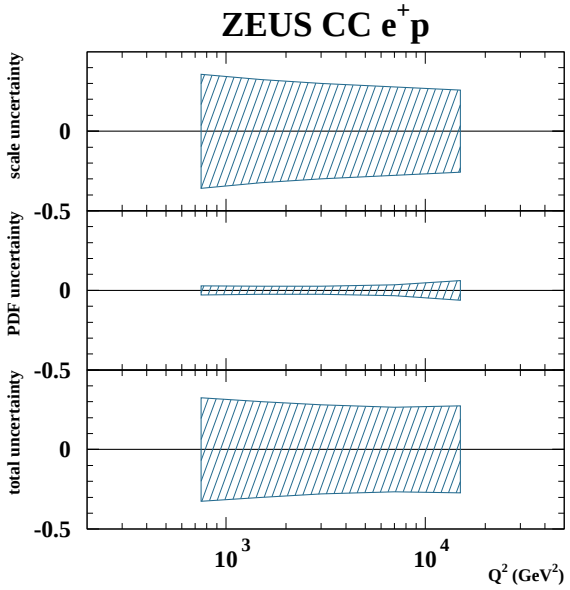

Figure E.23: Theoretical Uncertainty $e^{+}p$ Q^2 Trijet

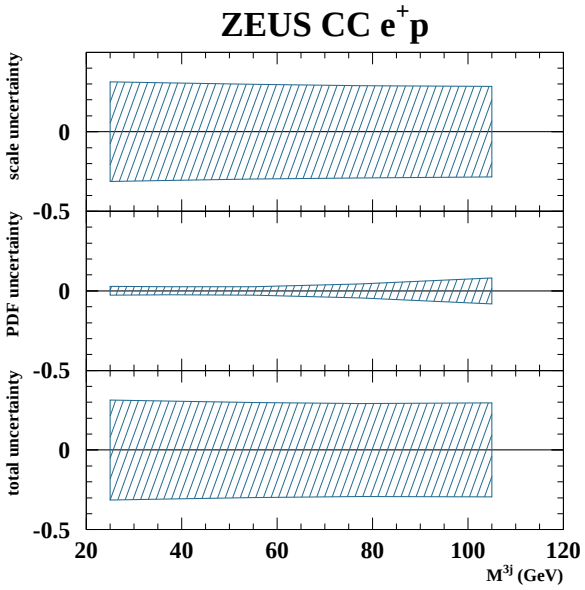

Figure E.24: Theoretical Uncertainty m Trijet

Appendix F

Technical Trigger Specifications

All trigger bits at each level described below additionally have overriding vetoes from timing information provided by the calorimeter, C5, SRTD, or Global Calormeter. This timing information is used to reject background events including beamgas, halo muon, cosmic muons.

F.1 First Level Trigger Selection

The FLT was divided into 64 independent bits, each of which recorded a true or false state for each event depending on specific physical conditions. The FLT bits used in the principle and secondary selections are listed in table F.1. For each trigger analysis, at least one bit in the FLT selection was required to be set to true. The bits definition depended on the run number, specifically in the case of bits 60 and 63, which changed on run 54115.

In table F.1, tight track veto refers to selection vetoes where events were rejected due to a large number of non-vertex tracks. B_{isoe} is true if an isolated calorimeter deposit in the BCAL was located which is consistent with an isolated electron. $N_{\rm gt}$ is the number of tracks found with strict quality standards. E_{EMC} and E_{BEMC} are the

FLT bit number	Principle	Alternative	Description
31		✓	$E_{T,Fbp} + E_T \geq 45$ GeV
39	✓	✓	$E_{BEMC} \geq 3$ GeV and B_{isoe} and $N_{\rm gt} \geq 1$ and Loose Track Veto
40	✓	✓	$E_{EMC} \geq 25$ GeV and Tight Track Veto
41	✓	✓	$E_T \geq 30$ GeV and Tight Track Veto
43	✓	✓	$E_T \geq 12$ GeV and $N_{\rm gt} \geq 1$ and Tight Track Veto
44	✓	✓	($E_{BEMC} \geq 10$ GeV or $E_{REMC} \geq 3$ GeV), B_{isoe}, $N_{\rm gt} \geq 1$, and Tight Track Veto
50		✓	$(E_{CAL} \geq 15$ GeV$\|\|E_{EMC} \geq 10$ GeV$\|\|E_{BEMC} \geq 3$ GeV$\|\|E)_{REMC} >= 2$ GeV)&&TRK_q95b&&$(Et_HFL >= 892)$
60 (Run $\leq$ 54115)	✓	✓	($P_{T,\rm miss} > 5$ GeV and $E_{T,-2IR} > 5$ GeV and $N_{vtxtrk} \geq 1$) or ($P_{T,\rm miss} > 8$ GeV and $N_{trks} \geq 1$) or ($P_{T,\rm miss} > 8$ GeV and $E_{FCAL} \geq 10$ GeV) and not FCLR beam gas
60 (Run $>$ 54115)	✓	✓	($P_{T,\rm miss} > 5$ GeV and $E_{T,-2IR} > 5$ GeV and $N_{vtxtrk} \geq 1$) or ($P_{T,\rm miss} > 11.5$ GeV and $N_{trks} \geq 1$) or ($P_{T,\rm miss} > 11.5$ GeV and $E_{FCAL} \geq 10$ GeV) and not FCLR beam gas
63 (Run $>$ 54115)	✓	✓	($P_{T,\rm miss} > 5$ GeV and $E_{T,-2IR} > 5$ GeV and $N_{vtxtrk} \geq 1$) or ($P_{T,\rm miss} > 8$ GeV and $N_{trks} \geq 1$) or ($P_{T,\rm miss} > 11.5$ GeV and $E_{FCAL} \geq 10$ GeV) and not FCLR beam gas

Table F.1: First Level Trigger bits used in this analysis.

energies located in the entire EMC and Barrel EMC, respectively. Additional vetoes from the C5 counter and Veto Wall apply to all bits.

In FLT60 before run 54115, an event was vetoed by the FCLR if the highest energy RCAL cluster had an energy greater than 50 GeV, and the highest energy tower in the highest energy RCAL cluster was located in the inner ring of the RCAL. Due to increased dead time during 2005 data taking, the requirements of FLT60 was divided up into two bits: FLT60 and FLT63. FLT60 and FLT63 after run 54115 had the same veto conditions as FLT60 before run 54115, but afterwards FLT63 additionally was FCLR vetoed if $E - p_z < 3$ GeV

F.2 Second Level Trigger Selection

In the principle selection, events were required to have SLT bit EXO04 set to true. Elements of SLT EXO04 are defined in table F.2. SLT EXO04 was true if all of the following conditions were satisfied:

- (CCtimeOK||CCCTDOK)
- NoOffBeamProton
- (CC1||CC2 ||CC3||CC4)

The alternate selection required that the SLT bit HPP05 was set to true, which was satisfied if all the following conditions were met:

- FLT: 28,30,31,39,40,41,42,43,44,50, or 60
- $N_{\mathrm{gt}} \geq 1$
- $P_{T,\mathrm{miss}} > 8$ GeV

$N^{\mathrm{G}}{}_{\mathrm{PMT}}$	The number of PMTs in the global calorimeter
CCtimeOK	$\lvert T_{\mathrm{G}}\rvert < 7\,\mathrm{ns}$ and $N^{\mathrm{G}}{}_{\mathrm{PMT}} > 1$
CCCTDOK	$N_{\mathrm{trk}} \geq 1$ and $Z_{\mathrm{vtx}} < 100\,\mathrm{cm}$
NoOffBeamProton	$\lvert p_y\rvert > 3$ GeV or $P_{T,\mathrm{miss}} > 15$ GeV or $P_{T,\mathrm{miss}}(-1IR) > 6$ GeV or $P_{T,\mathrm{miss}} > 0.06 p_z$
CC1	$P_{T,\mathrm{miss}} > 6$ GeV and $E_T(-2IR) > 6$ GeV and $N_{\mathrm{gt}} > 1$
CC2	$P_{T,\mathrm{miss}} > 9$ GeV and $P_{T,\mathrm{miss}}(-1IR) > 8$ GeV and $E_{FCAL} > 20$ GeV
CC3	$P_{T,\mathrm{miss}} > 9$ GeV and $(P_{T,\mathrm{miss}})^2 > 2.31 \times E_T$ and $E_{FCAL} > 80$ GeV
CC4	$E - p_z > 6$ GeV and $(P_{T,\mathrm{miss}})^2 > 2.25 \times E_T$ and $N_{\mathrm{gt}} > 1$

Table F.2: EXO4 Second Level Trigger Definitions

- $E_T^{cone} > 8$ GeV
- $P_{T,\mathrm{miss}}/E_T > 0.3$

F.3 Third Level Trigger Selection

The principle selection required that either the TLT bit EXO02 or EXO06 was set to true. TLT EXO02 was true if all of the following conditions were satisfied:

- $P_{T,\mathrm{miss}} > 6$ GeV
- $|z_{vtx}| < 60$ cm
- UDTimeOK

where UDTimeOK compares the timing information from the upper and lower half of the calorimeter. This condition rejected cosmic rays, which often come from above the ZEUS detector. EXO06 was set to true if all of the following conditions were met:

- $P_{T,\mathrm{miss}} > 6$ GeV
- $\big(E_{FCAL} > 10$ GeV $\parallel N_{\mathrm{gt}} > 0\big)$
- OffBeamProton
- BeamGasVertex
- (TooManyBeamGasTracks —— (Good Vertex && $N_{vtxtracks} \geq 2$))
- $(N_{CTDhits} < 2500 \| P_{T,\mathrm{miss}} > 10$ GeV)
- UDTimeOK

The alternative trigger required one of TLT bits HPP05, HPP06, HPP10 to be set to true. HPP TLT 05 true was equivalent to all of the following being true:

- HPP SLT 5 == true
- $P_{T,\mathrm{miss}} > 8$ GeV
- $E_T^{cone} > 8$ GeV

HPP TLT 06 true was equivalent to all of the following being true:

- HPP SLT 5 == true
- $P_{T,\mathrm{miss}} > 8$ GeV
- at least 1 cone jet with $E_T^{\mathrm{jet}} > 8$ GeV, $\eta^{\mathrm{jet}} < 2.5$

Note that this is the only condition in this thesis where cone jets were considered. In all other points, a jet will refer explicitly to jets found using the k_T cluster algorithm. HPP TLT 10 true was equivalent to all of the following being true:

- HPP SLT 5 == true
- $P_{T,\mathrm{miss}} > 8$ GeV
- at least 1 k_T jet with $E_T^{\mathrm{jet}} > 8$ GeV, $\eta^{\mathrm{jet}} < 2.5$

F.4 DST Bits

In the principle trigger selection, data events were required to have DST bit 34 set to true. This bit was equivalent to the principle trigger selection described in the

following sections. In the secondary selection, at least one of DST bits 34, 68, 69 and 73 was required to be set to true. These bits form a superset of the alternative trigger selection.

F.5 Selection Flags

The ZEUS reconstruction library contains a flag EVTAKE for each event, which is set to true if the event was taken during reliable conditions. Data events were only selected if the EVTAKE flag was set to true. MC events were not subject to this selection.

The two methods of polarization measurement, LPOL and TPOL, produced comparable but different measurements of the average polarization during each data taking run. The ZEUS reconstruction library contains two boolean flags, LPOLTAKE and TPOLTAKE, which indicate if the event was taken when the LPOL and TPOL were functioning properly. If the integrated luminosity for a given run measured by the LPOL L_{LPOL} was greater than or equal to that that of the TPOL, L_{TPOL}, then data events were only selected if LPOLTAKE was true. If $L_{\mathrm{TPOL}} > L_{\mathrm{LPOL}}$ during the run, then events were only taken if TPOLTAKE was true. MC events were not subject to this selection. The average polarization value and integrated luminosity for each data run was exclusively taken from the LPOL if $L_{\mathrm{LPOL}} < L_{\mathrm{TPOL}}$, otherwise values from the TPOL were used. All MC presented here have zero average polarization.

Events were required to have $P_{T,\mathrm{miss}} > 9$ GeV, $P_{T,\mathrm{miss}}/E_T > 0.3$, and at least one calorimeter jet within $-1 < \eta^{\mathrm{jet}} < 2.5$ and $E_T^{\mathrm{jet}} > 3$ GeV, where E_T^{jet} was computed purely from cell energies. These cuts are less restrictive forms of applied cuts and will be described later in this chapter in detail. Events meeting all these criteria were

then retrieved from the ZARAH computing farm and stored on a local workstation for analysis.

Appendix G

Correction Functions

Bibliography

[1] Theodore Arabatzis, *Representing Electrons: A Biographical Approach to Theoretical Entities*. University of Chicago, Chicago, 2006.

[2] Milorad Mladjenovic, *The History of Early Nuclear Physics (1896-1931)*. World Scientific, Singapore, 1992.

[3] Herman Cember, *Introduction to Health Physics*. McGraw-Hill Professional, New York, 1996.

[4] N. Bohr, Phil. Mag. **6**, 1 (1913).

[5] E. Rutherford, Phil. Mag. 6 **37**, 537 (1919).

[6] J. Chadwick, Nature **136**, 692 (1932).

[7] E. Schrödinger, Phys. Rev. 28 **6**, 1049 (1926).

[8] G. Gamow, Z. Phys. **51**, 204 (1928).

[9] Albert Einstein, Hermann Minkowski, , Meghnad Saha, Satyendra Bose, *The principle of relativity; original papers*. University of Calcutta, Calcutta, 1920.

[10] Jong-Ping Hsu and Dana Fine, *100 Years of Gravity And Accelerated Frames*. World Scientific, Singapore, 2005.

[11] W. Heisenberg, Zeits. f. Phys. **77**, 1 (1932).

[12] C.N.Yang and R.F. Mills, Phys. Rev. **1**, 191 (1954).

[13] E. Wigner, Phys. Rev. **51**, 106 (1937).

[14] T. D. Lee and C. N. Yang, Phys. Rev. **104**, 254 (1956).

[15] C.S. Wu, Phys. Rev. **105**, 1413 (1957).

[16] P. Watkins, *Story of the W & Z*. Cambridge University Press, Cambridge, 1986.

[17] M. Gell-Mann, *The Eightfold Way: A Theory of Strong Interaction Symmetry*, Technical Report TID-12608, California Inst. of Tech., Pasadena. Synchrotron Lab., Pasadena, California, March 1961.

[18] G. Zweig, *An SU*(3) *Model of Strong Interaction Symmetry and Its Breaking*, Technical Report 8419/TH-412, CERN, Geneva, Switzerland, 1964.

[19] D. Gross, Nucl. Phys. Proc. Suppl. **74**, 426 (1999).

[20] BNL Bubble-Chamber Group, *High Energy Physics with the 80"Bubble Chamber*, Technical Report BNL-9065, Brookhaven National Laboratory, Upton, New York, 1966.

[21] M. Gell-Mann, Phys.Lett. **8**, 214 (1964).

[22] A. Pickering, *Constructing Quarks: A Sociological History of Particle Physics*, First edition$^{\text{th}}$ edn. Edinburgh University Press, Edinburgh, 1984.

[23] E.D. Bloom *et al*, Phys. Rev. Lett. **23**, 935 (1969).

[24] F. Halzen and A.D. Martin, *Quarks and Leptons*, 2nd edition$^{\text{th}}$ edn. John Wiley and Sons, New York, 1984.

[25] E. Mirkes and D. Zeppenfeld, Phys. Lett. **B**, 205 (1996).

[26] E. Mirkes, *Theory of Jets in Deep Inelastic Scattering* (unpublished), 1997, available on `http://hep-ph/9711224v1`. U. Karlseruhe TTP97-39.

[27] W. T. Giele, E. W. N. Glover and D. A. Kosower, Nuclear Phys. **B403**, 633 (1993).

[28] G. 't Hooft, Nucl. Phys. B **61**, 455 (1973).

[29] W. A. Bardeen, Phys. Rev. D **18**, 3998 (1978).

[30] ZEUS Coll., S. Chekanov et al., Phys. Rev. **D 67**, 012007 (2003).

[31] J. Pumplin et al., JHEP **07**, 012 (2002).

[32] D. Stump, et al., JHEP **10**, 046 (2003).

[33] A.D. Martin et al., Eur.Phys.J. C **35**, 325 (2004).

[34] C. Duprel et al., *Proceedings of the Workshop on Monte Carlo Generators for HERA Physics*, A.T. Doyle, G. Grindhammer, G. Ingelman, H. Jung (ed.), pp. 142 – 150. Hamburg, Germany (1979). Also in preprint arXiv:hep-ph/9910448v1. MADPH-99-1129, PITHA 99/30.

[35] S. Catani and M. H. Seymour, Nucl. Phys. **B 485**, 291 (1997).

[36] A.A. Sokolov and I.M.Ternov, Sov. Phys. Dokl. **8**, 1203 (1964).

[37] ZEUS Coll., *A microvertex Detector for ZEUS* (unpublished), 1997, available on `http://www-zeus.desy.de/ZEUS_ONLY/zeus_notes/ZEUS_NOTES/ZEUS-97-006.ps`. ZEUS-97-006, DESY-PRC 97/01.

[38] J. Krüger, *The Uranium Scintillator Calorimeter for the ZEUS Detector at the Electron-Proton Collider HERA* (unpublished). DESY F35-92-02, 1992.

[39] H1 Coll., I. Abt et al., Nucl. Inst. Meth. **A 386**, 310 (1997).

[40] H1 Coll., SPACAL group, R.-D. Appuhn et al., Nucl. Inst. Meth. **A 386**, 397 (1997).

[41] Helbich M. ; Ning Y. ; Paganis S. ; Ren Z. ; Schmidke W. B. ; Sciulli F. ; Schneekloth U. ; Bttner C. ; Caldwell A. ; Sutiak J., Nuc. Instrum. Meth. A **565**, 572 (2006).

[42] G. F. Hartner, *VCTRAK Briefing: Program and Math* (unpublished). Zeus-98-058, internal ZEUS-note, 1998.

[43] J. Repond, *Jet Energy Corrections* (unpublished). ZEUS Note96-104.

[44] Abramowicz, Halina and Caldwell, Allen and Sinkus, Ralph, Nucl. Instrum. Meth. **A365**, 508 (1995).

[45] M. Wodarczyk, *Measurement of the F_2 Structure Function of the Proton at HERA from 1996 and 1997 ZEUS Data*. Ph.D. Thesis, University of Wisconsin, 1999.

[46] F. Jaquet and A. Blondel, *Proc. of the European Committee for Future Accelerators*, U. Amaldi (ed.), p. 391. Hamburg, Germany (1979). DESY-79-48.

[47] S.Catani et al., Nucl. Phys. **B406**, 187 (1993).

[48] CTEQ Coll., H.L. Lai et al., Eur. Phys. J. **C 12**, 375 (2000).

[49] A.D. Martin, R.G. Roberts and W.J. Stirling, Phys. Rev. **D 50**, 6734 (1994).

[50] ZEUS Coll., S. Chekanov et al., Eur. Phys. J. **C 42**, 1 (2005).

[51] M. Bengtsson, G. Ingelman and T. Sjöstrand, *Proc. HERA Workshop*, R.D. Peccei (ed.), Vol. 1, pp. 149–165. DESY, Hamburg, Germany (1987).

[52] G. Gustafson and U. Pettersson, Nucl. Phys. **B 306**, 746 (1988).

[53] T. Sjöstrand, PYTHIA 5.7 AND JETSET 7.4 PHYSICS AND MANUAL, 1993. Preprint CERN-TH 7112/93.

[54] L. Lönnblad, Comp. Phys. Comm. **71**, 15 (1992).

[55] B. Andersson et al., Phys. Rep. **97**, 31 (1983).

[56] A. Kwiatkowski, H. Spiesberger and H.-J. Möhring, Comp. Phys. Comm. **69**, 155 (1992). Also in *Proc. Workshop Physics at HERA*, 1991, DESY, Hamburg.

[57] K. Charchula, G.A. Schuler and H. Spiesberger, Comp. Phys. Comm. **81**, 381 (1994).

[58] R. Brun et al., GEANT3, Technical Report CERN-DD/EE/84-1, CERN, 1987.

[59] ZEUS Collaboration; S. Chekanov et al., Phys. Lett. **B 637**, 210 (2006).

[60] ZEUS Coll., S. Chekanov et al., Eur. Phys. J. **C 31**, 149 (2003).

[61] P.J. Bussey, *EUCELL*. ZEUS Phantom Library.

[62] Wing, M. (on behalf of the ZEUS Coll.), *Proc. of the 10th International Conference on Calorimetry in High Energy Physics hep-ex/0206036.*, R. Zhu (ed.), p. 767. Pasadena, USA (2002). Also in preprint hep-ex/0206036.

[63] S. Bethke, Prog. Part. Nucl. Phys. **58**, 351 (2007).